-reactor measurements of catalytic activity of mass selected nano-particles

Riedel, Jakob Nordheim

Publication date:
2016

Document Version
Publisher's PDF, also known as Version of record

Center for Individual Nanoparticle Functionality

Technical University of Denmark

PhD Thesis

μ-reactor measurements of catalytic activity of mass selected nano-particles

Author:

Jakob Nordheim Riedel

Supervisor:

Prof. Ib Chorkendorff

May 31st, 2016

DTU Physics

Department of Physics

Jakob Nordheim Riedel
μ-reactor measurements of catalytic activity of mass selected nanoparticles
Technical University of Denmark
PhD Thesis
Author's e-mail:
jakob.riedel@gmail.com

Jakob Nordheim Riedel, May 31st, 2016

"I want to understand everything," said Miro. "I want to know everything and put it all together to see what it means."
"Excellent project," she said. "It will look very good on your resume."
-conversation between Miro and Jane, Speaker for the Dead

Cover illustration:
Hydrogen and deuterium being dissociated on oxidized clusters in the μ-reactor.

Preface

The work presented in the thesis at hand was carried out in the period from March 2013 to May 2016 at the Center for Individual Nanoparticle Functionality (CINF) at the Technical University of Denmark (DTU). I would like to acknowledge The Danish National Research Foundation's Center for Individual Nanoparticle Functionality (DNRF54) for funding this work. The daily work was supervised by Prof. Ib Chorkendorff with regular assistance from Prof. Ole Hansen and Assoc. Prof. Peter C.K. Vesborg through weekly meetings, discussions, and feedback. It has been a privilege to work with and learn from such distinguished professors. Countless practical challenges were overcome by assistance from the untiring help of floor managers Robert Jensen and Kenneth Nielsen.

At CINF, I have had the pleasure of colleagues and collaborators at several research institutions. It has been an honour to work with talented and professional colleagues from some of the best research groups in the field. They have made my work place truly enjoyable, with friendships that last beyond the boundaries of work. A word of gratitude to Thomas Pedersen, Marian D. Rötzer, Florian F. Schweinberger, Ulrik G. Vej-Hansen, Anders Bodin, Daniel B. Trimarco, Claudie Roy, Ann-Louise N. Christoffersen and Sine E. Olesen. I especially thank Béla Sebök for sparing, hard and dedicated work in the lab and being a supportive friend through many challenging experiments.

I would like to thank my family; Birte N. Riedel, Werner Riedel, and Agnete N. Riedel, for always being supportive in my studies and carrier.

Lastly, I owe a debt of gratitude to Helene Kolding; for being my partner and closest friend, for incredible support during work, both practicalities in our daily life, scientific sparing, providing feed back for my thesis, but

most importantly for making my life so enjoyable and making me a better version of myself.

Abstract

The work of this thesis revolves around catalytic activity measurements of nano-particles tested using a μ-reactor platform, developed and produced at DTU, in a collaboration between CINF and Nanotech.
The thesis contains the results from two separate research projects; both utilising μ-reactors in combination with surface science techniques and computer simulations. The first project described is a study of hydrogen dissociation on mono-disperse platinum clusters. The second project studies methanation from carbon monoxide and hydrogen on nano-particles of nickel-iron alloys. The second study is a work in progress, and the corresponding chapter aims to summarise the results so far. Other projects are not included in the thesis because they are inconclusive or dead ends.
Hydrogen dissociation was studied by the H_2/D_2 exchange reaction on SiO_2-supported mono-disperse platinum clusters in a μ-reactor. The reaction was tested under ambient pressures and temperatures ranging from room temperature to 180 °C. The initial ambition was to study size effects on the chemical activity of clusters, but experimental challenges prevented a final conclusion on cluster size effects. Using Pt_8 cluster samples it was found that minute amounts of oxygen present in the gas stream would change the clusters ability to dissociate hydrogen. Reaction products were analysed with quadrupole mass spectrometry. The catalyst was characterized before and after chemical testing using XPS and ISS, proving the catalyst to be highly stable. DFT simulations demonstrated that even a single oxygen atom binds strongly to SiO_2-supported Pt_8 clusters and changes the morphology and chemical properties of the cluster.
Catalytic methanation reaction from CO and H_2 was studied on $Ni_{75}Fe_{25}$ nano-particles with sizes 3.5 nm, 5 nm, 7 nm and 9 nm. The presented

data is a work in progress, but initial results show a tendency of 7 nm particles being most active. The catalyst is characterized before and after chemical activity measurements using ISS, XPS, and SEM to ensure a clean surface and consistent deposition. Plans for the immediate future involve reproducing activity measurements on all sample sizes and more consistent characterisation with ISS and XPS. An ambitious plan is to do a similar size study on pure nickel nano-particles, to examine differences and similarities between the catalysts under reaction conditions.

Resumé

Denne ph.d.-afhandling omhandler måling af katalytisk aktivitet af nanopartikler ved brug af en μ-reaktor-platform. μ-reaktoren er udviklet på DTU i et samarbejde mellem CINF og Nanotech.
Resultaterne præsenteret i denne afhandling er opdelt i to forskningsprojekter hvor begge gør brug af μ-reaktoren i kombination med metoder kendt fra eksperimentiel overfladefysik og computersimulering. Det første projekt er et studie af molekylær brint, der deler sig på masse-selekterede platin-klynger. Det andet projekt studerer methanudvikling fra brint og kulilte på nanopartikler bestående af nikkel-jern-legeringer. Det sidstnævnte projekt er igangværende, og de foreløbige resultater bliver opsummeret. Andre forskningsprojekter er ekskluderet fra afhandlingen da resultaterne ikke er entydige eller endt i en blindgyde.
Brintdissociationsstudier blev udført med H_2/D_2 udveksling på SiO_2-supporterede platin-klynger i en μ-reaktor. Reaktionen foregik under 1 bar og temperaturer fra stuetemperatur til 180 °C. Projektets oprindelige intention var, at studere størrelseseffekter på platin-klynger, men det viste sig udfordrende at reproducere de indledende resultater. Med udgangspunkt i Pt_8 klynger blev det påvist, at små mængder ilt i gasstrømmen kan ændre katalysatorens evne til at splitte brint. Produkter blev analyseret med quadrupol masse-spektrometri og katalysatoren blev karakteriseret med XPS og ISS, som fandt at klyngerne var stabile under reaktionen. DFT simuleringer viste at klyngen binder sig stærkt til SiO_2 og at atomart ilt på en Pt_8 klynge vil ændre klyngens morfologi og kemiske egenskaber.
Udvikling af methan fra kulilte og brint blev studeret på nanopartikler bestående af $Ni_{75}Fe_{25}$ og i størrelserne 3.5 nm, 5 nm, 7 nm og 9 nm. Projektet er endnu ikke færdigt og resultaterne er et øjebliksbillede af den

nuværende viden, hvor 7 nm partikler er mest aktive. Partiklerne er karakteriseret før og efter kemiske aktivitetsmålinger med XPS, ISS og SEM. Projektets fremtidige planer er at genskabe det nuværende data med en mere konsistent karakterisering med XPS, ISS og SEM. Som supplement er der startet et ambitiøst projekt om at sammenligne nikkel med $Ni_{75}Fe_{25}$ ved brug af aktivitetsstudier for at undersøge ligheder og forskelle.

Contents

List of publications

Paper I, page 109

H_2/D_2 exchange reaction on mono-disperse Pt clusters: Enhanced activity from minute O_2 concentrations

Jakob Nordheim Riedel, Béla Sebök, Elisabetta Maria Fiordaliso, Alexander Krabbe, Anders Bodin, Thomas Pedersen, Christian Danvad Damsgaard, Jakob Birkedal Wagner, Peter Christian Kjærgaard Vesborg, Ole Hansen, and Ib Chorkendorff

Submitted, 2016

Paper II, page 117

Methanation on size-selected $Ni_{75}Fe_{25}$ nano-particles

Jakob Nordheim Riedel, Béla Sebök, Elisabetta Maria Fiordaliso, Alexander Krabbe, Thomas Pedersen, Christian Danvad Damsgaard, Jakob Birkedal Wagner, Peter Christian Kjærgaard Vesborg, Ole Hansen, and Ib Chorkendorff

In preparation

List of abbreviations and symbols

Abbreviations

BV buffer volume

CINF Center for Individual Nanoparticle Functionality

CV containment volume

DC direct current

DFT density functional theory

DTU Technical University of Denmark

FWHM full width at half maximum

GHSV gas hourly space velocity

HSA hemi-spherical analyser

ISS ion scattering spectroscopy

LEIS low-energy ion scattering

MC main chamber

MFC mass flow controller

ML monolayer

QMS quadrupole mass spectrometer

RF radio frequency

RP	roughing pump
RT	room temperature
RTD	resistance temperature detector
SEM	scanning electron microscope
TC	thermocouple
TP	turbo pump
TPD	temperature programmed desorption
TPR	temperature programmed reaction
TUM	Technische Universität München
UHV	ultra high vacuum
XPS	X-ray photoelectron spectroscopy

Symbols

α	heating coefficient
$\bar{p}$	mean pressure
$\dot{N}_{\mathrm{int}}$	gas flow in intermediate flow regime
$\dot{N}_{\mathrm{vol}}$	volumetric flow
$\dot{N}_{\mathrm{mol}}$	gas flow in molecular flow regime
η	viscosity
λ	molecular mean free path
ω	angular frequency
ϕ	potential distribution

σ	initial adsorbate concentration
φ	work function
A	pre-exponential factor
a	tube radius
c_{int}	flow conductance in intermediate flow regime
c_{mol}	flow conductance in molecular flow regime
d	tube diameter
E_{act}	activation energy
E_{des}	desorption energy
E_{f}	final ion energy
E_{i}	initial ion energy
K	equilibrium constant
k	reaction rate
k_{B}	Boltzmann constant
l_{int}	length of capillary with intermediate flow
l_{mol}	length of the capillary with a molecular flow
l_{total}	total capillary length
m	molecular mass
p_1	pressure at tube inlet
p_2	pressure where λ is comparable with d
p_3	pressure at tube outlet

R	gas constant
r_0	distance between the center axis and the rods
s	molecular diameter
T	temperature
t	time
T_p	desorption-peak maximum temperature
U	DC potential
u	either x or y
V	RF potential
v	molecular velocity
v_n	rate constant
V_reactor	reactor volume
x	spatial coordinate
y	spatial coordinate

List of Figures

List of Tables

Chapter 1

Introduction

1.1 Uses of heterogeneous catalysis

The field of heterogeneous catalysis dates back more than a century [1–3] and is today a massive industry, playing a key role in the production of fertilizer [4], oil refinery [3, 5], polymers [3], and many other reactions that modern society relies heavily on [2]. Catalysis also plays a major role in the future of sustainable energy [3], including power-to-gas conversion, i.e. methanation from H_2, CO_2, and electricity to CH_4 for storage and transportation [6, 7].

1.2 Bridging the pressure gap with μ-reactors

Many modern industrial catalysts are developed by trial and error (happy chance). However, a fundamental understanding require studies of catalysts by surface sensitive techniques [8]. These often require low pressures. ultra high vacuum (UHV) techniques [8, 9] combined with computational simulations allow fundamental knowledge of surface reactions [10]. There is a need to demonstrate that the results of UHV experiments at 10^{-13} mbar to 10^{-7} mbar are relevant at industrial reaction conditions of 1 bar to 10^2 bar. This is commonly referred to, as bridging the pressure gap [11, 12]. Another important step between early fundamental studies and industrial applica-

tions include bridging the material gap from single crystal to industrial catalyst [12, 13].

One important step in bridging the material gap is cluster sources [14–17]. Industrial catalysts use nano-particles on porous supports. Cluster sources are a highly advantageous method for making clusters and nano-particles, because important parameters like compounds, stoichiometry and size can be controlled. The nano-particle fabrication is very expensive, but constitute well defined model systems that imitate that of an industrial catalyst. However, an inherent limitation of these systems is the low catalyst yield, that makes activity testing at industrial pressures difficult. By utilizing a very low reactor volume, the μ-reactor [18] used in the thesis allows the well defined model systems to be tested at pressures up to 2.5 bar, thereby acting as a bridge between UHV studies on model systems and industrial catalysts.

Some important differences between industrial- and μ-reactor catalyst means that several issues still need to be addressed to truly bridge the materials- and pressure-gap. Industrial catalysts are chemically synthesized where the model catalyst is mass selected in the gas phase. The catalyst support of the μ-reactor is flat SiO_2 while industrial catalysts have a three-dimensional porous support. The longest μ-reactor experiments last a few weeks while industrial catalysts sometimes run for decades, suggesting that stability tests are difficult to truly address in the μ-reactor. All these issues each constitute an entire field of research, not touched upon in this work.

1.3 Thesis outline

The experiments described in this thesis are concentrated around the μ-reactor. However, several characterization experiments where conducted to gain meaningful knowledge of the catalyst. For this reason the projects are made in collaboration between several people in different research groups. Most experiments using the μ-reactor were done by me. I also conducted

or assisted with some characterisation experiments. All experiments not done by me are clearly stated.

Chapter 1 Introduction to the field of catalysis and how the μ-reactor compliments the current forefront of surface science.

Chapter 2 An exposition of experimental equipment used in this thesis. Particular emphasis is placed on the μ-reactor design and capabilities.

Chapter 3 H_2/D_2 exchange reaction on mono-disperse platinum clusters.

Chapter 3 Methanation on size selected $Ni_{75}Fe_{25}$ nano-particles.

Chapter 4 Conclusion and outlook.

Chapter 2

Experimental foundation

The experiments described in this thesis are a result of collaborations between several people located at different universities around the world, i.e. Technische Universität München (TUM), and three different institutes at the Technical University of Denmark. A description of equipment and procedures will be given in this chapter.

2.1 μ-reactors

The μ-reactor used throughout this thesis is a silicon based chip developed at DTU in collaboration between DanChip and CINF, first published in 2009 [18]. Being roughly the size of a post stamp, these reactors provide several advantages to conventional reactors. The primary advantage is a very small reactor volume of 236 nL that allows a high gas hourly space velocity (GHSV) while testing minute amounts of catalyst. This is essential for size selected clusters and nano particles formed in cluster sources, since the yield is extremely low. In this thesis we demonstrate significant chemical activity on as little as 4.6 ng platinum. The chip design directs all chemical products into a small UHV chamber equipped with a quadrupole mass spectrometer (QMS). This gives a high sensitivity and a fast time response while analysing chemical products. Since the chip has a low mass, the thermal time response is very fast. Heating to 400 °C from room temperature in a few seconds

provides an almost instant reaction with adsorbed chemicals. This is used to estimate surface areas or contamination levels of a catalyst and measure temperature programmed desorption (TPD) [19].

Several silicon based μ-reactor set-ups are used at DTU, CINF. A μ-reactor for photo catalysis [20], a liquid phase electrochemical reactor [21], and a μ-reactor utilizing time of flight mass spectrometry for increased sensitivity [22] are being used. Here, a detailed description of the two μ-reactor set-ups for heterogeneous catalysis used throughout this thesis is presented.

2.1.1 Old μ-reactor

The μ-reactor is the backbone and workhorse of this thesis. The silicon chip depicted in figure 2.1 is the so-called old reactor design which was used for the majority of my PhD project. Figure 2.1a shows the front side of the reactor chip that measures 20 mm × 16 mm.

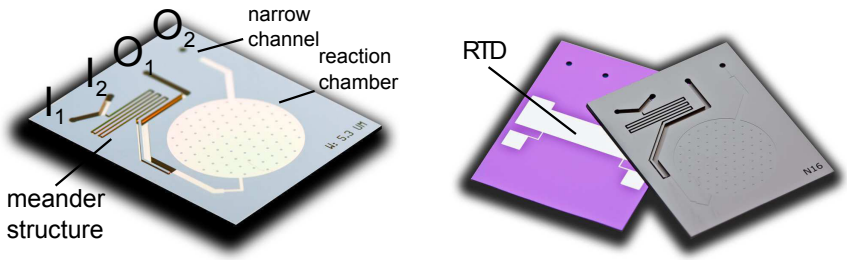

(a) Front side of the μ-reactor.

(b) Front and back side of the reactor chip.

Figure 2.1. Old μ-reactor design. The two inlets, I_1 and I_2, allow gasses into the reactor. O_1 is an outlet leading to the pressure controller and O_2 leads from the reactor volume to the QMS. The reactor design is distinct from the NG design (described below) by being shorter in length and only having a single resistance temperature detector (RTD) that also functions as heating element. Also, it does not have a Pyrex spacer on the backside to thermally insulate the chip from the interface block. Photos by Thomas Pedersen.

Chip design

The two gas inlets, I_1 and I_2 in figure 2.1a, allow different reactants into the gas channels of the chip. A meander structure mixes the gases that are otherwise in a laminar flow regime. From this point a small fraction of the gas stream enters the reaction chamber where a catalyst is deposited. Reaction products flow through the narrow capillary, described in section 2.1.5, and exit through outlet O_2 into a UHV chamber containing a QMS. Most gas never enters the reaction chamber, but exits through O_1 and is used to regulate the pressure inside the reactor. The back side of the reactor, seen in figure 2.1b, contains holes for the inlets and outlets together with a four point probed resistance temperature detector (RTD) that also functions as a heating element. A set of gold plated pogo pins ensure the contact to the platinum pads and a constant current is put through a platinum thin film. Two probing pads are used to measure the potential drop across the RTD to calculate the resistance of the platinum. Since the resistance of the metal increases with temperature, this is used as a highly sensitive thermometer. A thermocouple (TC) is placed on top of the reactor, above the reactor volume, as a backup measurement of the temperature.

Gas handling

Figure 2.2 shows a schematic drawing of the gas handling system and equipment surrounding the μ-reactor (yellow). Blue tubes contain pressures of ∼2.5 bar but can be pumped down by the buffer volume (BV) when changing to other gases. A network of green tubes and chambers are pumped by a turbo pump (TP) and roughing pump (RP) combo and can reach UHV. The main chamber (MC) contains a QMS and has the sole purpose of analysing reaction products. The BV is used to pump residual gases from the μ-reactor and tubes. A relatively large volume is used to gradually expand large amounts of gas when pumping down the reactor

without overloading the TP. A pressure controller (PC) at O_1 determines the pressure in the reactor. A total of six gas lines with mass flow controllers (MFC) provide the reactants for inlets I_1 and I_2. Hourglass shapes represent valves, black being manual and grey are pneumatic.

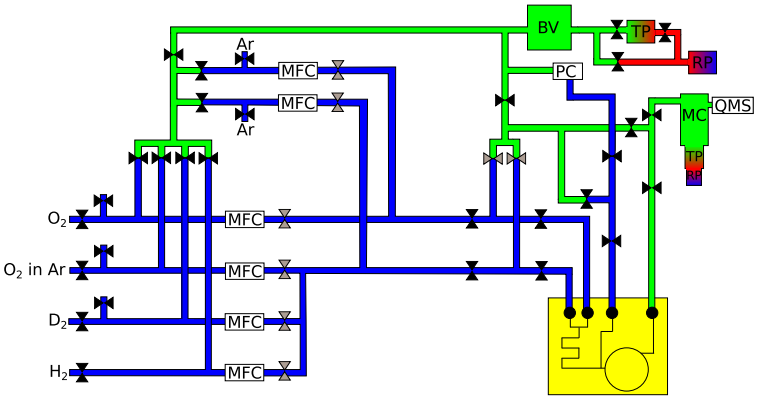

Figure 2.2. Schematic drawing of gas handling and spectroscopic equipment surrounding the μ-reactor (yellow). Six gas lines fitted with MFCs provide the reactants to the μ-reactor. The MC analyses the reaction products while the BV and PC takes care of pressure in the reactor. Blue gas lines can contain high pressure gasses while green gas lines are pumped by the BV. Black and grey hourglass shapes represent manual and pneumatic valves, respectively. Adapted from [19].

The interface between silicon chip and the gas handling system is done by a stainless steal interface block. This transition is sealed with small Viton O-rings. Since Viton is never completely leak tight the O-rings are constantly flooded with argon. A small contamination of argon is always present in the reactor but is insignificant to the chemical reaction. This leads to a non-neglectable background in the QMS on $m/z = 40$ and 20.

Set-up improvements

For the H_2/D_2-exchange reaction (experiments described in chapter 3) it proved necessary to make a few alterations on the set-up. The two Ar lines in figure 2.2 were added to the four existing lines, allowing five different gases dosed during the H_2/D_2-exchange reaction experiments. This reaction

also proved highly sensitive to relative dosage amounts that could come from badly calibrated MFCs. To limit unknown parameters all MFCs were exchanged with digitally controlled ones and calibrated anew. Pneumatic valves from the two inlet gas lines to the BV also allows automatic pumping directly on these lines, dramatically reducing residual gases in the system. These alterations allowed dosage of dilute O_2 in Ar as an additional gas, leading to the findings on O_2 effects on Pt clusters.
The latest upgrade to the set-up was upgrading the heater design and the pogo pin set to match that of the μ-reactorNG, allowing the same samples to be used on both set ups and improving heating on the old set-up.

2.1.2 μ-reactorNG

The NG in μ-reactorNG stands for next generation and was build with improvements on the old design. The reactor chip, as seen in figure 2.3, is made longer (16 mm × 27 mm) to accommodate a more advance heater design seen in figure 2.3b. As opposed to the old reactor design that had an integrated heater and RTD, the μ-reactorNG has a separate four point RTD going through the middle of the reactor volume. The platinum film is more narrow giving a higher electrical resistance that is easier to measure. Two heaters symmetrically around the RTD provide a more homogeneous heating of the reactor. At the gas inlets a Pyrex spacer is fitted. This is done to thermally insulate the chip from the stainless steel interface block. In figure 2.3a the front of the reactor shows five spots in the reactor volume. These are small grids that are etched out in the reactor volume, shown in figure 2.4. Each grid has coordinates that allow SEM imaging at identical locations before and after testing. The smallest square features are 6 µm × 6 µm and make it easier to navigate the chip with SEM images. The schematic drawing of the gas handling system shown in figure 2.5 has a few modifications to that seen in figure 2.2. Most noticeably is the containment volume (CV) around the the reactor chip. This is a pragmatic solution to the problem of leaking O-rings. Instead of flooding the inlets

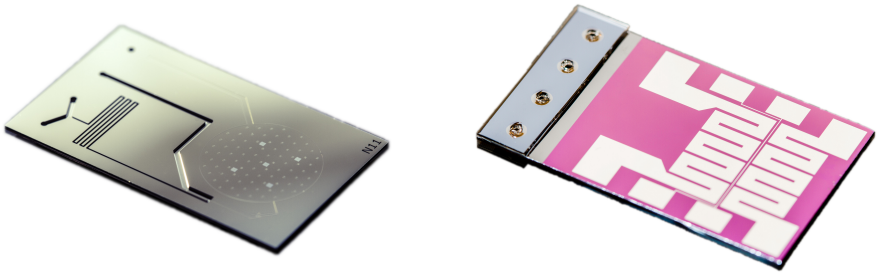

(a) Front side of the μ-reactor with SEM grid.

(b) Backside of reactor. A more sophisticated heater design is used with a dedicated four point RTD and two separate heating elements.

Figure 2.3. Newest μ-reactorNG design. The longer design allows an elaborate heater design. Photos by Thomas Pedersen.

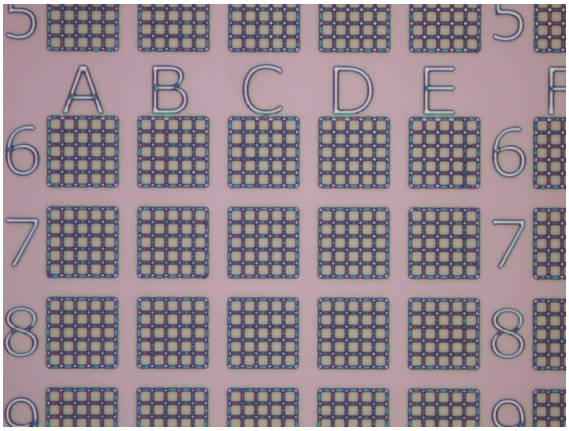

Figure 2.4. Microscopy image of SEM grids. The small square features are 6 µm × 6 µm. Photo by Thomas Pedersen.

with Ar the entire surroundings are pumped to low pressures, eliminating the need for a constant Ar flow. Another improvement made during this study is an additional pneumatic valve between the BV and the TP. This valve is significantly larger and provides a faster pumping of the μ-reactor and gas lines once the pressure is low enough. The main advantage is while pumping down a newly mounted sample. This process would take an entire work day or be done over night, but can now be done in less than an hour.

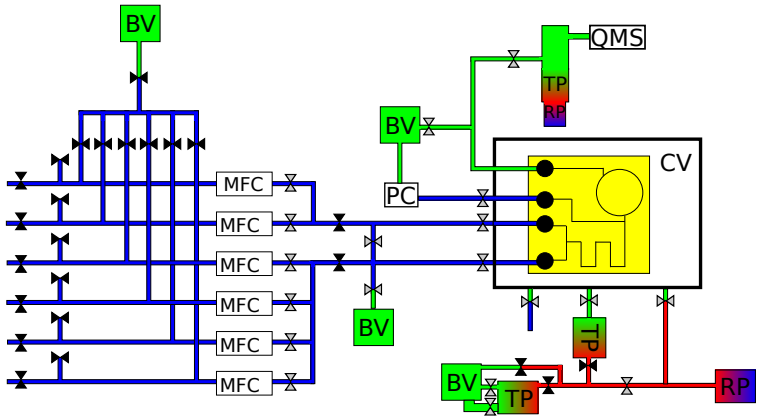

Figure 2.5. Schematic drawing of gas handling of the μ-reactorNG set up. The biggest difference is the containment volume (CV) surrounding the reactor chip. Adapted from [19].

2.1.3 Heat distribution

As mentioned, going from the "old" μ-reactor to the NG version has included a larger power input and better heating distribution, which leads to improved heating capabilities. The heat distribution was measured using an infra-red camera to image the top of a bonded reactor.

Heating of old μ-reactor

The heat distribution of the old μ-reactor is shown in figure 2.6. The heat profile is taken along the middle of the reactor chip and the black bars indicate the position of the reactor volume. At high temperatures there is a significant thermal gradient resulting in temperature gradients of ∼30 °C within the reactor volume. This is a clear problem since the temperature dependency of chemical reactions is exponential. Luckily, this problem becomes smaller at lower temperatures. All experiments involving the old μ-reactor design are done at a maximum temperature of 180 °C and most experiments are well below that.

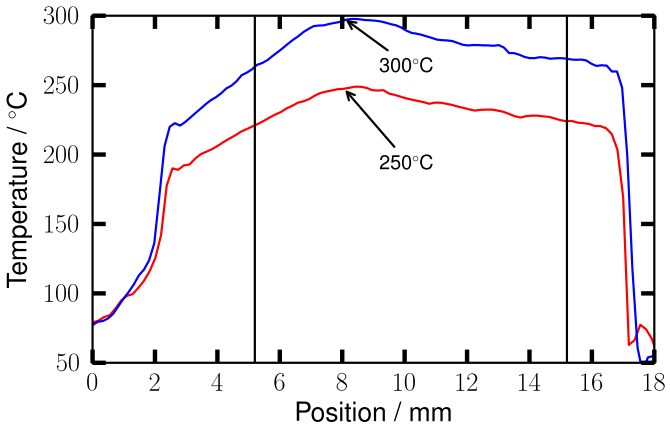

Figure 2.6. Heat distribution profile of the old μ-reactor captured with an infrared camera. It is taken along the middle of the reactor chip. The two black bars indicate the position of the reactor volume. Reprinted from [19].

Heating of μ-reactorNG

The heater design has been improved at several iterations. The latest heater design is shown in figure 2.3b. The two heaters are symmetrically placed under the reactor volume, and it was first thought that an 1:1 power distribution would give an even heat distribution. A temperature profile is seen in figure 2.7 where the sample is heated to 200 °C. The thermal image is shown in grey scale, the blue line shows the temperature profile, the reactor volume is marked by a green circle and the RTD is shown as a red bar. The optimal power distribution was found to be 2:1 with most power on the heating element closest to the interface block. This is because the primary heat loss comes from thermal conduction to the interface block, while the effects of radiation are very limited at these temperatures. To reduce heat loss, a piece of Pyrex was bonded to the part of the reactor in contact with the interface block, effectively insulating the reactor chip. However, the heat distribution seen in figure 2.7 is with this Pyrex spacer added. Most of the reactor volume has a homogeneous

temperature, but with a large gradient of ∼20 °C towards the interface block. A suggestion for improving the heat distribution is to make the heating element closest to the interface block extend further away from the reactor volume and thereby compensate for the conductive heat loss. The temperature measured by the infra-red camera was ∼10 °C higher than the RTD. This is highly peculiar since all possible explanations for a misreading would result in a lower temperature. The camera readout is of the Pyrex, which is thermally insulating compared to silicon. The emissivity is also set to 1 on the camera, meaning that any real material would look colder in the thermal camera. However, the relative changes in temperature are deemed real and the errors are therefore less important.

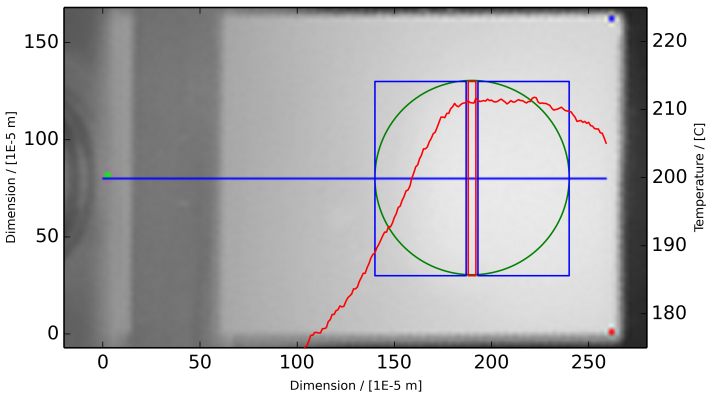

Figure 2.7. Heat distribution of the μ-reactorNG at 200 °C captured with an infra-red camera. The thermal image is in grey scale. The green circle shows the position of the reactor volume while the blue line indicates the location of the thermal gradient read-out. The red bar shows the temperature read-out of the thermal camera. Figure by Anders Nierhoff.

Logging of power input

Lately the input power of the reactor is logged together with other measurements during experiments. This will help troubleshooting in case one

heater or the RTD looses electrical contact. An example of the input power shown together with measured temperature is shown in figure 2.8. In some cases the electrodes can loose contact to the platinum pads on the backside of the reactor. If one heater looses contact the temperature at the RTD will drop. The regulation will then increase the power through the other heater, keeping the RTD at a constant temperature. Counter-intuitively, the overall chemical activity will increase when a heater is lost, because of the exponential temperature dependence of the reaction. If the electrical contact to the RTD is unstable, large spikes in temperature can occur, and the catalyst can be briefly heated to high temperatures. This is because the principle of four point resistance measurements rely on the system being in equilibrium. But if the system is momentarily brought out of equilibrium, the resulting resistance can vary a lot. Sometimes the RTD is also damaged during experiments, providing an altered resistance. These sources of error are usually easily detected as inconsistent RTD measurements, or by the TC place on top of the reactor.

2.1.4 Anodic bonding

The reactor chips are sealed with a Pyrex lid using anodic bonding, also known as field-assisted thermal bonding [23, 24]. This process benefits from making a chemical bond between the silicon chip and Pyrex lid, effectively sealing the reactor volume and gas channels. The basic concept is sketched in figure 2.9 where the μ-reactor with Pyrex lid is heated on a grounded hot plate. A cathode set to $-1\,\mathrm{kV}$ induces an electric field between the reactor and lid. Sodium in the Pyrex is made mobile and ionized by the heat, and the electric field accelerates it towards the cathode. This leaves a charged region in the Pyrex/silicon interface that pulls them into intimate contact. High temperatures (in our case $\sim 450\,^{\circ}\mathrm{C}$) make covalent bonds in the interface that seals the reactor.

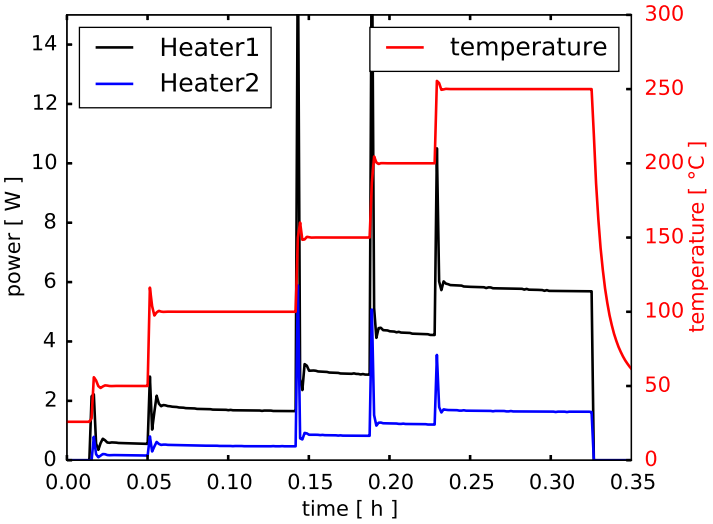

Figure 2.8. Power put into the μ-reactor chip during heating. Heater 1 is closest to the interface block and heat losses will be highest there. This is the reason why the power is higher for that heater. The temperature is measured by the RTD and shown in the right axis in red.

Cold bonding

While the method provides excellent sealing of the reactor, temperatures of ∼450 °C will sinter most catalysts and make prior mass selection of particles redundant. For this reason the cold bonding setup was invented. This actively cools the reactor area while heating the surrounding chip to allow bonding. Figure 2.10 shows a finite element analysis of heat in the system. A water cooled copper block is placed under the reactor volume while an aluminum block heats the rest of the chip. It ensures that the catalysts stays sufficiently cool during bonding.

Opening reactors

Anodic bonded Pyrex lids provide a practical solution to the problem of sealing the reactor. However, they drastically limit the possibility of doing spectroscopic analysis of the catalyst and reactants during chemical reaction.

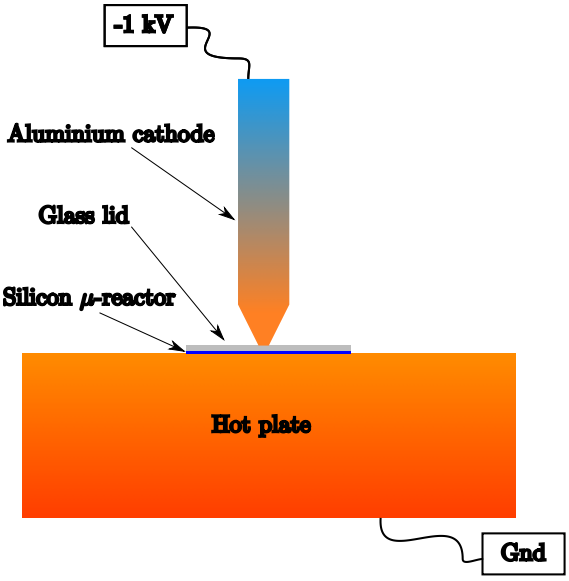

Figure 2.9. Schematic drawing of anodic bonding. A cathode set at −1 kV provides the electric field while a grounded hot plate ensures the chemical bonding between Pyrex lid and μ-reactor. Adapted from [23].

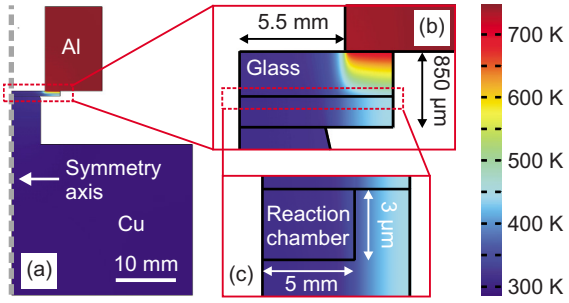

Figure 2.10. Finite element simulation of heat profile during cold bonding. A water cooled copper block cools the reactor volume while an aluminum block heats the rest of the chip for anodic bonding. Reprinted from [23].

Attempts have been made to use thin Pyrex lids and do *in situ* grazing incidence small angle scattering [25]. However, sufficiently thin lids were not available and proved impossible to produce. The next best thing to *in situ* spectroscopy is analysis before and after reaction. XPS, ISS, and SEM

have been used in this study, and characterisation pre- analysis is straight forward. To analyse the catalyst post-reaction is a bit trickier because the reactor is sealed tight. The only solution was to break open the reactor. By using a diamond saw the lid can be cut open. To avoid water contaminating the surface the Pyrex lid was only mostly cut through but leaving ∼35 µm as seen in figure 2.11a. By glueing a copper gasket to the Pyrex on top of the reactor it was possible to break open the reactor as seen in figure 2.11b. This allowed for characterisation of the surface post-reaction but effectively ruining the reactor chip and preventing further experiments to be done.

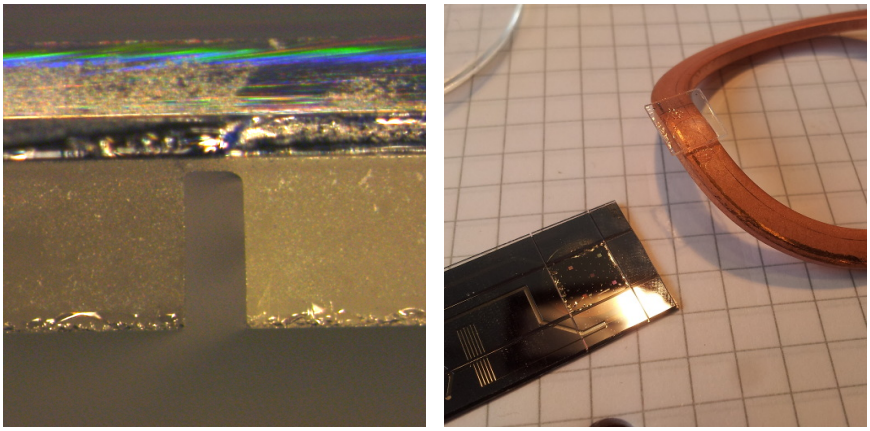

(a) Pyrex partially cut through. Photo by Thomas Pedersen.

(b) Reactor opened by breaking off cut out.

Figure 2.11. By partially cutting the Pyrex lid the reactor could be opened be breakage. This prevented contamination of the surface and left the silicon chip intact.

2.1.5 Reactor gas flow

To limit the gas flow from the reactor volume, containing up to 2.5 bar, to the UHV chamber, a narrow capillary is placed in between. The gas flow from the reactor volume through the capillary and into the QMS is important to understand, because some noticeable artefacts of the total gas flow arise from the properties of the capillary and the gases flowing

through it.

A gas flow through a narrow capillary with a high pressure on the inlet side and a UHV on the outlet can be described mathematically [18, 26, 27]. The Knudsen number, λ/d, denotes the ratio between the mean free path of the molecule, λ, and the diameter, d, of the tube. A Knudsen number above 110 gives a viscous flow, where a Knudsen number below 1 causes a molecular flow. For pressures and gases used in the μ-reactor the Knudsen number never reaches values above 110. This means we go from an intermediate flow to a molecular in the narrow capillary.

A schematic of a capillary is shown in figure 2.12 with pressures p_1 at the inlet and p_3 at the outlet. High pressures cause an intermediate gas flow at first, as indicated. The pressure drop across the capillary will increase the mean free path, λ , of gas molecules. At the pressure, p_2 where λ is comparable with the diameter of the capillary, the intermediate flow changes to a molecular flow. This can be written as

$$p_2 = \frac{k_B T}{\sqrt{2}\pi s^2 a} \tag{2.1}$$

where k_B is the Boltzmann constant, T is the temperature, s is the molecular diameter, and a is the capillary radius.

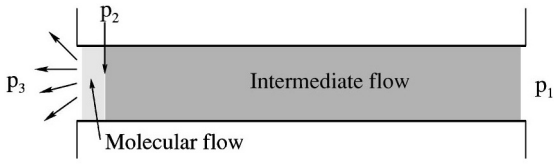

Figure 2.12. Schematic drawing of gas flow through narrow capillary. The pressure drop introduces three critical points of pressure and two flow regimes, i.e. the high pressure, p_1, at inlet, low pressure, p_3, at outlet, and the pressure, p_2, where the flow changes from intermediate to molecular. Reprinted from [28].

The flow in the intermediate flow regime, $\dot{N}_{\text{int}}$, is given by [26]

$$\dot{N}_{\text{int}} = c_{\text{int}} \frac{1}{l_{\text{int}}} \frac{p_1 - p_2}{k_B T} \tag{2.2}$$

where the intermediate flow conductance, c_{int}, is given by

$$c_{\text{int}} = \frac{\pi}{8}\frac{\bar{p}a^4}{\eta} + \frac{8}{3}\sqrt{\frac{\pi}{2}}\frac{a^3}{v}\frac{1+2\frac{av\bar{p}}{\eta}}{1+2.48\frac{av\bar{p}}{\eta}} \tag{2.3}$$

Here, $\bar{p} = (p_1 + p_2)/2$, η is the viscosity, l_{int} is the length of the part of the capillary with intermediate flow, $v = \sqrt{m/k_{\text{B}}T}$, and m is the mass of a single molecule.

Gas flow in the molecular flow regime is given by [27]

$$\dot{N}_{\text{mol}} = c_{\text{mol}}\frac{1}{l_{\text{mol}}}\frac{p_2 - p_3}{k_{\text{B}}T} \tag{2.4}$$

with

$$c_{\text{mol}} = \frac{8}{3}\sqrt{\frac{\pi}{2}}\frac{a^3}{v} \tag{2.5}$$

where l_{mol} is the length of the capillary with a molecular flow regime. Using equations 2.2, 2.3, 2.4, and 2.5 while noting that $l_{\text{total}} = l_{\text{mol}} + l_{\text{int}}$ gives the total flow through the capillary

$$\dot{N} = \frac{1}{k_{\text{B}}T}\frac{1}{l}\left(c_{\text{int}}(p_1 - p_2) + c_{\text{mol}}(p_2 - p_3)\right) \tag{2.6}$$

This yields a complicated equation dependent on many parameters. During experiments it is possible to control temperature, pressure, and gas composition. It is important to realize that all these parameters determine the gas flow, and particularly temperature and gas composition has a substantial influence compared to conventional test reactors. Increasing the pressure in the reactor therefore increases the flow through the reactor. Heating the reactor will decrease the gas flow. This is significant since a typical experiment will have varying temperatures during reaction and therefore varying gas flow. This also changes the molecular residence time in the reactor and therefore the reactant conversion factor.

This allows us to calculate the gas hourly space velocity as

$$GHSV = \frac{\dot{N}_{\mathrm{vol}}}{V_{\mathrm{reactor}}} \tag{2.7}$$

where $\dot{N}_{\mathrm{vol}}$ is the volumetric flow and the volume of the reactor, V_{reactor}, is 236 nl. For air at room temperature (RT) and 1 bar this corresponds to a $GHSV$ of $\sim 330\,\mathrm{h}^{-1}$. This might seem like a small value, but the catalyst is dispersed over only $0.79\,\mathrm{cm}^2$ of SiO_2 support. These same conditions give rise to a residence time of $\sim 12\,\mathrm{s}$ and a reactor throughput of $0.43\,\mathrm{nmol\,s}^{-1}$.

2.1.6 Temperature programmed techniques

The basic working principle behind TPD is to dose a gas onto a surface, then heat it gradually to high temperature and measure a surface species desorb. At a given temperature the adsorbate will desorb, corresponding to the binding energy of that specific atom or molecule. A temperature programmed reaction (TPR) is very similar, but involves a chemical reaction between either multiple pre-adsorbed surface species or a surface species and a reactant in the gas phase.

A TPD can be used to identify surface cites of a catalyst. A homogeneous surface will have one broad peak corresponding to the adsorption properties of one specific surface site. If the surface has both kinks, corners, and broad planes the TPD will show several peaks accordingly.

The desorption rate is described as zero-, first-, or second-order desorption, as described by the following equations, respectively [2]:

$$\frac{E_0}{R} = \frac{v_0}{\sigma\alpha}\exp\left(-\frac{E_0}{RT_{\mathrm{p}}}\right) \tag{2.8}$$

$$\frac{E_1}{RT_{\mathrm{p}}^2} = \frac{v_1}{\alpha}\exp\left(-\frac{E_1}{RT_{\mathrm{p}}}\right) \tag{2.9}$$

$$\frac{E_2}{RT_{\mathrm{p}}^2} = \frac{v_2\sigma}{\alpha}\exp\left(-\frac{E_2}{RT_{\mathrm{p}}}\right) \tag{2.10}$$

where E_{des} is the desorption energy, R is the gas constant, v_{n} is the rate constant, σ is the initial adsorbate concentration, T_{p} is the desorption-peak maximum temperature, α is the heating coefficient, and the subscript denotes the desorption order. From the equations it is seen that a zero-order desorption T_{p} increases with the initial adsorbate coverage, σ, while it is constant for a first-order desorption, and decreases with a desorption of second-order. From this it is possible to determine activation energy and pre-exponential factor of each surface site [29].

In the μ-reactor a TPD is done by dosing a gas of choice, often CO is used, in the reactor, pumping out the gas, flushing with Ar, and then heating the reactor in a constant flow of Ar and high pressures, usually 1 bar. The Ar flushing is done to clean all gas lines for residual gases. The Ar flow during TPD is used as a carrier gas to transport desorbing gases to the QMS for analysis. A H_2-TPR is done in the same manner, but exchanging Ar with H_2 during heating.

2.2 UHV techniques

Many experimental techniques require very low pressures in order to work. This is mainly due to the necessity of a high mean free path of electrons and ions attainable at pressures below 10^{-4} mbar. Surface characterization is also highly sensitive to background pressures if a clean surface is required. The number of molecules bombarding a single surface atom can be estimated by kinetic gas theory to be once per second at $\sim 10^{-6}$ mbar. This relates to the unit Langmuir (L) that is defined as the exposure of a surface to a single ML of gas. UHV is defined as being below 10^{-9} mbar, providing both high mean free paths for experimental techniques and clean surfaces for roughly an hour for reliable characterisation [30].

2.2.1 QMS

QMSs are widely used in industry and research to analyse gas compositions. The technique is a vital part of the μ-reactor set-up as it is used to measure the activity and other properties of the catalyst.

Mass selection

As the name suggests the main operational part of a QMS are four metallic poles, shown schematically in figure 2.13. They are ∼15 cm long and are responsible for the actual mass selection of ions. To the left of the rods is an ion source, usually a filament that ionises incoming gas. To the right is an ion detector, in our case a secondary electron multiplier. Opposing rods are electrically connected pairwise and each pair constitute a low-mass or high-mass pass filter.

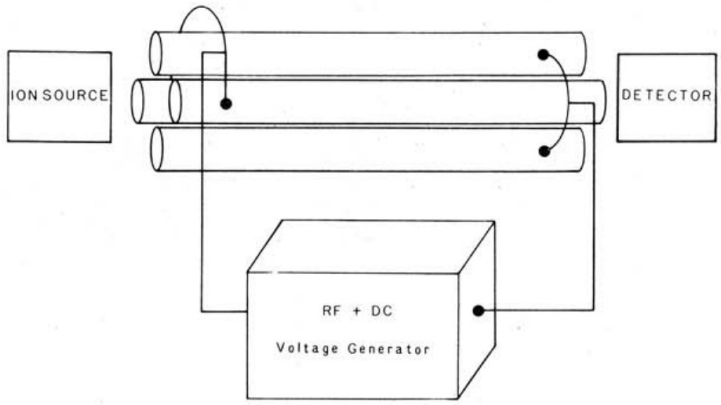

Figure 2.13. Sketch of the quadrupole rods of a QMS. The four rods are pairwise electrically connected to an RF and DC generator. The ion source of a conventional QMS is a filament while the detector consists of a secondary electron multiplier. Reprinted from [31].

A pair of rods will have a radio frequency (RF) potential applied. Ions travelling between the rods will start to oscillate, while the rods are positive they will repel positively charged ions and focus them to the center and when they are negative the ions will be attracted towards the rods. Whether

an ion will collide with the negatively charged rods and be neutralized is a function of the magnitude and time dependence of the electric potential and also the mass of the ion. Lighter ions will have greater oscillations and collide with the rods while heavy ions will stay oscillating along the length of the rods. By applying a positive direct current (DC) potential on the same rods it is possible to tune the maximum mass allowed through the quadrupole, effectively making a tunable high-mass pass filter. The other pair of rods will also have a RF potential, but combined with a negative DC potential. Heavy ions will feel an average of the signal and be attracted towards the rods and neutralize. However, light ions will quickly deflect while the rods are positive and thereby oscillate along the length of the rods, effectively constituting a tunable low-mass pass filter. By combining all four rods it is possible to make the ions follow a spiral trajectory that works as a mass filter with a resolution of less than $m/z = 1$, effectively letting through a single m/z value at a time [31].

The potential distribution of a QMS, ϕ, is given by [31–33]

$$\phi = (U + V\cos\omega t)\frac{x^2 - y^2}{r_0^2} \tag{2.11}$$

where U and V are DC and RF potentials on the rods, respectively, ω is the angular frequency of the RF potential, t is time, x and y are spatial coordinates orthogonal to the direction of the rods, and r_0 is the distance between the center axis and the rods. The RF potential on the two rod pairs are phase shifted by π. The resulting equations of motion are found as [31, 33]

$$\frac{d^2x}{dt^2} = -(U + V\cos\omega t)\frac{ex}{mr_0^2} \tag{2.12}$$

$$\frac{d^2y}{dt^2} = (U + V\cos\omega t)\frac{ey}{mr_0^2} \tag{2.13}$$

$$\frac{d^2z}{dt^2} = 0 \tag{2.14}$$

where m is the ion mass. Equation 2.12 and 2.13 can be rewritten to the form of Mathieu's differential equation [31]

$$\frac{d^2u}{d\xi^2} + (a + 2q\cos 2\xi)u = 0 \tag{2.15}$$

where

$$\xi = \frac{t}{2}, \tag{2.16}$$

$$a = \frac{4eU}{\omega^2 r_0^2 m}, \tag{2.17}$$

$$q = \frac{2eV}{\omega^2 r_0^2 m}, \tag{2.18}$$

and u is either x or y. The bound solutions to equation 2.15 are shown as a grey field in figure 2.14 as function of a and q. This area indicates the region where the ions are stable. In principle a and q can be varied independently, but usually they are kept at a constant ratio. This yields the mass scan line, also shown in figure 2.14. If the mass scan line only intersects with the tip of the stable region only ions with a certain mass will be stable in the quadrupole. By changing U and V with the same factor different ion masses will fall within the stable region, effectively making a mass filter.

Ion source

Ionization of molecules on the filament is dependent on the ionization cross section, meaning the probability of ionization [34]. The high energy electrons from the filament can also break molecules into smaller ions that will have other m/z ratios. Additionally, naturally occurring isotopes will also show on a mass spectrum. This is both a blessing and a curse since bigger molecules will have complex spectra that overlap with other spectra from other gases. However, it also allows distinction between molecules

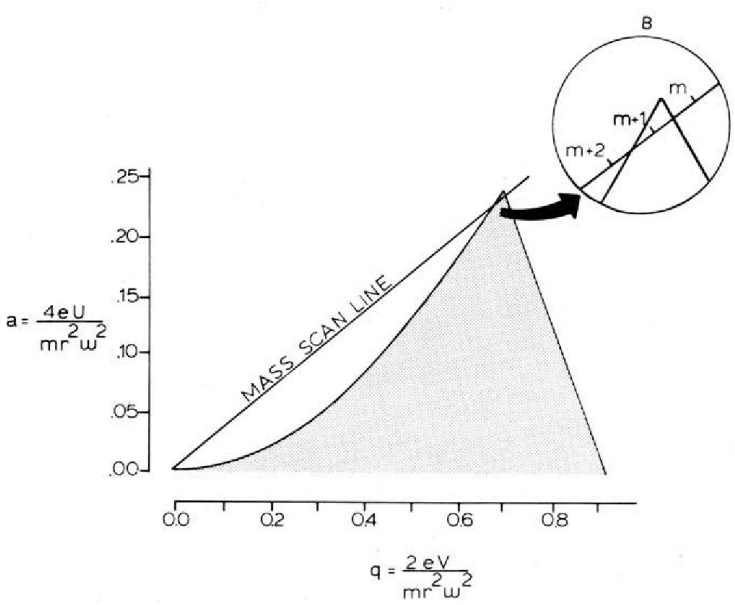

Figure 2.14. Stability diagram of a QMS. The grey area indicate the stable region of the ions. By having a constant ratio between a and q a mass scan line that intersects the tip of the stable region appears. U and V can be varied with the same factor to vary the mass that enters the stable region. Reprinted from [31], after [33].

with the same primary mass. Lastly, the gases can react with carbon or oxygen on the filament forming CO, CO_2, H_2O, and other species.

Ion detection

After mass selection by the rods the ions are detected using a secondary electron multiplier. Several metal plates are charged and incoming ions will hit a plate and kick out electrons. These electrons will hit another charged plate and a cascade effect amplifies the signal. The resulting measured current is proportional to the concentration of the gas present at the filament, but is not a direct measure of the gas. This is important to note during quantitative analysis of the data.

2.2.2 XPS

X-ray photoelectron spectroscopy (XPS) is a surface sensitive technique that relies on the photoelectric effect, of which Einstein received the Nobel Prize in Physics in 1921 [35, 36].

Photoelectric effect

It utilizes X-rays to kick an electron out from an atom. The electron energy is detected by a hemi-spherical analyser (HSA) and the energy spectrum can uniquely identify compounds and chemical environments of a sample surface. The energies of the resulting electrons follow the relation [3]:

$$E_{\text{kin}} = hf - E_{\text{bin}} - \varphi \tag{2.19}$$

where E_{kin} is the kinetic energy of the electron, h is the Planck constant, f is the frequency of the X-ray, E_{bin} is the binding energy of the electron, and φ is the work function of the hemispherical analyser.

X-ray source

The photons are generated in an X-ray gun. Electrons from a filament bombard an anode that leaves an electron hole at the 1s level. Relaxation of electrons from the $2p_{1/2}$ and $2p_{3/2}$ to the 1s orbital will emit a $K_{\alpha_{1,2}}$ X-ray [37]. Usually magnesium or aluminum is used for the anode, giving well defined radiation at 1253.6 eV and 1486.3 eV, respectively. Since the magnesium main peak has a full width at half maximum (FWHM) of 0.7 eV and the spectral lines of the sample binding energy also have a broadening, the peaks arising from K_{α_1} and K_{α_2} will often overlap. Due to double ionisation, the two anodes will also have smaller displacement lines at higher photon energies known as satellites [38]. Unless the X-ray source has a monochromator, all spectral lines will show small satellite peaks at higher binding energy. For the magnesium anode, the most dominant are the K_{α_3} and K_{α_4} shifted 8.4 eV and 10.2 eV relative to the main peak [39]. Cross

contamination from the two anodes or other impurities can result in ghost peaks in the X-ray spectrum. In the case of contamination from aluminum on the magnesium anode, the ghost peak will be shifted 233 eV relative to the main peak [39]. However, if the anode is clean, this can usually be avoided.

Electron detection

Detection of the electron energy is done by a HSA, shown schematically in figure 2.15. Two concentric hemispheres have an electric potential difference. Electrons entering one end of the detector will be bent according to the electric fields while an aperture permits electrons with a narrow energy distribution to hit a detector in the other end of the analyzer. By varying the electric fields a broad spectrum of energies can be detected. By changing poles on the hemispheres the detector can also be used to detect ion energies used in ISS [40]. The work function, φ, is the energy required to remove an electron from the Fermi level to the vacuum state [3]. The HSA has its own work function that must be corrected for in the data treatment of the kinetic energy to find the binding energy using equation 2.19.

Electron mean free path

X-rays penetrates deep into the substrate sample, but XPS is a surface sensitive technique because of the mean free path of electrons in a solid, plotted as a function of electron energy in figure 2.16. For a large number of elements the electron mean free path follows the same curve, with a minimum depth at 40 eV to 100 eV of $\sim$5 Å. This means that XPS is very surface sensitive, but does have a finite probing depth, usually of 1 nm to 2 nm.

The electron intensity decays with penetration depth as [42]

$$I = I_0 \exp\left(-\frac{x}{\lambda}\right) \tag{2.20}$$

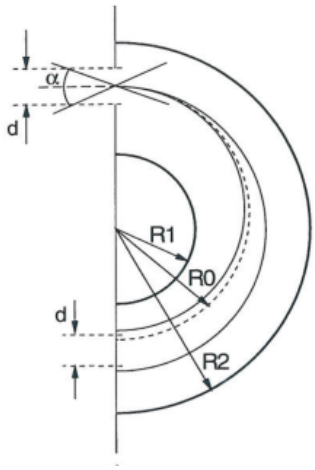

Figure 2.15. Two concentric hemispheres form the hemispherical analyzer. The sensitivity and resolution of the analyzer is given by the geometrical parameters and the electric fields of the two hemispheres. Reprinted from [37].

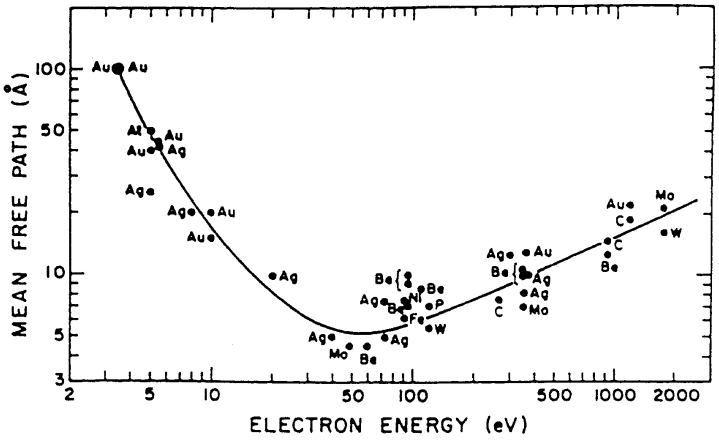

Figure 2.16. The electron mean free path in solids as function of electron energy, also known as the universal curve. Reprinted from [41], after [42].

where I is the electron intensity out of the sample, I_0 is the initial electron intensity, x is the probing depth, and λ is the electron mean free path. This shows that even a single monolayer (ML) will have an impact on signal intensity, but the actual probing depth is several monolayers deep.

Peak analysis

Prior to all peak analysis, a Shirley background is subtracted from the spectra. The background is calculated by the equations [43]

$$I''(E_{\text{bin}}) = I'(E_{\text{bin}}) - I''(E_{\text{bin},0}) \left(\frac{\sum_{E'_{\text{bin}} > E_{\text{bin}}} I'(E'_{\text{bin}})}{\sum_{E'_{\text{bin}} > E_{\text{bin},0}} I'(E'_{\text{bin}})} \right), \quad (2.21)$$

$$I'(E_{\text{bin}}) = I(E_{\text{bin}}) - I_{\text{B}} \quad (2.22)$$

where $I(E_{\text{bin}})$ is the signal intensity as a function of binding energy, I_{B} is a constant background defined as the lowest intensity measured, $I'(E_{\text{bin}})$ is the signal corrected for a constant background, $I''(E_{\text{bin}})$ is the final background corrected spectrum, and $E_{\text{bin},0}$ is the binding energy at the low energy foot of the peak. Since I'' occurs on both sides of the equation the background subtraction is an iterative process. This is usually done by dedicated software.

2.2.3 ISS

Ion scattering spectroscopy (ISS), also known as low-energy ion scattering (LEIS), is a technique for measuring and quantifying the outermost atomic surface layer of a sample. When used with a low ion beam current the technique is practically non-destructive [44].

The working principle of ISS is to accelerate an ion towards a sample surface. If the ion is not neutralized it will be elastically scattered by the outermost surface atom of the sample and be deflected. The ion energy loss is determined by [44]

$$E_{\text{f}} = E_{\text{i}} \frac{\cos\theta \pm \sqrt{r^2 - \sin^2\theta}}{1 + r} \quad (2.23)$$

where E_{i} is the initial ion energy, E_{f} is the final ion energy, θ is the scattering angle, r is the surface atom mass to ion mass ratio. The positive

sign applies when $r \geq 1$ and both signs are solutions when $1 \geq r \geq |\sin\theta|$. This equation allows one to calculate the mass of sample surface atoms. As mentioned, the technique benefits from a high surface sensitivity, but is limited in distinguishing masses close to each other since the resulting peaks will overlap.
Helium ions are usually used because they are light and inert. Helium is let into a UHV chamber and ionised by a filament. The ions are then accelerated by charged lenses towards the surface with a specific energy. The energy of the scattered ions is detected by a hemi-spherical analyzer as described in section 2.2.2.

2.2.4 SEM

The scanning electron microscope (SEM) is used for imaging samples details below the magnification of conventional optical microscopes. To probe a sample it uses an electron beam with electron energy of 2 to 1000 keV resulting in wavelengths of 0.027 to 0.0009 nm. Unfortunately the resolution is not that small, but limited of the interaction volume of the sample. When an electron beam hits a sample several process occur that can be utilized to characterise the sample. This is schematically shown in figure 2.17. The most common signals for imaging are secondary and backscattered electrons. For the purpose of this thesis, only backscattered electrons where used.
The incident electron will be scattered by the sample atoms upon interaction. A fraction of theses electrons will be scattered at an angle greater than $\pi/2$ and leave the surface again before being absorbed. These electrons can be measured with a detector placed close to the incident beam. The fraction of backscattered electrons will depend on the mean atomic weight of the local part of the sample being probed. Higher atomic number result in more backscattering. This allows for compositional analysis of the sample which is highly useful for imaging nano particles on μ-reactors [45]. All SEM images where done by Elisabetta Maria Fiordaliso.

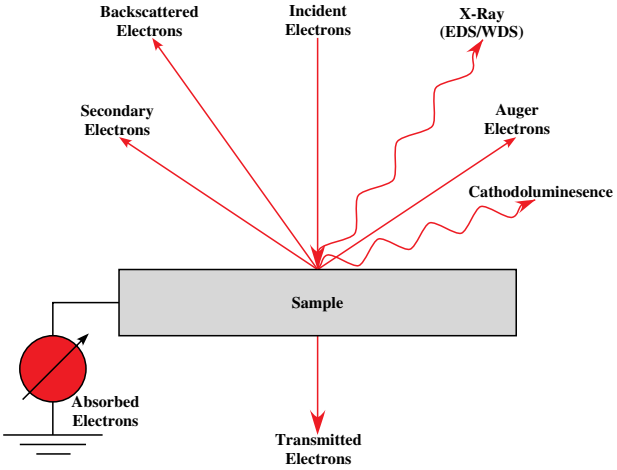

Figure 2.17. Signal generation from electron beam on a sample. Secondary and backscattered electrons are most common for imaging. Reprinted from [45].

2.3 Chemical kinetics

The rate of chemical reactions are often temperature dependent. Experimental findings follow an exponential correlation expressed as the Arrhenius equation [46]:

$$k = A \exp -\frac{E_{\text{act}}}{k_{\text{B}} T} \tag{2.24}$$

where k is the reaction rate, A is the pre-exponential factor, and E_{act} is the activation energy. E_{act} is a measure of the temperature dependence of the reaction while A is the theoretical rate at infinite temperature, sometimes referred to as the frequency factor. A re-writing of the same equation yields:

$$\ln k = \ln A - \frac{1}{T} \frac{E_{\text{act}}}{k_{\text{B}}} \tag{2.25}$$

where the reaction rate can be plotted as a straight line when the x-axis is $1/T$ and the y-axis is logarithmic. Here E_{act} defines the slope and A is the intercept with the y-axis. Some reactions have non-Arrhenius behaviour

where the slope varies with temperature. However, this still allows a temperature dependent activation energy to be extracted from the slope of the curve.
By transition state theory the pre-exponential factor, A, can be interpreted as the vibrational frequency of a reactant in a 3-dimensional potential landscape. The exponential factor is therefore interpreted as the fraction of reactants in the transition state with a high enough kinetic energy to facilitate a reaction, given by a Boltzmann distribution, $\exp -E_{\mathrm{act}}/k_{\mathrm{B}}T$.

2.4 Cluster sources

Results presented in this thesis include experimental testing and characterization on clusters and nano-particles from several cluster sources. Two different sources where used at different sites, i.e. DTU and TUM.

2.4.1 Omicron

This cluster source is located at CINF, DTU and is often referred to Omicron because of the analysis chamber attached to it. On a daily basis the set-up is operated by Béla Sebök, with my occasional assistance.
A schematic drawing of the cluster source is seen in figure 2.18. Nano-particles are produced by sputtering a metal target and mass filtering the resulting particle in the gas phase. Ar or He is let into magnetron head. Here it is ionized by the target which is kept at negative potential of $\sim$200 V. A combination of electric field and an array of magnets direct the Ar^+ plasma onto the metal target to produce a metal vapour [14]. This material is then cooled in the sputter-aggregation chamber where it condensates to clusters and nano-particles. By differential pumping and electrical lenses the charged particles are then directed into a lateral time of flight mass filter.
A schematic drawing of the time of flight principle is shown in figure 2.19. The particles are accelerated upwards by an electric field created between

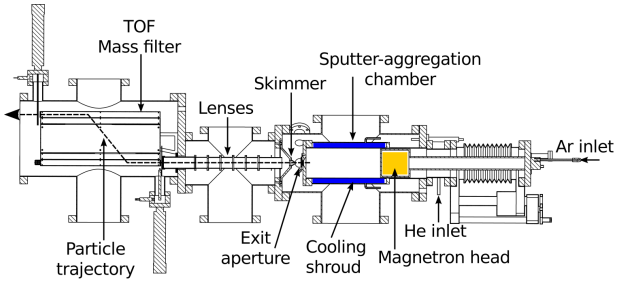

Figure 2.18. The Omicron cluster source located at CINF, DTU. Note that the TOF in the figure denotes a time of flight mass filter and has nothing to do with turnover frequency. Reprinted from [47].

plate 1 and 2, and after a certain time interval, are decelerated again by a field in the opposite direction. This results in a particle separation in m/z ratio. The lightest particles will accelerate faster with the first electric field, ending at the top part of the chamber, while heavy particles will not travel as far, ending at the lower part of the chamber. The position of a narrow exit slit is responsible for selecting particles of a particular mass to charge ratio [15].

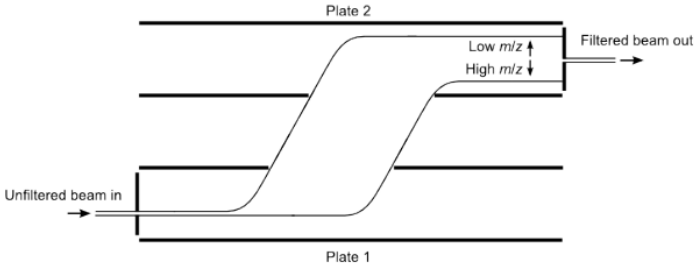

Figure 2.19. Working principle of a time of flight mass filter. Figure by Anders Bodin.

2.4.2 Laser ablation cluster source

The cluster source located at the Chair of Physical Chemistry at the Technische Universität München is shown schematically in figure 2.20 [16, 17, 48]. The figure shows the entire UHV chamber, divided into three main sections; the cluster source, sample preparation chamber, and an

analysis chamber. Only the cluster source and preparation chamber where used during the work of this thesis. The cluster formation is done in the cluster source by shooting a 532 nm Nd:YAG laser pulsed at 100 Hz at a rotating platinum target. The resulting plasma is cooled with a delayed helium pulse that expands into the chamber. It is in this process clusters are formed with a broad size distribution, some of them being ionized. The differentially pumped system guides the thermalized cluster into an octupole that guides the cluster beam into a set of ion optics that focuses the beam. To bend the cluster beam 90° a quadrupole deflector is used. An added benefit of this is to separate neutral clusters from the ionized ones. A QMS then mass selects the clusters before deposition on the sample. An aperture of 10 cm was placed in front of the µ-reactor to limit cluster deposition onto the reactor volume [49].

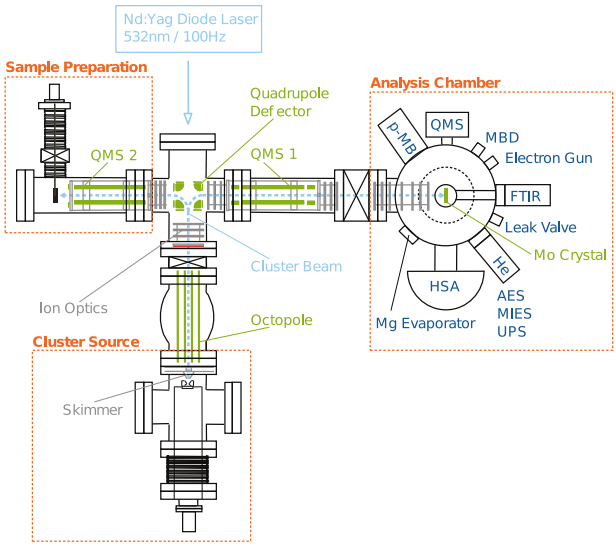

Figure 2.20. Experimental set-up at TUM, including the cluster source, sample preparation chamber, and analytical chamber. Only the first two parts where used in this thesis. Reprinted from [48] after [16].

The cluster deposition is measure using an ammeter on the µ-reactor. To ensure the clusters do not destroy on impact with the sample, a retarding field analysis ensures that the kinetic energy of the clusters is $<1\,\mathrm{eV/atom}$.

This is done by gradually applying an electric potential on the sample. When the cluster current goes to zero it means that the clusters do not have enough kinetic energy to overcome the potential barrier. For Pt_8 clusters the potential sould be <8 V below this point to ensure soft landing conditions [50, 51].

A highly import attribute of this cluster source is the ability to produce mono-disperse clusters. To prove the mono-disperse nature of the clusters, a mass scan of the QMS was done prior to deposition, seen in figure 2.21. A clear separation of the cluster masses proves the clusters are indeed mono-disperse when deposited [49].

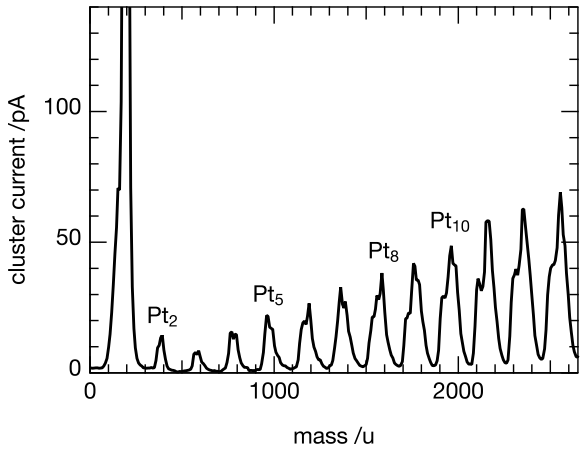

Figure 2.21. Mass scan of Pt cluster deposition. The clear separation of peaks proves that deposited clusters are indeed mono-disperse. Reprinted from [49].

Chapter 3

H_2/D_2 exchange: The simplest reaction we could think of

This project was started in early summer 2013. Marian Rötzer was doing his master thesis [52] at CINF as an exchange student from TUM. The experiments were intended as a quick side project of his master thesis before other systems and reactions would be studied. After initial experiments done by Marian, I intended to finalize the experiments for publication. The project has since been named The Never Ending Story, but three years after the initial experiments began, a paper was submitted on the basis of this project.

3.1 Introduction

Optimization of catalysts is important for industrial use, as gaining even a minor increase in its effectiveness or lifetime can greatly increase the overall yield over the lifetime of the catalyst. Having a fundamental understanding of the materials composing the catalyst is of prime importance, and new knowledge of systems already in use can lead to these advances. One of the most challenging parts of fundamental studies is to isolate the different effects influencing the system. For this reason, a model system is an ideal basis to conduct experiments, where most parameters can be kept constant, while a specific parameter is deliberately varied. Catalysts with cluster sizes

down to a single atom and with a tunable mono-disperse size distribution is therefore ideal as a bottom-up design of model catalysts for fundamental studies.

Size selected clusters have shown interesting physical and chemical properties that change with size [53–58], shape [59], and support [49, 60, 61]. For example; bulk gold is noble and does not dissociate H_2 [62], but gold clusters have a unique ability to do this both catalytically [56] and photocatalytically [63].

3.1.1 Hydrogen dissociation

Dissociating hydrogen is an important elementary step in numerous catalytic reactions. One of the largest industrial reactions is the formation of ammonia, i.e. $N_2 + 3\,H_2 \longrightarrow 2\,NH_3$ [64] that require dissociation of three hydrogen molecules to make two ammonia. In an attempt to construct a sustainable transportable engine, the simple reaction of hydrogen oxidation, i.e. $2\,H_2 + O_2 \longrightarrow 2\,H_2O$, is being widely studied for fuel cells [65–67], and hydrogen storage in metal hydrides also requires dissociation of hydrogen [68–72]. Despite this fact, the reaction is still scarcely understood on metal clusters at ambient pressures.

Early studies of hydrogen dissociation was done on single crystals. It was found that platinum crystals with a high Miller index are more likely to dissociate hydrogen [73–75]. This would suggest that smaller nano particles are preferable since they have many kinks and corners and only small extended surfaces. It was also through single crystal studies that adsorption-dissociation was found to be rate controlling for H_2/D_2 exchange reactions [76, 77]. A study on the Pt(111) surface finds that repulsive adsorbate interaction results in a weaker hydrogen binding to the surface and desorption activation energy also decreases with increasing hydrogen coverage [78].

3.1.2 Particle size effects on hydrogen dissociation

Despite the Miller index dependency on single crystals, hydrogen splitting on platinum nano particles of 2 to 5 nm is only weakly dependent on size [79]. There will be OH formation on the nano particle or at the interface with a SiO_2 support [80]. This will be evident by scalability of the reaction rate with the projected circumference of the particle, since the OH group is found to be directly involved in the reaction [81]. On small Pt_{13} clusters it is found that one cluster can accommodate 32 hydrogen atoms at a pressure of 200 mbar [82]. This shows that each platinum atom can bind more than one hydrogen atom. For the sake of the H_2/D_2 exchange reaction this is required to get sufficient hydrogen and deuterium atoms on the surface. If the adsorbates are also capable of scrambling on the surface the HD formation will be larger.

3.2 Sample treatment and preparation

3.2.1 Cluster deposition

The cluster samples used for this study were prepared at a cluster source located at the Technische Universität München, Germany. Details on the cluster source are described in section 2.4.2. Clusters were deposited under soft landing conditions, i.e. cluster energies below 1 eV per atom to prevent the clusters from destruction upon impact [50, 51]. A cluster coverage of $0.023\,\mathrm{nm}^{-2}$ was deposited in the reaction chamber of 10 mm diameter. This means that the total number of clusters stay constant for all samples, but samples with bigger clusters result in more platinum deposited in the reactor. For the Pt_8 sample this corresponds to 4.7 ng of platinum. The $Pt_{\geq 8}$ sample contains the same amount of clusters, but considerably more platinum. The exact amount is impossible to know since the clusters are unselected and the size distribution is therefore unknown.

3.2.2 Catalytic activity

Experiments aimed to demonstrate the effects of O_2 were carried out with a mix of gas flows and temperature treatment as seen in figure 3.1. The entire treatment was repeated multiple times to demonstrate reproducibility and eliminate effects of contaminants being reacted off at the start. At $\sim$0 h an O_2 gas flow is started and the temperature is increased to 150 °C at 1 bar to react off any contaminants. The reactor was pumped out and flushed twice with Ar at 0.5 bar to clean the gas lines from residual O_2. A gas stream of H_2/D_2/Ar is started at 4 mL min^{-1}, 4 mL min^{-1}, and 1.5 mL min^{-1}, respectively, while the pressure is kept at 1 bar. The Ar flow is divided onto two MFCs. This is done to keep a gas flow on both inlet channels to avoid gases standing still in one gas line during reaction. For 4 h the temperature is kept at 100 °C to react off contaminants on the surface, including oxygen. After cooling to RT, three consecutive heating ramps to 180 °C with 2 °C min^{-1} test the reactivity of the catalyst. At $\sim$20 h the temperature is again kept at 100 °C for 4 h and at $\sim$24 h a 0.5 mL min^{-1} flow of 5000 ppm O_2 in Ar is started and kept steady for another 4 h. This gas flow results in a 26 ppm O_2 contamination in the H_2/D_2 gas mixture. The sample is then cooled to RT and three heating ramps to 120 °C to measure chemical activity with O_2 contamination. The temperature is then increased to 100 °C for 4 h and the sample is then cooled to RT and pumped down. The entire process is then repeated.

The sample treatment described above is an alteration of the procedures used by Marian Rötzer to study size effects. The original did not include the Ar flushing, pre-treatment at 100 °C in a H_2/D_2 gas mixture, and all experiments involving diluted O_2 in Ar are treatments added at a later state.

All presented measured TOFs have been calculated from the QMS signals. HD has the main peak at $m/z = 3$, but when H_2 and D_2 are being dosed in the UHV chamber, a background signal arises from reaction on the filament. This lead us to believe that the $m/z = 3$ background signal is proportional

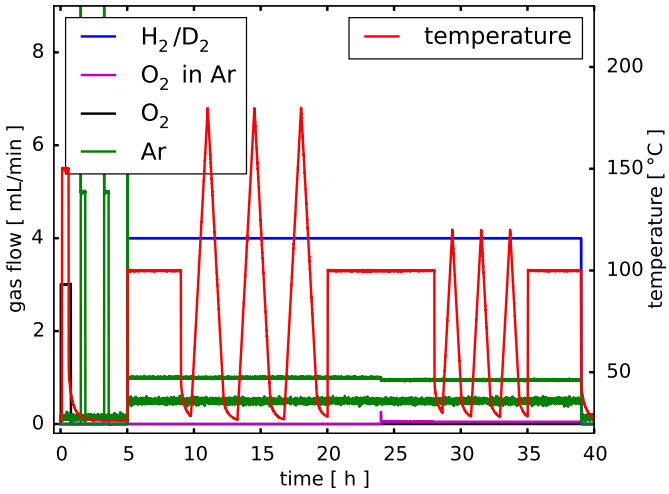

Figure 3.1. Treatment of platinum samples for H_2/D_2 exchange reaction. Gas flow values are shown on the left axis and sample temperature is on the right.

to the $m/z = 4$ signal, which is only influenced by D_2. However, at higher temperatures, where D_2 is being consumed, the background level will be smaller. Therefore, a background proportional to the $m/z = 4$ signal was subtracted. To calculate a TOF the total number of surface sites is needed together with the amount of HD molecules leaving the reactor. Surface sites are easily estimated by the number of clusters in the reactor and assuming that all atoms constitute surface atoms. The HD production was estimated by assuming that 4:9.5 of the gases leaving the reactor at full conversion is HD. Using equation 2.6 the gas flow can be calculated and related to the $m/z = 3$ signal.

3.2.3 Characterisation

ISS and XPS characterisation was performed in a UHV chamber from Omicron. The chamber has a base pressure of 1×10^{-11} mbar and ISS was performed with a helium pressure of 1×10^{-7} mbar. He^+ were accelerated to 1 keV and detected with a hemi-spherical analyzer. For XPS a magnesium

anode with a FWHM of 0.7 eV was used without a monochromator. Further details are shown in table A.1 of appendix A.

3.3 Size effects

The initial ambition was to study size effects on the H_2/D_2 exchange reaction on platinum clusters, ranging from 1 to 68 atoms. In figure 3.2 the results of the master thesis by Marian Rötzer are beautifully summarized [52]. The most active clusters show data down to ∼0 °C because they showed a finite activity at RT. To accommodate this, the samples were actively cooled using a water-cooled copper block and a Peltier element in a sandwich structure on top of the μ-reactor. Clusters smaller than seven atoms did not show any detectable activity and are omitted from the graph.
A clear tendency reveals itself, with bigger clusters being more active. The reason for this apparent tendency is only speculative, but could be related to larger surfaces simply allowing more reactants and better scrambling to occur. Though bigger clusters tend to be more reactive, common sense dictates that there should be a naturally occurring maximum which was not found in this study. The obvious choice would be to test nano-particles, but the project encountered other obstacles before this was mapped out.
In the data set shown in figure 3.2 only one cluster size is reproduced, i.e. Pt_7. The two samples differ by roughly a factor of two in reactivity, which seems significant, but is a small change compared to the other cluster sizes. Naturally, the results for each size needed to be reproduced in order to be conclusive. To our great regret this proved harder than expected.

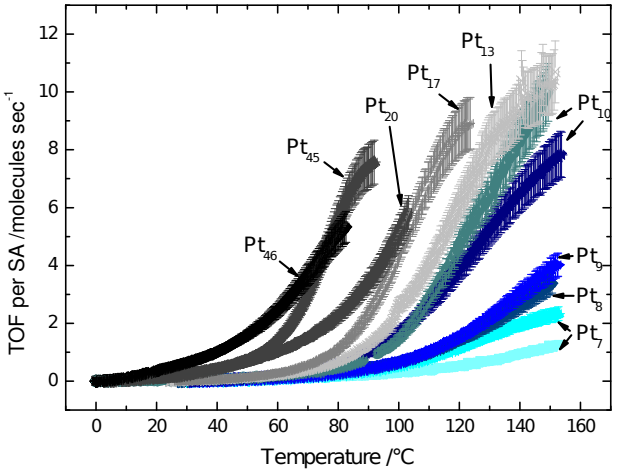

Figure 3.2. Initial size effects of H_2/D_2 exchange on Pt clusters. Plot shows TOF per surface atom. Results from clusters smaller than seven atoms are omitted because they showed no detectable activity. The preliminary results from Marian Rötzer were promising. To our disappointment the results proved hard to reproduce. Reprinted from [52].

3.4 Influence of O_2 of H_2/D_2-exchange

The following catalytic data was obtained by me. To finalize the project of size effects of H_2/D_2-exchange on platinum clusters, several new samples were measured to demonstrate reproducibility. Figure 3.3 shows the first attempts at this. Each sample was measured in a suitable temperature regime and TOF was found at 120 °C by fitting to the Arrhenius equation and extrapolating. Especially the upper left corner of the graph shows great variation within a single cluster size when considering the y-axis is logarithmic. TOF varies more than one order of magnitude for the Pt_{12} samples, indicating a huge source of error.

Through a long process of trial and error, I noticed that the activity of a given temperature ramp would change with the time the H_2/D_2 gas flow was on stream. For this reason a simple experiment was made where the temperature was kept constant and the activity was monitored over several hours, as seen in figure 3.4. Prior to each curve on the graph the sample

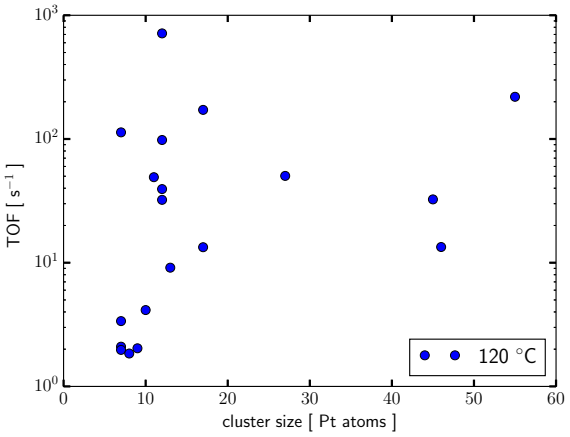

Figure 3.3. In an attempt to reproduce the results in figure 3.2 new samples were measured. H_2/D_2-exchange TOF is shown at 120 °C for different clusters sizes. A large variation is seen, especially for measurements on four Pt_{12} samples that vary more than one order of magnitude.

was oxidized at 100 °C for 2 h. During pressure build up in the reactor, HD signal increased as expected. However, before the reactor pressure reached 1 bar the HD signal decreases at ∼50 min to a level with only slight increase in activity for ∼1 h. At ∼110 min the HD signal increases with almost one order of magnitude and then gradually decrease over several hours to a semi-stable plateau at ∼380 min. Several samples and sample sizes showed a similar effect, and it is safe to say that this puzzled us a great deal and is a major reason why the project took so long.

By chance, the cause of changing activity was found by altering the gas flows while interrupting an experiment. To understand the cause of the error one must examine the schematic drawing of the gas handling of the μ-reactor set-up. The H_2 and D_2 gas lines both use the same inlet on the μ-reactor. This means that the second gas line is not used during H_2/D_2 exchange, but it is used during oxidation prior to each reaction. It was found that residual O_2 in the second gas line slowly leaks into the gas stream by diffusion and the O_2 contaminations would vary slowly over time

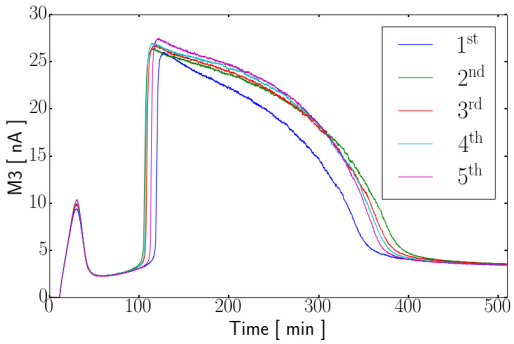

Figure 3.4. Varying activity for H_2/D_2-exchange over several hours on a Pt_9 sample at 80 °C. The same experiment is repeated five times with extraordinary reproducibility.

during experiments. This contamination source was later found to cause the remarkable change in cluster activity.

3.4.1 Controlled oxygen dosage

To investigate the effect in a controlled manner, some changes were made to the set-up, described in more detail in section 2.1. In short, two gas lines were added, one on each inlet, and the MFCs were exchanged with newer digital ones than allow better control of the flow. The added gas lines allowed argon flushing of the gas lines between experiments and a small amount of argon to be dosed through the spare inlet during reaction. Additionally, a bottle containing 5000 ppm O_2 in Ar was added to allow small amounts of O_2 to be dosed in controlled amounts during experiments. The resulting data concludes that minute amounts of O_2 facilitate the H_2/D_2-exchange reaction dramatically, as drawn schematically in figure 3.5. Using a Pt_8 sample as a reference system, H_2/D_2-exchange was measured with and without O_2 in the revised experimental set-up. The activity plots are shown in figure 3.6 as function of temperature in figure 3.6 a). The three red curves show consecutive heating ramps to 180 °C in a pure $H_2/D_2/Ar$ gas stream, with arrows indicating the direction of the heating ramp. All

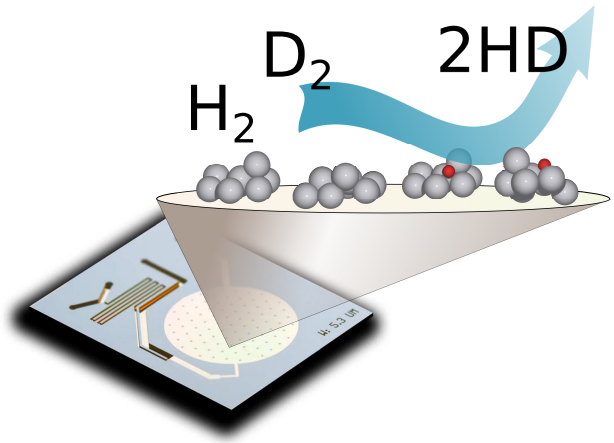

Figure 3.5. Schematic drawing of H_2/D_2-exchange being facilitated on the oxidized clusters. Reprinted from [49].

three curves lie closely on top of each other, proving the inherent robustness of the μ-reactor platform and the stability of the catalyst. A small hysteresis is seen in the system. There are many possible explanations for this, but an educated guess would be an actual temperature difference in the reactor of ∼5 °C. Two green curves show similar heating ramps to 120 °C with 26 ppm O_2 added to the gas stream. The activity is significantly higher during O_2 dosage and full conversion is reached ∼70 °C lower temperature. Again, the arrows indicate the direction of the temperature ramp, and a dramatic hysteresis is apparent where the catalyst is kept at full conversion during cooling to ∼45 °C. Since the reaction is equally likely to run backwards and forwards and with only one reaction intermediate, the hysteresis can not be explained by reactants blocking the surface as is known for CO oxidation [83–85]. Instead the O_2 must change the platinum cluster or be part of a reaction intermediate. The grey bar indicating full conversion has a downwards slope. This is caused by the decreasing gas flow through the narrow capillary with increasing temperature, described in section 2.1.5.

Figure 3.6 b) shows the same activity data as an Arrhenius plot. A dashed line shows an Arrhenius fit to the first part of the ramp with increasing

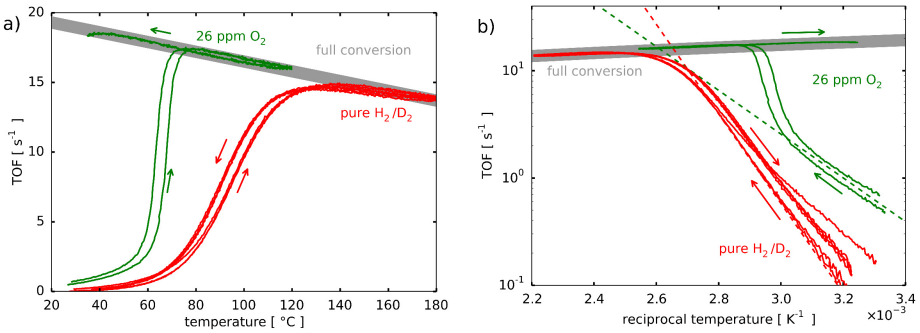

Figure 3.6. HD TOF at varying temperature on a Pt_8 sample with (green) and without (red) 26 ppm O_2 added to the gas stream. Arrows point in the direction of the temperature ramp and the grey bar indicates area of full conversion. Figure a) shows TOF as function of temperature. A pure H_2/D_2 gas mixture shows a clear temperature dependence with very little hysteresis. Adding O_2 dramatically increases the TOF in the entire temperature range. A substantial hysteresis keeps the activity at full conversion during cooling to ∼45 °C. Figure b) shows the same data in an Arrhenius plot. Dashed lines show a fit to the low TOF part of the heating ramp. The resulting fitted parameters are shown in table 3.1. Reprinted from [49].

temperature. Resulting activation energies and pre-exponential factors are seen in table 3.1. The apparent activation energy is roughly cut in half when O_2 is added to the gas stream. The pre-exponential factor is also changed. It is clear that the green curve follows a non-Arrhenius behaviour and increases in activity at a certain point. This might be oxygen that is dissociated on the surface and changes the chemical properties of the cluster.

Table 3.1: Apparent activation energies and pre-exponential factors for H_2/D_2-exchange on a Pt_8 sample with and without oxygen dosage. Data from [49].

gas dosage	E_{act} [eV]	A [s^{-1}]
pure H_2/D_2	0.83	28.3
26 ppm O_2	0.40	15.0

3.4.2 Thoughts on oxygen-assisted hydrogen dissociation

The activation energy and adsorption energy of H_2 dissociation on different platinum surfaces has been found in several studies, both by experimental and density functional theory (DFT) techniques. A representation of values found in literature are shown in table 3.2, with results from this study listed as systems named Pt_8/SiO_2, Pt_8O_x/SiO_2, and Pt_8O/SiO_2. By a quick glance it is clear that values vary significantly, both with varying system and varying method. The presented results prove that small amounts of O_2 can change the apparent properties of the system substantially, and might explain the low activation energies obtained in literature. Computer simulation are inherently clean and would never have gas impurities that are not put there deliberately, but the dosed amount of oxygen are likely lower than the detection limit of most experimental set-ups. This is an extremely important point of the discoveries made with these clusters, that minute gas contaminants can alter chemical properties significantly.
The effects of O_2 on platinum clusters are also made clear in figure 3.7. A flow of H_2, D_2, and Ar through the reactor is kept constant at 1 bar and 100 °C. The first 4 h show a stable activity, but the addition of 26 ppm O_2 increases the activity to a stable plateau of 100 % conversion. This dramatic increase further stresses the oxygen effects on the system. The experiment is repeated three times to demonstrate reproducibility.
So far the oxygen effects have been demonstrated on Pt_8 clusters, which constitutes a highly specific model system. However, similar experiments on an unselected $Pt_{\geq 8}$ sample reveal a more generalized effect that applies to a broad spectrum of cluster sizes. Figure 3.8 shows the activity of the $Pt_{\geq 8}$ catalyst with (green) and without (red) O_2 in the gas stream. The left figure shows the activity as function of temperature and the right figure shows the same data as an Arrhenius plot. The y-axis shows the HD ion signal i nA in stead of TOF as in figure 3.6 because the number of surface platinum atoms was not possible to derive. This is inherent in the detection of clusters, since the total number of clusters is known

Table 3.2: Activation and adsorption energies reported in literature on a selection of model systems. Both experimental values and simulated values are provided as stated. References are also provided. Adapted from [49].

system	E_{act} [eV]	E_{ads} [eV]	method	ref.
Pt(111)	$0.23 - 0.026^a$		exp.	[74]
Pt film	0.22		exp.	[70]
	$0.22 - 0.28^b$		exp.	[79]
Pt wire	0.11		exp.	[76]
2 nm Pt/SiO_2		0.93	exp.	[86]
Pt_8/SiO_2	0.83		exp.	[49]
Pt_8O_x/SiO_2	0.40		exp.	[49]
Pt(111)	$0.0 - 0.42^c$		DFT	[87]
	0.5		DFT	[88]
Pt(100)	0.8		DFT	[88]
	0.0		DFT	[89]
Pt_{22}/Al_2O_3		$0.42 - 0.62^d$	DFT	[90]
Pt_{44}/Al_2O_3		$0.47 - 0.61^d$	DFT	[90]
Pt_4/TiC(001)	1.16	0.87	DFT	[91]
Pt_8/SiO_2		$0.13 - 1.35$	DFT	[49]
Pt_8O/SiO_2		$0.066 - 0.89$	DFT	[49]

[a] Temperature dependent activation energy
[b] Varying with film thickness
[c] Dependent on adsorption site
[d] Energies vary with coverage

from measuring the cluster current during deposition, but the size of each cluster is unknown. Like the Pt_8 clusters, there is a clear difference between the oxidized clusters and the pure H_2/D_2 gas mixture. The red curves show an Arrhenius behaviour during gradual heating of the sample to the point where back reaction becomes significant. A clear hysteresis keeps the catalyst at almost full conversion during cooling, very unlike the behaviour of the Pt_8 catalyst. Remarkably, the O_2 dosage forces the catalyst to full conversion at all temperatures, from RT to 120 °C. This data suggests that the effects could be generalized and make it probable that oxygen

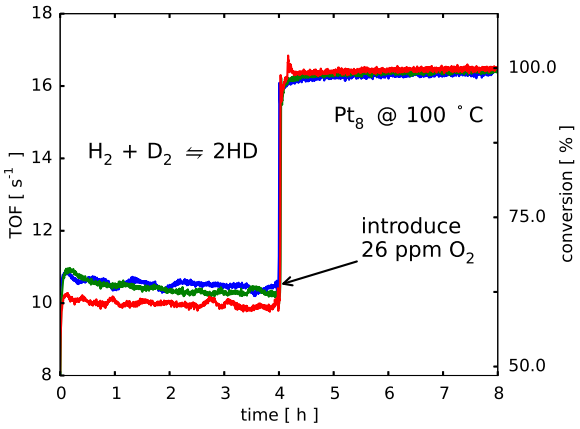

Figure 3.7. HD TOF at a constant temperature of 100 °C. After stable conversion for 4 h 26 ppm O_2 is introduced to the gas stream resulting in an increase in conversion rate from ∼60 % to 100 %. Reprinted from [49].

contaminants cause the great variation in literature values for activation energies of H_2 dissociation.

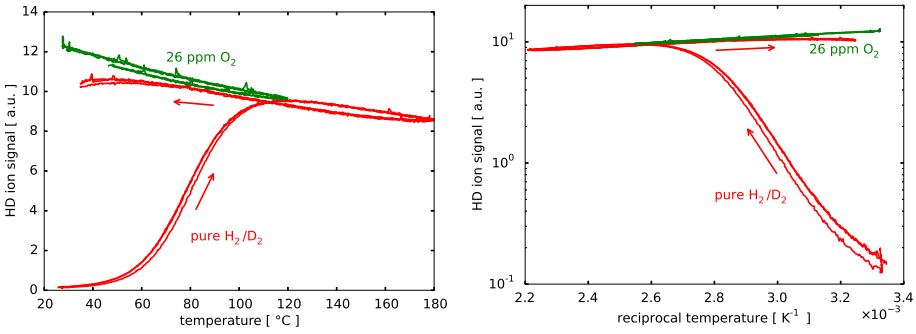

Figure 3.8. Left is shown the HD production as function of temperature on the $Pt_{\geq 8}$ sample. TOF is not possible to derive since the total catalyst surface area is unknown. On the right is shown an Arrhenius plot of the same data. Reprinted from [49].

Detection of reactants and side-products

During chemical testing of the Pt_8 sample H_2, D_2, and Ar was dosed continuously. The resulting m/z signals are shown in figure 3.9. H_2 and D_2 have resulting signals on $m/z = 2$ and 4 respectively while Ar has a main feature on $m/z = 40$ and a smaller signal on $m/z = 20$ from doubly ionized Ar. This result in a linear correlation between $m/z = 20$ and 40 that decreases with temperature because of the capillary flows temperature dependence. $m/z = 2$ and 4 decrease with temperature according to HD production in both graphs.

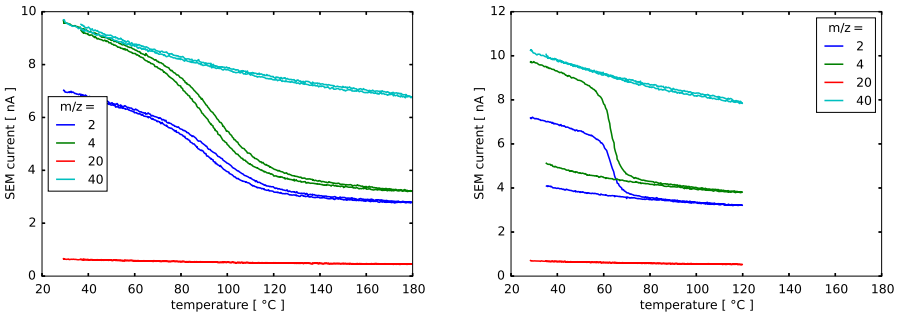

Figure 3.9. QMS signals from reactants during HD production with (right) and without (left) 26 ppm of O_2 in the gas stream. Reprinted from [49].

A number of side-products can be imagined during the reaction. Notably, O_2 ($m/z = 32$) and the formation of H_2O, HDO, and D_2O ($m/z = 18, 19, 20$) is to be expected [92]. These masses are shown in figure 3.10. The left figure shows by-product signals during pure H_2/D_2 dosage. All signals are very low, and several signals have a small negative off-set. The biggest signal is seen on $m/z = 18$. A constant background of water is expected, and the increasing signal is caused by H_2O evaporating from surfaces during heating. Remarkably, the $m/z = 32$ signal does not change between the two graphs, proving that the small amounts of O_2 are not detectable in the set-up at hand. The $m/z = 20$ signal is dominated by doubly ionized Ar and gives no information on D_2O formation. The $m/z = 19$ signal gives a slight increase at temperatures above ∼150 °C, only visible in the left figure.

This could come from OH groups on the SiO_2 being reacted of with H_2 and D_2. The increase in $^m/_z = 28$ and 44 signal could be a reaction between OH and carbon species to form CO and CO_2 at higher temperatures, but is most likely from leaking O-rings that let in small amounts of N_2 and CO_2 from the surroundings. This would also explain why the $^m/_z = 28$ signal is the biggest and increases the most. In conclusion, if H_2O, HDO, and D_2O are being formed during reaction it is below the detection limit of the set-up.

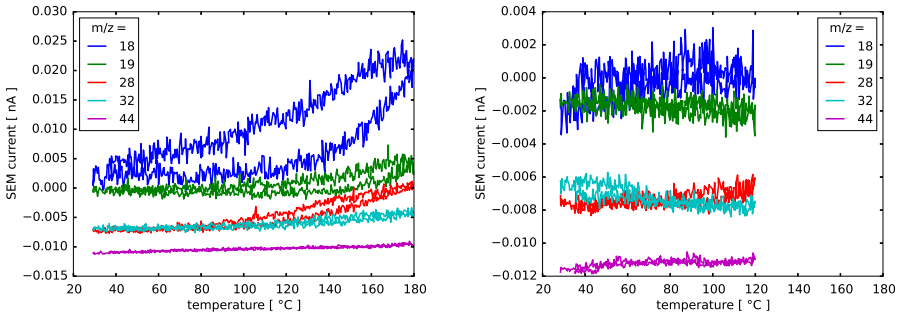

Figure 3.10. QMS signals from by-products during H_2/D_2 exchange on the P_8 sample with (right) and without (left) 26 ppm O_2 dosage. Reprinted from [49].

3.4.3 Spectroscopic characterisation

The presented chemical activities and dependency on contaminations are, to an extent, based on the catalyst remaining stable as Pt_8 clusters throughout experiments. If the catalyst sintered only slightly to larger clusters, the effects would still be the same, however, if it sintered to huge particles of several nanometres or micrometres, the conclusions would be meaningless. Several studies have been made that suggests that a narrow size distribution of the catalyst will suppress Ostwald ripening [48, 61, 93–96]. To prove that the catalyst is indeed stable during reaction the samples were characterized before and after chemical testing using ISS and XPS. Because a little sintering is difficult to detect on small clusters, the unselected $Pt_{\geq 8}$ sample

was used because it is more prone to sintering [48, 94–97]. If this sample is resistant to sintering, surely the mono-disperse Pt_8 sample will also be.

ISS characterization

The ISS technique is strictly surface sensitive. If a catalyst sinters, the surface area to volume ratio will decrease, resulting in a decreased ISS signal [44, 98, 99]. The ISS spectra in figure 3.11 are taken before (blue) and after (green) chemical reaction of the $Pt_{\geq 8}$ sample. Both curves have been normalized to the oxygen peak which is also the biggest. The platinum catalyst is clearly visible at ∼927 eV and the silicon and oxygen peaks from the support are seen at ∼590 eV and ∼391 eV, respectively. These three peaks barely change from one spectrum to the other, indicating little or no sintering. The broad features below ∼380 eV come from different carbon species, likely from contaminants from air during transportation between vacuum chambers. Two small features at 800 eV to 900 eV could not be identified, but the resulting masses of the bigger peak correspond roughly to barium while the smaller peak could originate from gallium or germanium. These compounds could come from residuals from the clean room fabrication process. However, they are so small they are considered negligible. To avoid these minor contaminations in future depositions, the reactors were cleaned with ethanol and sputtered with argon.
For comparison an ISS spectrum of the Pt_8 sample after reaction is seen in figure A.1 of appendix A. Most features are similar to those seen in figure 3.11, except for the platinum peak at ∼927 eV which is significantly smaller. This is to be expected since the two samples have the same number of clusters, but the clusters on the $Pt_{\geq 8}$ sample are significantly bigger.

XPS characterization

Using the same principle as ISS to determine catalyst sintering, XPS will detect a smaller signal if the metal clusters sinters. XPS spectra in figure 3.12 show the same $Pt_{\geq 8}$ sample before (blue) and after (green) chemical

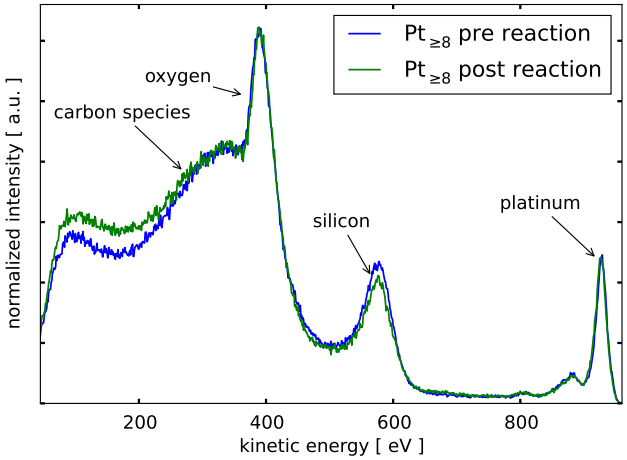

Figure 3.11. ISS spectra of the unselected $Pt_{\geq 8}$ sample before (blue) and after (green) reaction. The signals are normalized to the O_2 peak at ∼391 eV. At ∼927 eV the platinum peaks are almost identical, indicating little or no sintering of the catalyst. Reprinted from [49].

testing. The figure shows a detailed scan of the SiO_2 2p satellite peaks and the Pt 4f doublets. The red bars indicate position and relative height of the metallic platinum 4f doublets, and the grey bars indicate position and relative height of the SiO_2 2p satellite peaks originating from the $K_{\alpha,3}$ and $K_{\alpha,4}$ peaks, respectively. Both spectra have been shifted to fit the carbon 1s peak to 284.6 eV and normalized to the SiO_2 2p satellite peak. The spectrum taken prior to chemical analysis had a lower signal strength than the spectrum taken afterwards. This resulted in a higher noise level on the blue curve. To measure the spectra the sample is positioned manually and by a visual estimate, likely causing a different area of the sample to be measured and with varying signal intensity. Despite this the doublet peak is still clearly distinguishable.

The platinum doublet peaks in figure 3.12 are slightly shifted to higher binding energies. This could come from partial oxidation of the clusters during transport in air or a final state effect of the clusters, meaning that the electrons are stronger bound to platinum atoms in under coordinated

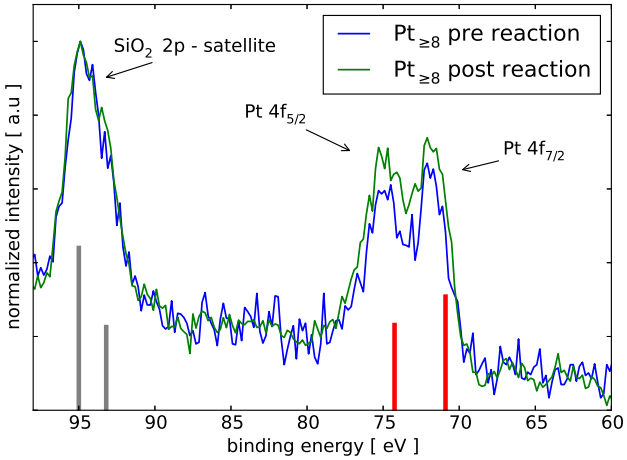

Figure 3.12. XPS spectra of the unselected $Pt_{\geq 8}$ sample before (blue) and after (green) reaction. The detailed scan is zoomed in at the SiO_2 2p satellite peaks and the Pt 4f doublets. Red bars indicate position and relative height of the metallic Pt $4f_{5/2}$ and $4f_{7/2}$. Grey bars indicate position and relative height of the $K_{\alpha,3}$ and $K_{\alpha,4}$ satellite peaks of the SiO_2 2p. Both spectra are normalized to the SiO_2 2p satellite peak and shifted to fit the carbon 1s peak to 284.6 eV. Reprinted from [49].

cites. The parameters of a fit to each peak is shown in table 3.3. After a Shirley background subtraction [43] the integrated peak area increases with 32 %. Though this is not insignificant, the increase is not great considering the potential systematic error in sample positioning during spectroscopic measurements.

Table 3.3: Fitted parameters to the XPS spectra in figure 3.12 from the $Pt_{\geq 8}$ sample. Reprinted from [49].

spectrum	peak name	binding energy [eV]	FWHM [eV]	area [a.u.]
pre reaction	Pt $4f_{7/2}$	71.9	2.6	1.38
	Pt $4f_{5/2}$	75.2	2.4	1.04
post reaction	Pt $4f_{7/2}$	71.8	2.8	1.83
	Pt $4f_{5/2}$	75.0	2.7	1.37

The overview spectra before and after chemical testing are shown in figure A.2 of appendix A together with an overview and detailed scan in figures A.3 and A.4, respectively. All overview spectra show expected features from O_2, C, Pt, and SiO_2. The detailed scan of the Pt_8 cluster show a very small Pt 4f peak where the doublet is barely distinguishable.

3.4.4 DFT simulations on oxygen effects on Pt clusters

The results thus far have proven the Pt_8 cluster catalyst to be able to dissociate hydrogen and improve reaction rate with O_2 added to the gas stream. However, the lack of *in situ* spectroscopic capabilities means that we have no means to experimentally examine the physical and chemical changes of the catalyst. To get a deeper understanding of the model system, a master project was conducted by Mikkel Jørgensen to do DFT simulations [100, 101] on a Pt_8 cluster and study the effects of oxygen [102]. These simulations were not carried out by me, and since my background is as an experimentalist, the details will be covered briefly.

The simulations were made using the GPAW software [103] with the ASE framework [104] and the BEEF-vdW exchange-correlation functional [105]. The initial configuration of the platinum cluster on the SiO_2 α-quartz support [106] is seen in figure 3.13, where grey atoms represent platinum, oxygen is red, and silicon is golden. The black box shows the computational unit cell. The cluster consists of a 7 atom basal plane [90, 107] with the last atom positioned at six different locations, with two examples shown as either on the side of the cluster (transparent green) or on top (transparent blue) of the plane. The final cluster morphology of the six configurations change dramatically after relaxation, as seen in figure 3.14. Each morphological configuration differs significantly from the others, suggesting large variations in chemical activity.

The stability of each cluster is addressed in figure 3.15 where the platinum atom binding energy is plotted for the six configurations shown in figure 3.14. The energies are given with the binding energy of bulk platinum as

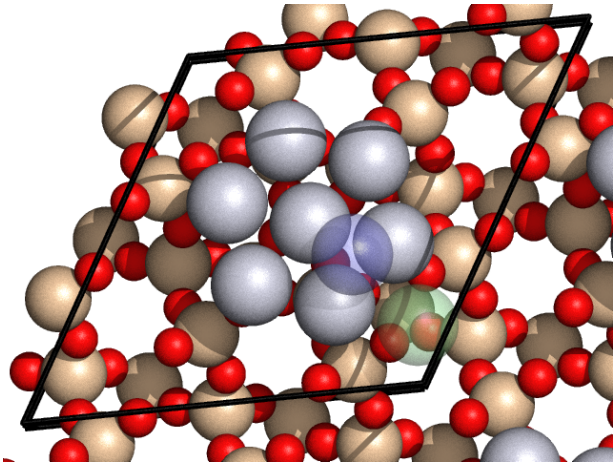

Figure 3.13. The Pt_8 cluster configuration for DFT simulation prior to relaxation. A 7 atom basal plane constitutes the base of the cluster. The 8th platinum atom can be placed at six different configurations, where two are exemplified with transparent blue and green. Platinum atoms are grey, oxygen atoms are red, and silicon atoms are golden. The black box shows the computational unit cell. Reprinted from [49].

reference. All configurations are fairly stable, and half the configurations are significantly more stable than bulk platinum. Again, this suggests a high level of stability of the clusters, in agreement with literature values for Pt_{13} clusters on amorphous silicon [108]. All following simulations were done on the lowest energy cluster. It is found that a single oxygen atom binds strongly to the lowest energy cluster with at least 1.0 eV in all investigated sites. Any oxygen atoms that would reach the cluster would therefore bind strongly to it. All surface oxygen atoms on the cluster or from the support were passivated with a hydrogen atom.

To estimate the activity of the clusters with and without oxygen, hydrogen adsorption was used as a descriptor. This can be done because dissociating hydrogen was found to be barrier-less on some sites, in agreement with literature [109]. For the sake of activity estimates, it is assumed that all sites dissociate hydrogen with no barrier. Since the adsorption and desorption energy for hydrogen are the same and adsorption is barrier-less,

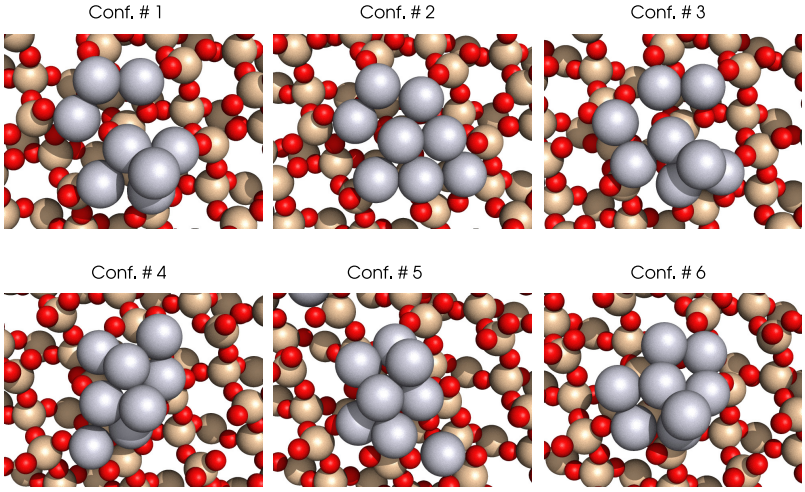

Figure 3.14. Six relaxed atomic configurations of Pt_8 clusters, ordered by decreasing binding energy. Platinum atoms are color coded grey, silicon is golden and oxygen is red. Reprinted from [49].

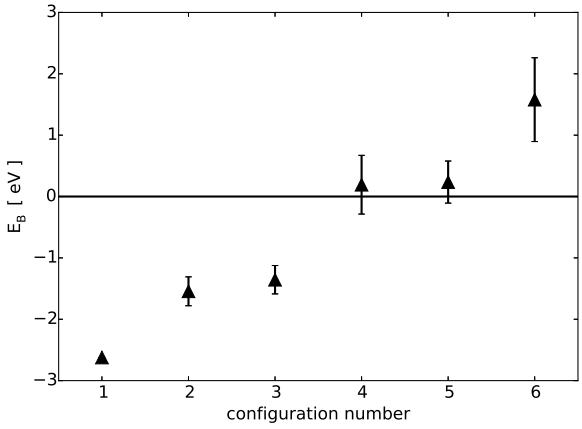

Figure 3.15. Platinum binding energy for different relaxed cluster configurations. The reference level is that of bulk platinum, proving clusters to be highly stable on SiO_2. Reprinted from [49].

the adsorption energy is used as descriptor for the reaction rate. Using Transition State Theory the activity was calculated, shown in figure 3.16 as a black line. The marked points on the graph represent different activities on different sites. Each color represents that same cluster site with (circle) and

without (triangle) oxygen. The variation in binding energy greatly changes the resulting activity, and the dark blue cluster site has a remarkable change in activity when oxygen is added. Sites with energies around $\sim -0.5\,\text{eV}$ will have activities varying greatly even with small changes in energy. Also note that the dark blue circle has a positive energy, meaning that hydrogen will never stick to that surface site when oxygen is present. This proves a site to go from inactive to having a finite activity by changing the oxygen level.

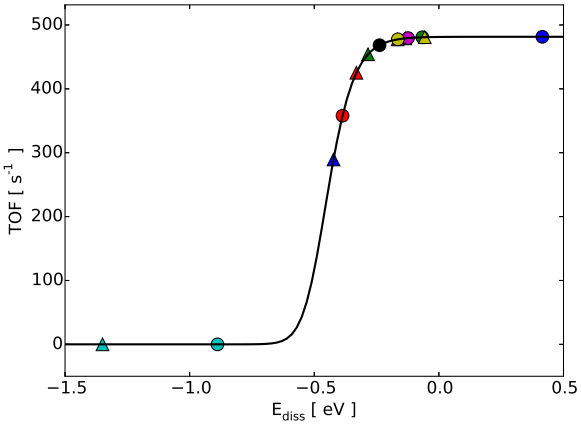

Figure 3.16. Transition State Theory simulations result in the black line and markings represent energies on different adsorption sites with (circles) and without (triangle) oxygen. Numerically estimated reaction rates vary for different adsorption sites. Reprinted from [49].

An important property of the cluster that affects chemical characteristics is the charge distribution on the cluster. Figure 3.17 shows a Bader charge analysis of the most stable cluster with and without oxygen [110]. A Bader charge analysis simply means that a sphere around the center of each atom and with the given atom diameter is created for each atom. The total charge distributed within this sphere is then summed up to give the atomic charge. The charge is represented with the scale bar on the right side of the figure. The left panel in the figure shows the cluster from the side while the right panel shows images from the top perspective. The two upper images

show the cluster without oxygen while the lower images with an added oxygen. To better see the changes in charge distribution on the cluster, the scale is truncated at ±2 e. A clear change of charge distribution is seen on the top platinum atom that changes from neutral to ∼0.4 eV charge by the addition of an oxygen atom. In the top view in the right panel of the figure it is also seen that the atom in the upper left corner of the images changes position, leaving a visible gap between the three atoms in the upper right corner and the rest of the cluster. A notable morphology change like this is bound to change the chemical properties of cluster.

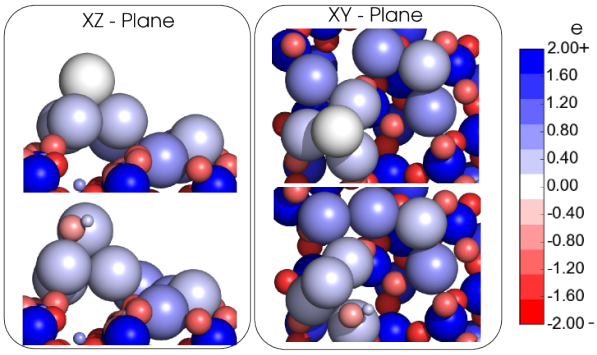

Figure 3.17. A Bader charge analysis of a Pt_8 cluster. Left panel shows a side view of the cluster while the right panel shows a top view of the same cluster. The two top images shows the cluster without oxygen, while an OH group is added in the two bottom images. The Bader charge analysis shows charge distribution between the atoms, color coded according to the color bar on the right. The addition of an oxygen atom increases the charge of the top platinum atom and changes the cluster morphology. Reprinted from [49].

Though the simulations presented provides valuable information about reaction mechanism, cluster stability, cluster morphology, and oxygen effects, there are some obvious limitations to the DFT study. The cluster is very small and our initial thought was they would be easy to compute with DFT, but strong interaction with the support means the unit cell has a considerable size, making computations expensive. Due to a limitation in computational power, only the lowest cluster configuration was examined for the ability to dissociate hydrogen, despite several other configurations

are shown to be very stable. The calculations also only include a single oxygen atom on the surface. While it is a plausible scenario that molecular oxygen is dissociated and one atom sticks to the support as an OH group while the other atom stick to a cluster, the model system does not treat multiple oxygen atoms on the cluster. Based on the experimental study of the $Pt_{\geq 8}$ sample it is probable that other cluster sizes would likely exhibit a similar effect. This would take significantly more computational resources to map out size effects on similar model systems.

The major take-home message from the DFT study is that Pt_8 clusters are highly stable on a SiO_2-support, and oxygen can change the cluster morphology, charge distribution, and chemical properties, providing credibility to the experimental results.

3.5 Conclusion

Mono-disperse Pt_8 clusters on SiO_2 were tested for H_2/D_2 exchange reaction at 1 bar using μ-reactors. Initial experiments demonstrated a clear size effect in the range of 7 to 46 atoms per cluster. The tendency indicated that bigger clusters had a higher TOF. These results proved very hard to reproduce and samples that should be identical, displayed activities varying with more than an order of magnitude.

Oxygen contaminations were found to be the source of great uncertainty in reaction rate and a detailed study found that minute amounts of oxygen added to the gas stream would radically change the performance of the catalyst. A Pt_8 cluster sample was used to demonstrate that 26 ppm of O_2 would decrease the apparent activation energy from 0.83 eV to 0.40 eV and increase the activity, sometimes up to an order of magnitude. The oxygen also introduced a hysteresis effect that was not seen in the clean H_2/D_2 gas stream.

The stability of the catalyst was addressed by characterising an unselected $Pt_{\geq 8}$ sample with XPS and ISS before and after chemical reaction. The

spectra showed little or no change, indicating a high level of stability of the mono-disperse Pt_8 sample.

Numerical simulations by DFT also proved the catalyst to be highly stable, with platinum binding energies to the support that where higher than that of bulk platinum. Simulations also provided information about how the cluster reacts to the addition of an oxygen atom. The cluster morphology and charge distribution changed, providing different hydrogen binding energies at various sites of the cluster. Despite only one oxygen atom per cluster was studied, it demonstrated that oxygen can indeed change the physical and chemical properties of the catalyst. This provides a plausible explanation for the non-Arrhenius behaviour seen in experiments with small amounts of oxygen added to the gas stream.

The documented effects could be the explanation of a high inconsistency in literature concerning activity and apparent activation energy for the studied reaction. A more general conclusion of the study is: beware of ppm levels of impurities in your gas stream!

Chapter 4

Methanation on nickel iron alloys

4.1 Introduction

The production of methane from CO and H_2 has an interesting perspective in converting renewable energy to a chemical energy carrier, since methane has a high energy density and an established infrastructure for distribution and transport [111]. CO can be made from biomass [112] or wood [113] while H_2 could be produced from electro-catalytic water splitting [114] using renewable energy sources or photo-catalytic water splitting directly from sunlight [114–116].

4.1.1 Nickel catalyst

Traditionally, nickel is used as a methanation catalyst [111], and has been studied for more than a century [117]. Nickel has a high activity per unit cost while maintaining a high selectivity towards methane [118]. Many catalytic reactions will occur during methane production from CO and CO_2, with possible reactions, label from R1-8, as follows [119]:

$$R1 : \mathrm{CO} + 3\,\mathrm{H_2} \rightleftharpoons \mathrm{CH_4} + \mathrm{H_2O}$$
$$R2 : \mathrm{CO_2} + 4\,\mathrm{H_2} \rightleftharpoons \mathrm{CH_4} + 2\,\mathrm{H_2O}$$
$$R3 : 2\,\mathrm{CO} + 2\,\mathrm{H_2} \rightleftharpoons \mathrm{CH_4} + \mathrm{CO_2}$$
$$R4 : 2\,\mathrm{CO} \rightleftharpoons \mathrm{C} + \mathrm{CO_2}$$
$$R5 : \mathrm{CO} + \mathrm{H_2O} \rightleftharpoons \mathrm{CO_2} + \mathrm{H_2}$$
$$R6 : \mathrm{CH_4} \rightleftharpoons 2\,\mathrm{H_2} + \mathrm{C}$$
$$R7 : \mathrm{CO} + \mathrm{H_2} \rightleftharpoons \mathrm{C} + \mathrm{H_2O}$$
$$R8 : \mathrm{CO_2} + 2\,\mathrm{H_2} \rightleftharpoons \mathrm{C} + 2\,\mathrm{H_2O}$$

A thermodynamic analysis of corresponding equilibrium constants, (K), is seen in figure 4.1. Reactions with the highest equilibrium constants at 200 °C to 300 °C are R1 and R3 that both produce methane. If only CO is added to the gas stream of a reactor, R1 will be dominant. However, reactions R1, R3, R4, and R5 all have high equilibrium constants, resulting in a high CO consumption [119].

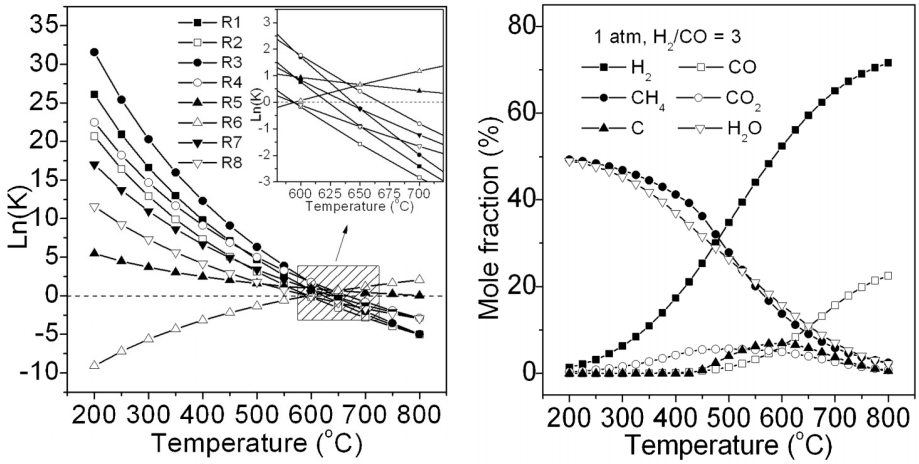

Figure 4.1. Left is shown the equilibrium constants for different reactions involved in methanation. Right is shown the product composition for CO methanation at equilibrium. Reprinted from [119].

4.1.2 Coking

The Boudouard reaction (R4) leaves C on the surface, which is considered a necessary intermediate for methane production [120]. However, if the carbon is not reacted off, it will deactivate the catalyst by coking, which will increase at high temperatures [121]. However, it is difficult to develop an efficient catalyst, running at equilibrium and low temperatures of 200 °C to 400 °C without coking [111, 121, 122].

4.1.3 Group VIII metals

Early studies of group VIII metals show that the metals with weakest bonding to CO have highest activity [123], with catalyst activity ordered as Ru ≫ Fe > Ni > Co > Rh > Pd > Pt > Ir [124]. More recent DFT studies disagree with this trend and show that CO dissociative energy is rate determining, rather than molecular CO binding [118]. The activity follows a volcano curve, as shown in figure 4.2.

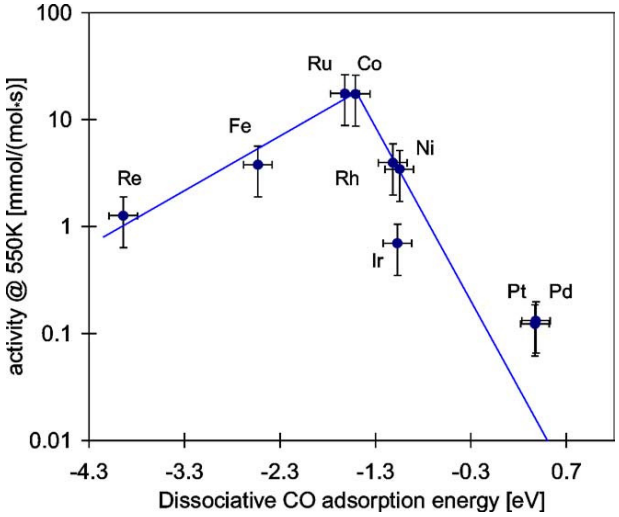

Figure 4.2. Volcano curve for methanation activity on group VIII metals. Ru is known to be a highly active catalyst, but Ni is significantly cheaper. An alloy between Ni and Fe seems a promising candidate. Reprinted from [118].

4.1.4 Alloying

Alloys and inter-metallic compounds have shown promise of high methanation rates and suppressing resilient carbon formation [125–127]. $Ni_{75}Fe_{25}/\gamma$-Al_2O_3 show high CO conversion at 225 °C to 550 °C and selectivity of 99 % towards CH_4 at 300 °C to 450 °C, 30 bar, and a H_2 to CO ratio of 3 [127]. Computational screenings find that NiFe alloys have dissociative binding energies between that of the pure metals, and $Ni_{75}Fe_{25}$ has the highest activity, as seen in figure 4.3 [125]. However, the catalyst activity is known to change with support material [128].

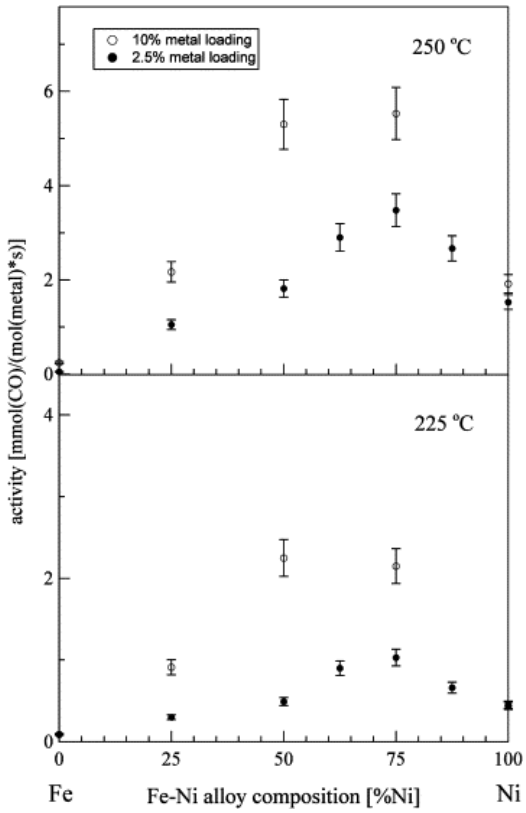

Figure 4.3. Chemical activity for different Ni and Fe alloys under reaction conditions of 2 % CO in 1 bar of H_2. Reprinted from [125].

H_2-TPR is used to characterize surface carbon species. After carbon deposition on Ni by CO dosage at 500 K to 625 K and 1 bar, two CH_4 peaks

result from heating in 1 bar of H_2. The first has a peak temperature at (200 ± 20) °C and the second lies at (400 ± 30) °C [129], representing two different forms of carbon on the surface, one more strongly bound than the other. The surface carbon formation has a dramatic effect on the performance of the catalyst [130], and suppressing carbon formation has been demonstrated by surface alloying with Sn [131]. Nano-particles with a Ni-Fe shell and a Ni core also show improved stability by suppressing carbon formation [132].

4.2 Sample treatment

Several samples were used for the following experiments. An overview of the samples can be seen in table B.1 of appendix B. Before nano-particle deposition, all reactors where sonicated in ethanol and subsequently washed in milli-Q water (18.2 MΩ cm) to clean off contaminants that might be present from the fabrication process. The empty reactor chip was then transferred in to the cluster source where it was sputtered for 40 min with Ar^+ accelerated to 1 keV. This was done to clean the reactor from carbon species on the surface. Nano-particles were then deposited onto the reactor, using the cluster source described in section 2.4.1, and the chip was taken out in air for subsequent cold-bonding, as described in section 2.1.4, followed by chemical testing.

4.2.1 Testing chemical activity

After characterisation of the sample, it was sealed by anodic bonding, as explained in section 2.1.4. The sample was then mounted in the μ-reactorNG set-up and pumped down. First the sample was heated in 1 bar of H_2 to 225 °C to react off carbon and other contaminants from exposure to air. This was deliberately not done in O_2 to prevent the iron content in the particles from segregating to the surface and covering the particles in an FeO_x shell. After cool down, a flow of H_2, CO, and Ar was started in

a ratio of 100:2:10, respectively. The methanation treatment is shown in figure 4.4. After the flows stabilized and the sample had cooled to RT, the sample was heated in steps for 1 h each, to 100 °C, 125 °C, 150 °C, 175 °C, 200 °C and 225 °C. At 225 °C the temperature was kept for 2 h after which the same steps were done down to 100 °C. The sample was kept at this temperature till the reactor was pumped down. This was done to prevent carbon formed on the surface during reaction to be reacted off with residual hydrogen. At ∼20 h in figure 4.4 the system was then flushed twice with Ar and then filled with hydrogen. A temperature ramp to 225 °C and at 2 °C s^{-1} in H_2 was made for a H_2-TPR that forms $C + 2\,H_2 \longrightarrow CH_4$. The system is then flushed with Ar again and the process is repeated. This also reactivated the catalyst after methanation.

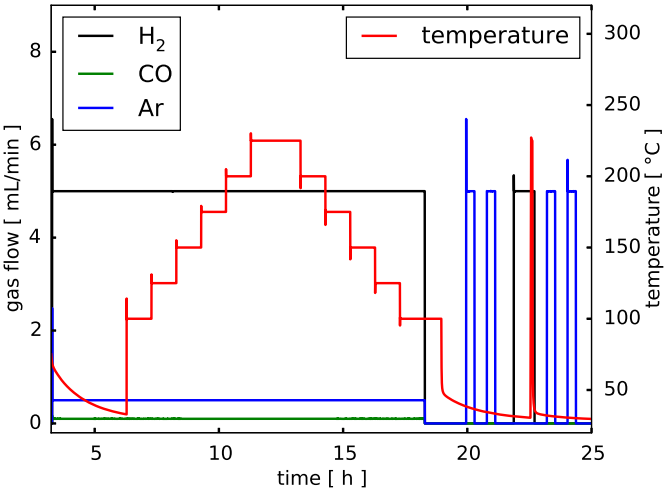

Figure 4.4. Sample treatment for methanation on $Ni_{75}Fe_{25}$ samples.

Limitations on pressure

Industrial methanation is done at very high pressures because of the benefit of increased entropy. The μ-reactor is limited to 2.5 bar by the PC at one of the outlets of the chip. However, the reactor lids would routinely break

at the combination of high pressure and temperature. In figure 4.5 are shown four broken reactors. The two on the left had their lids break around the reactor volume, effectively blowing them off. The two reactors on the right had their lids soften by high temperatures and form a bubble over the reactor volume. For this reason the pressure was lowered to 1 bar, providing stable measurements with intact lids.

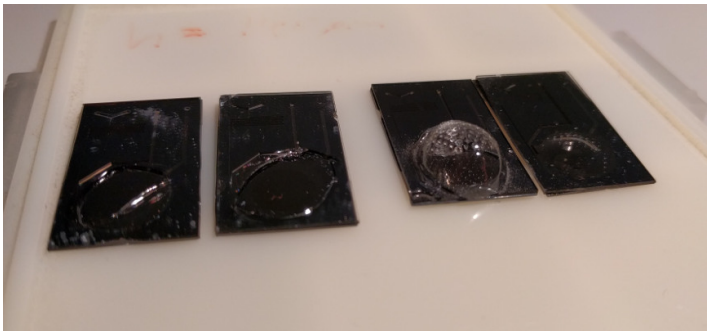

Figure 4.5. Broken rectors. The two left reactor chips had the reactor lid exploded off. The lids on the two right reactors softened during heating and bubbled up due to the pressure difference.

4.2.2 Characterization

ISS and XPS

ISS and XPS was done in the UHV chamber attached directly to the cluster source described in section 2.4.1. After cluster deposition, the samples were transferred to the analysis chamber under UHV conditions. The analysis chamber has a base pressure of 10^{-11} mbar. During ISS, a helium pressure of 5×10^{-8} mbar was established and He^+ were accelerated to 1 keV. For XPS a magnesium anode was used, with FWHM of 0.7 eV without a monochromator for the X-ray gun. Parameter details used to obtain the XPS spectra are listed in table B.2 in appendix B.
Before cluster deposition, the reactor was sputtered with Ar^+ at 1 keV for 40 min to clean the reactor. In figure B.2 of appendix B are shown ISS and XPS spectra of an empty reactor before and after sputtering. The ISS

spectra show a large broad feature of carbon species before sputtering, and a low intensity of the silicon peak. There is also a small peak visible at ∼680 eV that could come from potassium or calcium contaminations. This is clearly gone after the sputtering. The XPS spectra show both silicon and oxygen from the reactor chip. Before sputtering, there is a clear carbon peak that practically disappears afterwards. There are no detectable traces of potassium or calcium, proving the effectiveness of the cleaning procedure.

SEM

After ISS and XPS characterization, some samples were transported to a SEM for imaging. At the time of writing, only one sample of 9 nm particles was imaged at several positions spread across the reactor using 5.00 keV electrons. After chemical testing the sample was cut open, as described in section 2.1.4 and imaged again. Using the reactor pillars as landmarks, it was possible to image the exact same position before and after chemical testing, as seen in figure B.3 of appendix B. Future plans include similar imaging the other three sample sizes.

4.3 Results

4.3.1 Activity measurements

The chemical activity tests were done on numerous $Ni_{75}Fe_{25}$ samples for reproducibility. An outline of the collected data is seen in figure 4.6 from one 3.5 nm sample, three 5 nm samples, three 7 nm samples, and one 9 nm sample. Each particle size is plotted in separate sub-plots. In general, the most active size is the 7 nm samples. Initially, there was a large distribution in activity within each particle size. The most active 7 nm sample was almost at full conversion at 200 °C while the least active 7 nm sample showed roughly half that activity at 225 °C. In an attempt to remedy this, the signals were normalized to the nickel and iron peak of the ISS spectra in figure 4.10, which should be proportional to the amount of metal surface

atoms. Some samples did not have ISS spectra and were therefore not normalized. This resulted in much more coherent data on the 7 nm samples. The three 5 nm samples are less active, but also show a large dispersion. Since only one 5 nm sample had an ISS spectrum, it is unknown whether normalization would benefit the trend. Only one sample each of 3.5 nm and 9 nm where tested. Their activity are both low and roughly the same in the beginning, but the 9 nm sample deactivates faster. However, with the dispersions seen on the other samples, this is not significant.

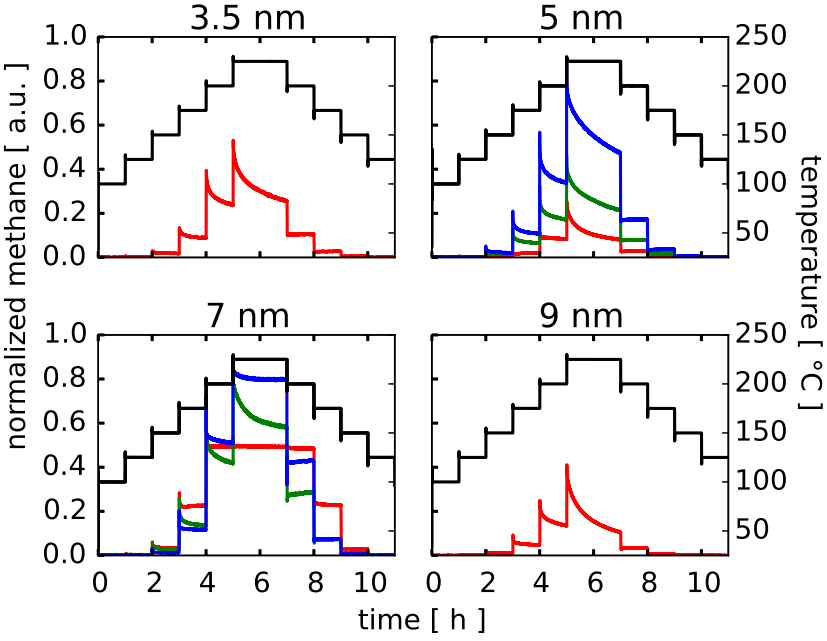

Figure 4.6. Raw methanation data normalized to $^{m}/_{z} = 2$ signal from $Ni_{75}Fe_{25}$ samples. Each sub-plot shows a specific sample size. The black lines show the temperature, indicated on the right axis.

To analyse the data, the methane signal for each temperature plateau, that lasted for 1 h, was averaged to get a data point at each temperature step. The first and last 3 min were omitted to leave out the actual change in temperature. This data is plotted as a function of temperature in figure 4.7. Error bars are based on a collection of all available methane data for the

given sample size and temperature step. It is clear that the 7 nm samples are more active than the rest, but the activity of 3.5 nm, 5 nm, and 9 nm samples cannot be distinguished from each other with the large error bars.

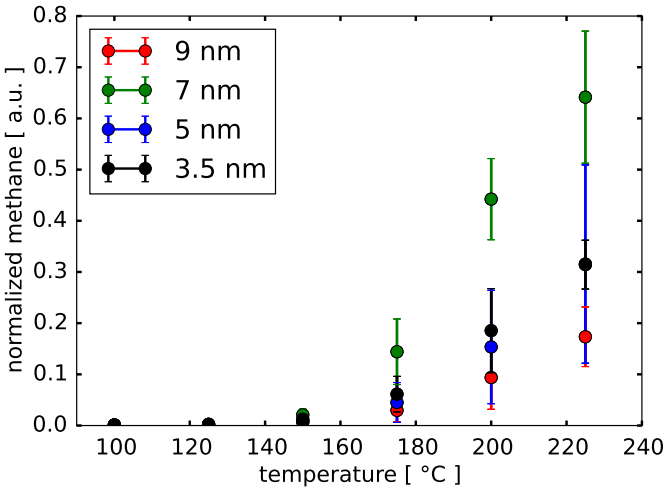

Figure 4.7. Methanation on $Ni_{75}Fe_{25}$ samples as function of temperature.

After each methanation cycle, the catalyst was treated in 1 bar of pure H_2 at 225 °C to react off carbon on the surface. In figure 4.8 is shown the activity data from two subsequent methanation measurements on the 9 nm MR59 sample. The activity on the first (green) methanation cycle is only slightly larger than the second (blue), indicating a reactivation of the catalyst. This shows that the reaction conditions mostly deposits carbon that is weekly bound to the catalyst. The small deactivation that does occur might come from a small amount of strongly bound carbon that does not react off during reduction.

Arrhenius plots

An Arrhenius plot of the data from figure 4.7 is seen in figure 4.9. All samples exhibit a clear Arrhenius behaviour in a broad temperature range. At the highest temperatures (to the left) the 7 nm samples bend off due

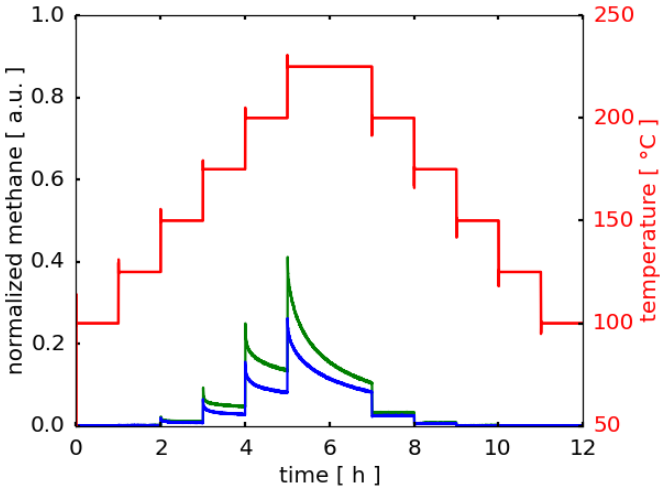

Figure 4.8. Re-activation of 9 nm $Ni_{75}Fe_{25}$ sample (MR59). By reacting off carbon with hydrogen at 225 °C the sample has almost the same activity before (green) and after (blue) reduction.

to mass transport limitations. The samples with lower activities bend off at the lower temperatures (to the right) due to background signals being dominant.

In table 4.1 are plotted the fitted parameters to the Arrhenius equation. Data points close to full conversion are neglected because they are dominated by back reaction. Data points that show no activity are also neglected because they are dominated by the background. Again, the 7 nm samples stand out with higher apparent activation energy and pre-exponential factor. However, considering the error bars in figure 4.9, this could very well be a coincidence, since the slope or vertical off-set could be changed and still lie within the error bars.

Sources of error

There are many plausible sources of systematic error that can cause the large fluctuations in activity. They mostly relate to the state of the catalyst deposited in the reactor. The mass selection of the particles from the

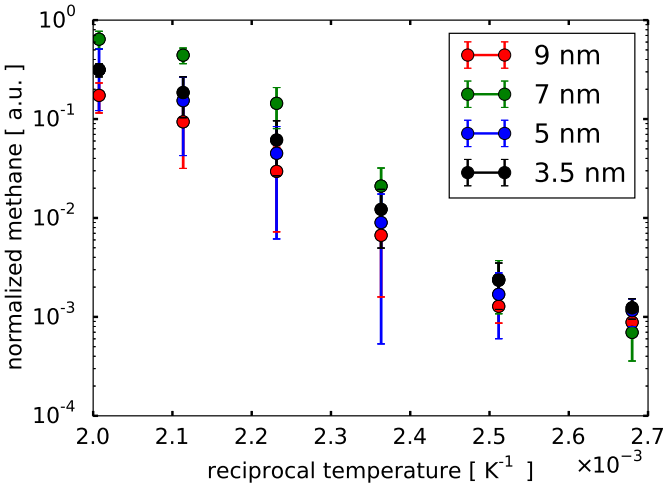

Figure 4.9. Arrhenius plot of methanation on $Ni_{75}Fe_{25}$ samples.

Table 4.1: Apparent activation energies and pre-exponential factors for methanation on $Ni_{75}Fe_{25}$ particles of 3.5 nm, 5 nm, 7 nm and 9 nm.

particle size [nm]	E_{act} [eV]	A [a.u.]
3.5	0.74	26.6
5	0.76	27.3
7	0.99	35.8
9	0.79	27.9

cluster source is fairly stable and should be considered robust. However, the cluster beam could be slightly inhomogeneous, and perfect aiming the beam onto the reactor volume sometimes fails due to small misalignment of the aperture or charging of the sample. This is usually detected by visual inspection since the SiO_2 changes color with nano-particle coverage. The samples with inhomogeneous coverage are then discarded. The cluster density is also measured by SEM at several locations before chemical activity testing. If the deposition was inhomogeneous, it would be detected by the particle density count of the SEM, but this was never seen in this project. Another plausible cause of error is the anodic cold bonding, described in

section 2.1.4. The reactor was carefully placed on the cooling finger by hand using visual estimate for alignment. The aluminum heating block was also placed by hand on top of the reactor. If one or both of these are misaligned, a part of the reactor volume will experience excessive heating or insufficient cooling that could cause the catalyst to sinter at certain areas of the reactor. If the reactor is slightly tilted, the cooling block is not in proper thermal contact with the reactor, and the same problem would result. These sintering problems would all be detected by the particle count from SEM imaging when the reactors are opened after chemical testing.

The catalyst could also be affected by foreign compounds in the reactor. These could come from the fabrication process in the clean room where multiple users on the machinery could leave contaminants that either poison the catalyst or acts as a promoter. However, this would most likely be detected by XPS or ISS, since especially ISS is extremely sensitive to surface compounds. For the methanation project, reactors were systematically sputtered with Ar^+ to thoroughly clean the reactor before particle deposition.

Several aspects of the temperature could also be the cause of inconsistency of catalytic data. An unstable RTD would be fatal to the catalytic experiments, that have an exponential dependence of temperature. However, RTDs are widely used for thermal measurements, and the four point probed measurement will result in very reliable detection of resistance. However, some experiments have shown loss of one heater during reaction, causing a large temperature gradient across the reactor chip. These experiments are routinely ignored. Recently, the power input is logged together with other data, making uneven heating easily detectable. The normal gradient of up to 20 °C cannot account for the inconsistency observed in the presented data.

4.3.2 Characterisation

As this is a work in progress, not all samples were characterized with ISS and XPS before activity measurements. SEM imaging is aimed at being done on one sample per size. Due to practical errors and broken reactors, this has not been done on all sample size at the time of writing.

ISS

ISS spectra of several samples are shown in figure 4.10. Each sub-plot shows different sample sizes. Only one sample was measured for each of the 3.5 nm, 5 nm and 9 nm samples, while three 7 nm samples were measured and color-coded according the the sample name. Each spectra show the second scan, and used the first scan to clean the sample by sputtering during measurement. All spectra are normalized to the silicon peak. Nickel and iron are so close together in mass that their ISS peaks overlap and are indistinguishable.

All spectra for 3.5 nm, 5 nm and 9 nm samples look very similar. The silicon to oxygen ratio is $\sim$2.5 and the nickel and iron peaks are the same or only slightly larger than the silicon peak. The most noticeable spectra are that of the 7 nm particles. The oxygen peaks are fairly similar, but the nickel and iron peaks vary significantly. Given that the coverage is calculated as a constant fraction of the surface area, all samples should have the same catalyst surface area. The variations could come from measuring outside the reactor volume, since the apparatus is aimed using the naked eye. There could also be a preferential build-up of carbon species on the nano-particles or the support. This could be explained by different sticking coefficients on the particles and surface, and would explain the differences in nickel and iron peak intensities. However, then all the other samples should be off by the same amount, which seems unlikely. It is also possible that something went wrong during the deposition, and that the catalyst coverage is simply different.

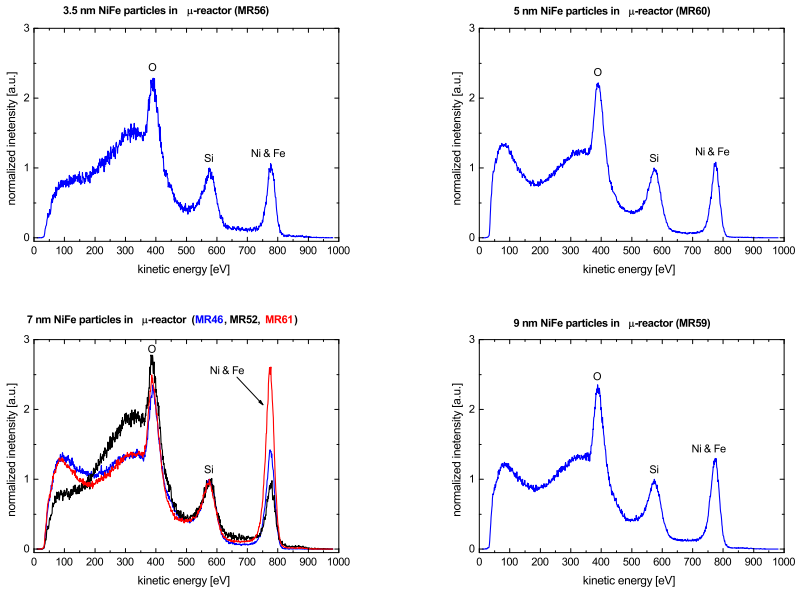

Figure 4.10. ISS spectra of $Ni_{75}Fe_{25}$ samples. All spectra show the second scan and are normalized to the silicon peak hight at ∼590 eV. He^+ are accelerated to 1 keV. Figure by Béla Sebök.

XPS

Five samples were characterized with XPS after nano-particle deposition. The overview spectra are shown in figure B.1 in appendix B. Not all samples were characterized with XPS, since this was not routinely done for the first samples made. All spectra are shifted in energy to fit the SiO_2 2p peak at 103.4 eV and normalized to that same peak area. The spectra show features from silicon, oxygen, nickel, iron, and carbon, as is expected.

Figure 4.11 shows detailed scans of the Ni $2p_{3/2}$ (left) and Fe $2p_{3/2}$ (right) peaks for all measured samples. The peaks are shifted to fit the detailed scan of the SiO_2 2p peak at 103.4 eV and also normalized to the peak area of that peak. Most spectra look quantitatively alike. Noticeably, the two 7 nm samples; MR52 and MR61, look very similar, despite that the corresponding nickel and iron peaks of the ISS spectra in figure 4.10 are off

by a factor of ∼2.6. The reason for the inconsistency is unknown at the time of writing.

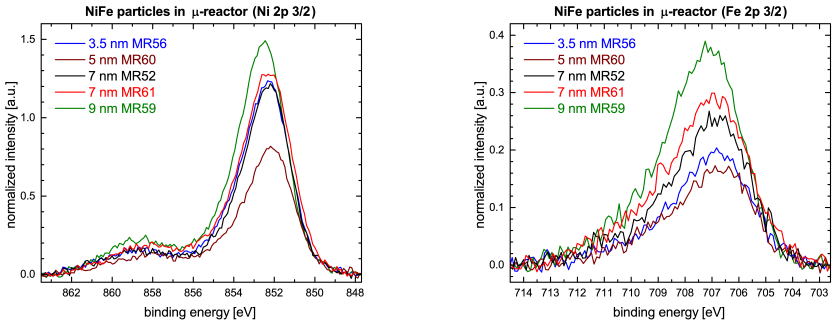

Figure 4.11. Left shows the Ni $2p_{3/2}$ peak and right shows the Fe $2p_{3/2}$ of five different $Ni_{75}Fe_{25}$ samples at varying sizes. All spectra are normalized to the SiO_2 2p peak area and shifted to fit the SiO_2 2p peak at 103.5 eV. A Shirley background has also been subtracted. Figure by Béla Sebök.

In table 4.2, the iron content of the nano-particles is shown. There is no big trend to be seen in the iron content as a function of size. MR61 and MR52, that showed the biggest difference in chemical activity and ISS spectra show the exact same nickel to iron ratio. This is not a contradiction, since the ratio can still be constant if there are more particles. The XPS data from MR34 and MR36 is not shown in figure 4.11 since a detailed scan of the SiO_2 2p peak was not made, and the normalization was therefore not possible. However, the ratios should be the same. The MR56 sample had a very low signal intensity and the nickel and iron peaks are dominated by noise, which could explain the low iron content.

SEM

Several questions can be answered by a characterization using SEM. A SEM study of the 9 nm $Ni_{75}Fe_{25}$ sample MR59 is shown in figure 4.12. The left image shows a portion of the reactor with clearly visible nano-particles, taken before anodic bonding and chemical testing. The right figure shows

Table 4.2: Nickel to iron ratio in $Ni_{75}Fe_{25}$ samples from XPS. The peaks of the detailed scans in figure 4.11 are subtracted a Shirley background and integrated. The resulting iron content is calculated.

sample	particle size [nm]	$\frac{Fe}{Ni+Fe}$ [%]
MR59	9	26
MR61	7	24
MR52	7	24
MR46	7	39
MR60	5	23
MR34	5	27
MR36	5	28
MR56	3.5	18

the same portion of the reactor, but taken after chemical experiments. The right image has slightly lower contrast because carbon is deposited on the reactor during imaging as a result of interaction with the electron beam. In figure B.4 of appendix B another portion of the same reactor is imaged, demonstrating a higher contrast because of no carbon deposition. Taking a closer look at figure 4.12, it is clear that the particles show no visible change in size or position. All particles in the left image keep their position and size in the right image, proving that catalyst is indeed resistant to sintering. The concept of identical location SEM is more easily identified in figure B.3 where the same rough edge of a reactor pillar is seen before and after chemical reaction. The $Ni_{75}Fe_{25}$ particles are seen to be unaltered from the reaction conditions. This also proves that anodic bonding is not harmful to the catalyst. Imaging was done on several spots of the reactor, to ensure the depositions were homogeneous and results were not simply a local phenomenon.

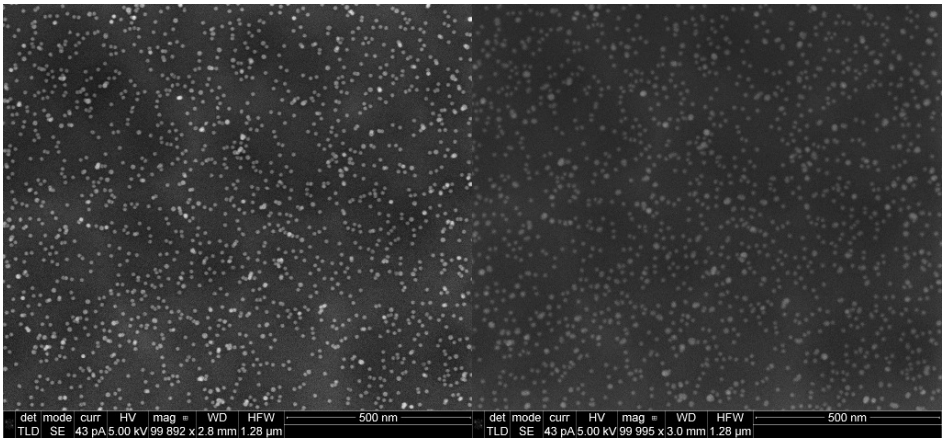

Figure 4.12. Identical location SEM of 9 nm $Ni_{75}Fe_{25}$ sample before (left) and after (right) chemical reaction. The qualitative and quantitative similarity of the two images proves a high resistance to sintering. Figures by Elisabetta Maria Fiordaliso.

Particle size distribution

Figure 4.13 shows the size distributions for each particle mass. The histogram is made from bright field TEM images of nano-particles deposited on copper grids with lacey carbon, and data is treated with imageJ. The diameters are calculated based on the projected particle area, assuming spherical particles. The red curves are Gaussian fits to the histograms, and uncertainties represent two sigma. All peaks are clearly separated, proving a narrow size distribution. Only the 9 nm particles (brown) show some double mass particles at ∼11 nm.

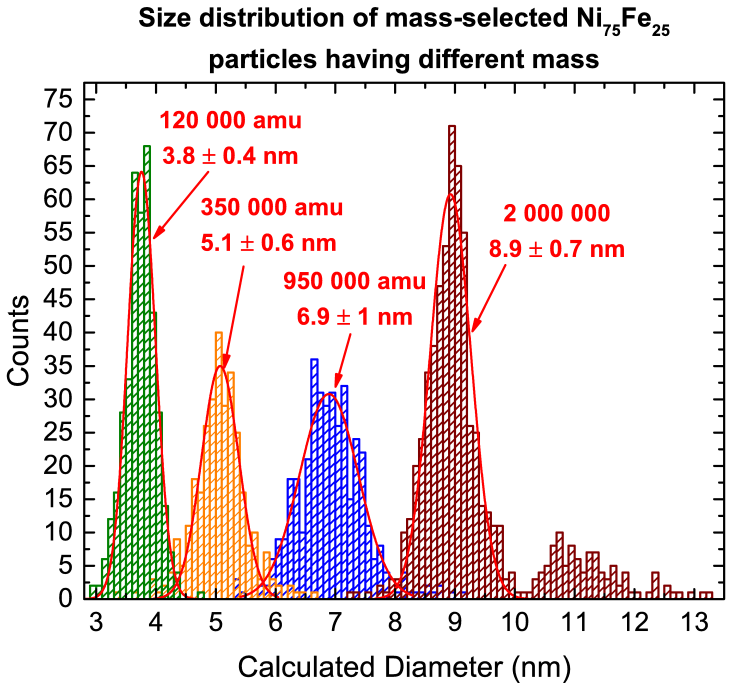

Figure 4.13. Histogram of size distributions from TEM. The four particle sizes are clearly distinguishable. Red curves show Gaussian distribution fits, and uncertainties are given in two sigma. Figure by Béla Sebök.

4.4 Conclusion and outlook

$Ni_{75}Fe_{25}$-alloy was tested for catalytic activity towards methanation from carbon monoxide and hydrogen using nano-particles of 3.5 nm, 5 nm, 7 nm and 9 nm. The nickel to iron ratio was chosen based on the literature suggesting this to be of highest activity [125]. The presented data make up a half finished story, where experimental procedures were gradually altered as new knowledge was obtained. The results suggest that there is indeed a trend in activity as function of size, with the 7 nm particles being the most active. SEM images also suggest that the catalyst does not sinter under reaction conditions, suggesting that carbon formation on the catalyst surface is the main source of de-activation. This is also made clear by the

catalysts ability to re-activate by hydrogenation at 225 °C.

A lot of work is yet to be done. Several sizes should be re-made with consistent characterisation before and after reaction, using ISS and XPS. The causes for varying chemical activity between samples that should be identical is unknown at the moment, but the chemical activity seems to correlate proportionally with the nickel and iron peak intensity of the ISS spectra.

In the future, a similar size study on pure nickel particles will make an interesting addition to the initial results. This will prove whether the $Ni_{75}Fe_{25}$ alloy is indeed more active and more resistant to coking.

Chapter 5

Conclusion and outlook

The unifying aspect of the research projects of this thesis, is the use of μ-reactors. Two separate projects were conducted independently, and concluded in separate sections below.

H_2/D_2-exchange reaction on platinum clusters

The H_2/D_2-exchange reaction was studied on mono-disperse platinum clusters. Using Pt_8 clusters as a reference system, it was found that adding 26 ppm of O_2 to the gas stream had a significant effect on the clusters ability to dissociate and recombine hydrogen. The apparent activation energy decreased from 0.83 eV to 0.40 eV and the activity increased dramatically. A gradual increase and decrease in temperature during reaction revealed a significant hysteresis of the oxidized cluster, that was not seen in the reduced system.

The stability of the clusters was addressed by XPS and ISS characterisation before and after chemical testing. The catalyst showed a very high stability. Complimentary DFT simulations also confirm a very high binding energy of the cluster to the support. Adding an oxygen atom to the cluster changed the cluster morphology, electrical charge distribution, and chemical activity of the cluster, proving oxygen contaminations as a plausible cause for the increased activity.

Methanation on nickel-iron alloys

Nano-particles of $Ni_{75}Fe_{25}$ was studied for methanation from carbon monoxide and hydrogen. The nano-particles used were of 3.5 nm, 5 nm, 7 nm and 9 nm. At the time of writing, the project is still in progress, but current results indicate that 7 nm particles are most active.
The catalyst was characterized with ISS, XPS, and SEM before and after reaction. All surface techniques suggest that the catalyst is highly resistant to sintering, and identical location SEM shows that no particles move or sinter during reaction of up to 225 °C.

The future of μ-reactors for heteroneneous catalysis

Sources of systematic error should be further investigated. Possible sources could include; inconsistent heating and cooling during bonding, uneven distribution of particles, foreign compounds from the fabrication process, deactivation from exposure to atmosphere, heat gradients, and RTD failure. A substantial source of error came from residual oxygen in the gas lines. This has been thoroughly investigated with the H_2/D_2-exchange reaction on platinum, and the problem is considered solved. It was recently implemented that the input power is logged along with temperatures, pressures etc. during reaction. This should help troubleshooting for inconsistencies in reactor heating and temperature readout. The problem of temperature gradients has already been addressed and the gradients decreased. However, completely eliminating them has proven challenging. To lower the gradient further, it is suggested to extend the heater closest to the interface block, thereby heating more at the part of the reactor volume with the highest temperature gradient. An initial estimate of the particle distribution is obtained by visual estimate, and proves a fairly good indicator. Minute amounts of foreign compounds have been observed by ISS. The origin of these compounds is unknown, but by routinely cleaning the reactors with ethanol, water, and sputtering can remove the contaminants. A systematic

characterisation by ISS and XPS will prevent similar contamination problems in the future. Sources of error will continue to be addressed through further experiments using μ-reactors.

The μ-reactors are a powerful platform that allows a unique model system, i.e. mass selected nano-particles and clusters, to be studied under relevant reaction conditions. The two available set-ups are relatively easy to handle on a daily basis, are semi-automated to operate, and allow a high throughput of samples. The reactors suffer under a lack of *in situ* spectroscopy capabilities. This provides challenges when interpreting data. But no one said it should be easy.

Bibliography

[1] Berzelius, J., Jahres-Bericht über die Fortschritte der Physichen Wissenschaften, Tübingen, **1836**.

[2] Somorjai, G. A.; Li, Y., Introduction to surface chemistry and catalysis, second edition, John Wiley & Sons, **2010**.

[3] Chorkendorff, I.; Niemantsverdriet, J. W., Concepts of Modern Catalysis and Kinetics, second edition, Wiley-VCH Verlag GmbH, **2007**.

[4] Haber, F.; van Oordt, G., *Zeitschrift für Anorg. Chemie* **1905**, 44 (1), 341–378.

[5] Moulijn, J. A.; Makkee, M.; van Diepen, A., Chemical Process Technology, John Wiley & Sons, **2001**.

[6] IEA, Technology Roadmap: Carbon capture and storage, **2013**.

[7] IEA, Technology Roadmap: Hydrogen and fuel cells, **2015**.

[8] Somorjai, G. A.; Park, J. Y., *Phys. Today* **2007**, 60 (10), 48–53.

[9] Ertl, G., *Crit. Rev. Solid State Mater. Sci.* **1982**, 10 (4), 349–372.

[10] Nørskov, J. K.; Houmøller, A.; Johansson, P. K.; Lundqvist, B. I., *Phys. Rev. Lett.* **1981**, 46 (4), 257–260.

[11] Stoltze, P.; Nørskov, J., *Phys. Rev. Lett.* **1985**, 55 (22), 2502–2505.

[12] Freund, H.-J.; Kuhlenbeck, H.; Libuda, J.; Rupprechter, G.; Bäumer, M.; Hamann, H., *Top. Catal.* **2001**, 15 (2-4), 201–209.

[13] Schlögl, R.; Schoonmaker, R. C.; Muhler, M.; Ertl, G., *Catal. Letters* **1988**, 1 (6-7), 237–241.

[14] Haberland, H.; Karrais, M., *J. Vac. Sci. Technol. A* **1992**, 10 (5), 3266–3271.

[15] von Issendorff, B.; Palmer, R. E., *Rev. Sci. Instrum.* **1999**, 70 (12), 4497.

[16] Heiz, U.; Vanolli, F.; Trento, L.; Schneider, W.-D., *Rev. Sci. Instrum.* **1997**, 68 (5), 1986.

[17] Kunz, S.; Hartl, K.; Nesselberger, M.; Schweinberger, F. F.; Kwon, G.; Hanzlik, M.; Mayrhofer, K. J. J.; Heiz, U.; Arenz, M., *Phys. Chem. Chem. Phys.* **2010**, 12 (35), 10288–91.

[18] Henriksen, T. R.; Olsen, J. L.; Vesborg, P. C. K.; Chorkendorff, I.; Hansen, O., *Rev. Sci. Instrum.* **2009**, 80 (12), 124101.

[19] Jensen, R., µ-reactors for Heterogeneous Catalysis, PhD thesis, Technical University of Denmark, **2012**.

[20] Vesborg, P. C. K.; Olsen, J. L.; Henriksen, T. R.; Chorkendorff, I.; Hansen, O., *Chem. Eng. J.* **2010**, 160 (2), 738–741.

[21] Trimarco, D. B.; Pedersen, T.; Hansen, O.; Chorkendorff, I.; Vesborg, P. C. K., *Rev. Sci. Instrum.* **2015**, 86 (7), 075006.

[22] Andersen, T.; Jensen, R.; Christensen, M. K.; Pedersen, T.; Hansen, O.; Chorkendorff, I., *Rev. Sci. Instrum.* **2012**, 83 (7), 075105.

[23] Vesborg, P. C. K.; Olsen, J. L.; Henriksen, T. R.; Chorkendorff, I.; Hansen, O., *Rev. Sci. Instrum.* **2010**, 81 (1), 016111.

[24] Madou, M. J., Fundamentals of microfabrication: the science of miniaturization, second edition, CRC press, **2002**.

[25] Kehres, J., Dynamical properties of nano-structured catalysts for methane conversion: an in situ scattering study, PhD thesis, Technical University of Denmark, **2011**.

[26] Roth, A., Vacuum Technology, third edition, Elsevier Science BV, Amsterdam, **1990**.

[27] O'Hanlon, J. F., A User's Guide to Vacuum Technology, John Wiley & Sons, **2003**.

[28] Quaade, U. J.; Jensen, S.; Hansen, O., *J. Appl. Phys.* **2005**, 97 (4), 1–5.

[29] Redhead, P., *Vacuum* **1962**, 12 (4), 203–211.

[30] Ertl, J.; Küppers, J., Low energy electrons and surface chemistry, second edition, VCH, **1985**.

[31] Miller, P. E.; Denton, M. B., *J. Chem. Educ.* **1986**, 63 (7), 617–623.

[32] Paul, W.; Steinwedel, H., *Zeitschrift für Naturforsch. A* **1953**, 8 (7), 448–450.

[33] Paul, W.; Reinhard, H. P.; von Zahn, U., *Zeitschrift für Phys.* **1958**, 152 (2), 143–182.

[34] Inczédy, J.; Lengyel, T.; Ure, A. M.; Gelencsér, A.; Hulanicki, A., *Blackwell, Oxford* **1997**.

[35] Einstein, A., *Ann. Phys.* **1905**, 4, 132–148.

[36] Einstein, A., The Nobel Prize in Physics, `http://www.nobelprize.org/nobel_prizes/physics/laureates/1921/`, **1921**, [Online; accessed 26-January-2016].

[37] Chorkendorff, I., Surface Physics / Chemistry, **2010**.

[38] Krause, M.; Ferreira, J., *J. Phys. B At. Mol. Phys.* **1975**, 8 (12), 2007–2014.

[39] Wagner, C.; Riggs, W.; Davis, L.; Moulder, J., Handbook of X-ray photoelectro spectroscopy, **1978**.

[40] Niemantsverdriet, J. W., Spectroscopy in catalysis, third edition, John Wiley & Sons, **2007**.

[41] Somorjai, G. A., Chemistry in two dimensions: surfaces, Cornell University Press, **1981**.

[42] Seah, M.; Dench, W., *Surf. interface Anal.* **1979**, 1 (1), 2–11.

[43] Shirley, D. A., *Phys. Rev. B* **1972**, 5 (12), 4709–4714.

[44] Brongersma, H. H.; Groenen, P.; Jacobs, J.-P., *Mater. Sci. Monogr.* **1995**, 81, 113–182.

[45] Brandon, D.; Kaplan, W., in Microstruct. Charact. Mater., John Wiley & Sons, Ltd, Chichester, UK, **2008**, 261–331.

[46] Atkins, P.; de Paula, J., Atkins' Physical Chemistry, 8th edition, Oxford University Press, **2006**.

[47] Strebel, C. E., Structure and reactivity of nano-particles, PhD thesis, Technical University of Denmark, **2012**.

[48] Schweinberger, F. F., Catalysis with supported size-selected Pt clusters, PhD thesis, Technische Universität München, **2013**.

[49] Riedel, J. N.; Rötzer, M. D.; Jørgensen, M.; Vej-Hansen, U. G.; Pedersen, T.; Sebök, B.; Schweinberger, F. F.; Vesborg, P. C. K.; Hansen, O.; Schiøtz, J.; Heiz, U.; Chorkendorff, I., H_2/D_2 exchange reaction on mono-disperse Pt clusters: Enhanced activity from minute O_2 concentrations, **2016**, submitted.

[50] Cheng, H.-P.; Landman, U., *J. Phys. Chem.* **1994**, 98 (13), 3527–3537.

[51] Bromann, K.; Brune, H.; Félix, C.; Harbich, W.; Monot, R.; Buttet, J.; Kern, K., *Surf. Sci.* **1997**, 377 (1-3), 1051–1055.

[52] Rötzer, M. D., HD exchange on supported, size-selected Pt clusters in µ-reactors under ambient pressure, Master's thesis, Technische Universität München, **2013**.

[53] Heiz, U.; Sanchez, A.; Abbet, S.; Schneider, W.-D., *J. Am. Chem. Soc.* **1999**, 121 (13), 3214–3217.

[54] Sanchez, A.; Abbet, S.; Heiz, U.; Schneider, W.-D.; Häkkinen, H.; Barnett, R. N.; Landman, U., *J. Phys. Chem.* **1999**, 103 (48), 9573–9578.

[55] Abbet, S.; Sanchez, A.; Heiz, U.; Schneider, W.-D.; Ferrari, A. M.; Pacchioni, G.; Rösch, N., *J. Am. Chem. Soc.* **2000**, 122 (14), 3453–3457.

[56] Fujitani, T.; Nakamura, I.; Akita, T.; Okumura, M.; Haruta, M., *Angew. Chemie - Int. Ed.* **2009**, 48 (50), 9515–9518.

[57] Bond, G. C., *Surf. Sci.* **1985**, 156, 966–981.

[58] Honkala, K.; Hellman, A.; Remediakis, I.; Logadottir, A.; Carlsson, A.; Dahl, S.; Christensen, C.; Nørskov, J. K., *Science (80-.).* **2005**, 307, 555–558.

[59] Choudhary, T.; Goodman, D., *Appl. Catal. A Gen.* **2005**, 291 (1-2), 32–36.

[60] An, K.; Alayoglu, S.; Musselwhite, N.; Plamthottam, S.; Melaet, G.; Lindeman, A. E.; Somorjai, G. A., *J. Am. Chem. Soc.* **2013**, 135 (44), 16689–16696.

[61] Fukamori, Y.; König, M.; Yoon, B.; Wang, B.; Esch, F.; Heiz, U.; Landman, U., *ChemCatChem* **2013**, 5 (11), 3330–3341.

[62] Hammer, B.; Nørskov, J. K., *Nature* **1995**, 376 (6537), 238–240.

[63] Mukherjee, S.; Zhou, L.; Goodman, A. M.; Large, N.; Ayala-Orozco, C.; Zhang, Y.; Nordlander, P.; Halas, N. J., *J. Am. Chem. Soc.* **2014**, 136 (1), 64–7.

[64] Dahl, S.; Logadottir, A.; Egeberg, R. C.; Larsen, J. H.; Chorkendorff, I.; Törnqvist, E.; Nørskov, J. K., *Phys. Rev. Lett.* **1999**, 83 (9), 1814–1817.

[65] Neyerlin, K. C.; Gu, W.; Jorne, J.; Gasteiger, H. A., *J. Electrochem. Soc.* **2007**, 154, B631.

[66] Gasteiger, H. A.; Garche, J., *Handb. Heterog. Catal.* **2008**, 3031–3121.

[67] Gorlin, Y.; Jaramillo, T. F., *J. Am. Chem. Soc.* **2010**, 132 (39), 13612–13614.

[68] Schlapbach, L.; Züttel, A., *Nature* **2001**, 414 (6861), 353–358.

[69] Johansson, M.; Johannessen, T.; Jørgensen, J. H.; Chorkendorff, I., *Appl. Surf. Sci.* **2006**, 252, 3673–3685.

[70] Johansson, M.; Lytken, O.; Chorkendorff, I., *J. Chem. Phys.* **2008**, 128 (3), 034706.

[71] Wang, L.; Yang, R. T., *J. Phys. Chem. C* **2008**, 112 (32), 12486–12494.

[72] Yamauchi, M.; Kobayashi, H.; Kitagawa, H., *ChemPhysChem* **2009**, 10 (15), 2566–2576.

[73] Bernasek, S. L.; Siekhaus, W. J.; Somorjai, G. A., *Phys. Rev. Lett.* **1973**, 30 (24), 1202–1204.

[74] Bernasek, S. L.; Somorjai, G. A., *J. Chem. Phys.* **1975**, 62 (8), 3149–3161.

[75] Salmeron, M.; Gale, R. J.; Somorjai, G. A., *J. Chem. Phys.* **1977**, 67 (11), 5324–5334.

[76] Ross, P. N.; Stonehart, P., *J. Res. Inst. Catal. Hokkaido Univ.* **1974**, 22 (1), 22–41.

[77] O'Brien, C. P.; Miller, J. B.; Morreale, B. D.; Gellman, A. J., *J. Phys. Chem. C* **2011**, 24221–24230.

[78] Xu, L.; Ma, Y.; Zhang, Y.; Teng, B.; Jiang, Z.; Huang, W., *Sci. China Chem.* **2011**, 54 (5), 745–755.

[79] Fiordaliso, E.; Murphy, S.; Nielsen, R.; Dahl, S.; Chorkendorff, I., *Surf. Sci.* **2012**, 606 (3-4), 263–272.

[80] Wallin, M.; Grönbeck, H.; Spetz, A. L.; Eriksson, M.; Skoglundh, M., *J. Phys. Chem. B* **2005**, 109 (19), 9581–9588.

[81] Sajiki, H.; Kurita, T.; Esaki, H.; Aoki, F.; Maegawa, T.; Hirota, K., *Org. Lett.* **2004**, 6 (20), 3521–3523.

[82] Keppeler, M.; Roduner, E., *Phys. Chem. Chem. Phys.* **2014**, (111), 11–14.

[83] Engel, T.; Ertl, G., *J. Chem. Phys.* **1978**, 69 (3), 1267–1281.

[84] Berlowitz, P. J.; Peden, C. H. F.; Goodman, D. W., *J. Phys. Chem.* **1988**, 92 (18), 5213–5221.

[85] Bowker, M.; Jones, I. Z.; Bennett, R. A.; Esch, F.; Baraldi, A.; Lizzit, S.; Comelli, G., *Catal. Letters* **1998**, 51 (3-4), 187–190.

[86] Bus, E.; van Bokhoven, J. A., *Phys. Chem. Chem. Phys.* **2007**, 9 (22), 2894–2902.

[87] Olsen, R. A.; Kroes, G. J.; Baerends, E. J., *J. Chem. Phys.* **1999**, 111 (24), 11155–11163.

[88] Skúlason, E.; Faraj, A. A.; Kristinsdóttir, L.; Hussain, J.; Garden, A. L.; Jónsson, H., *Top. Catal.* **2013**, 57 (1-4), 273–281.

[89] Pasteur, A.; Dixon-Warren, S.; Ge, Q.; King, D., *J. Chem. Phys.* **1997**, 106 (21), 8896–8904.

[90] Behafarid, F.; Ono, L. K.; Mostafa, S.; Croy, J. R.; Shafai, G.; Hong, S.; Rahman, T. S.; Bare, S. R.; Roldan Cuenya, B., *Phys. Chem. Chem. Phys.* **2012**, 14, 11766–11779.

[91] Gomez, T.; Florez, E.; Rodriguez, J. A.; Illas, F., *J. Phys. Chem. C* **2011**, 115 (001), 11666–11672.

[92] Yook, S.; Shin, H.; Kim, H.; Choi, M., *ChemCatChem* **2014**, 6 (10), 2836–2842.

[93] Simonsen, S. B.; Chorkendorff, I.; Dahl, S.; Skoglundh, M.; Sehested, J.; Helveg, S., *J. Am. Chem. Soc.* **2010**, 132 (23), 7968–7975.

[94] Simonsen, S. B.; Chorkendorff, I.; Dahl, S.; Skoglundh, M.; Sehested, J.; Helveg, S., *J. Catal.* **2011**, 281 (1), 147–155.

[95] Zhdanov, V. P.; Schweinberger, F. F.; Heiz, U.; Langhammer, C., *Chem. Phys. Lett.* **2015**, 631-632, 21–25.

[96] Wettergren, K.; Schweinberger, F. F.; Deiana, D.; Ridge, C. J.; Crampton, A. S.; Rötzer, M. D.; Hansen, T. W.; Zhdanov, V. P.; Heiz, U.; Langhammer, C., *Nano Lett.* **2014**, 14, 5803–5809.

[97] Fukui, N.; Yasumatsu, H., *Eur. Phys. J. D* **2013**, 67 (4), 81.

[98] Vurens, G. H.; Strongin, D. R.; Salmeron, M.; Somorjai, G. A., *Surf. Sci.* **1988**, 199 (1-2), L387–L393.

[99] van Leerdam, G. C.; Brongersma, H.; Tijburg, I. I. M.; Geus, J. W., *Appl. Surf. Sci.* **1992**, 55, 11–18.

[100] Hohenberg, P.; Kohn, W., *Phys. Rev.* **1964**, 136 (3B), B864–B871.

[101] Kohn, W.; Sham, L., *Phys. Rev.* **1965**, 140 (4A), 1133–1138.

[102] Jørgensen, M., Supported Sub-Nano Catalysts Modeled with Density Functional Theory, Master's thesis, Technical University of Denmark, **2015**.

[103] Mortensen, J. J.; Hansen, L.; Jacobsen, K. W., *Phys. Rev. B* **2005**, 71 (3), 035109.

[104] Bahn, S.; Jacobsen, K. W., *Comput. Sci. Eng.* **2002**, 56–66.

[105] Wellendorff, J.; Lundgaard, K.; Møgelhøj, A.; Petzold, V.; Landis, D.; Nørskov, J. K.; Bligaard, T.; Jacobsen, K. W., *Phys. Rev. B* **2012**, 85 (23), 235149.

[106] Fu, Q.; Wagner, T., *Surf. Sci. Rep.* **2007**, 62 (11), 431–498.

[107] Wang, B.; Yoon, B.; König, M.; Fukamori, Y.; Esch, F.; Heiz, U.; Landman, U., *Nano Lett.* **2012**, 12 (11), 5907–5912.

[108] Ewing, C. S.; Hartmann, M. J.; Martin, K. R.; Musto, A. M.; Padinjarekutt, S. J.; Weiss, E. M.; Veser, G.; McCarthy, J. J.; Johnson, J. K.; Lambrecht, D. S., *J. Phys. Chem. C* **2015**, 119 (5), 2503–2512.

[109] Zhou, C.; Wu, J.; Nie, A.; Forrey, R. C.; Tachibana, A.; Cheng, H., *J. Phys. Chem. C* **2007**, 111 (34), 12773–12778.

[110] Tang, W.; Sanville, E.; Henkelman, G., *J. Phys. Condens. Matter* **2009**, 21 (8), 084204.

[111] Gao, J.; Liu, Q.; Gu, F.; Liu, B.; Zhong, Z.; Su, F., *RSC Adv.* **2015**, 5 (29), 22759–22776.

[112] Kiendl, I.; Klemm, M.; Clemens, A.; Herrman, A., *Fuel* **2014**, 123, 211–217.

[113] Kopyscinski, J.; Seemann, M.; Moergeli, R.; Biollaz, S.; Schildhauer, T., *Appl. Catal. A Gen.* **2013**, 462-463, 150–156.

[114] Laursen, A. B.; Kegnæs, S.; Dahl, S.; Chorkendorff, I., *Energy Environ. Sci.* **2012**, 5 (2), 5577–5591.

[115] Seger, B.; Pedersen, T.; Laursen, A.; Vesborg, P. C. K.; Hansen, O.; Chorkendorff, I., *J. Am. Chem. Soc.* **2013**, 135 (3), 1057–1064.

[116] Vesborg, P. C. K.; Seger, B.; Chorkendorff, I., *J. Phys. Chem. Lett.* **2015**, 6 (6), 951–957.

[117] Sabatier, P.; Senderens, J.-B., *C. R. Acad. Sci. Paris* **1902**, 134, 514–516.

[118] Bligaard, T.; Nørskov, J. K.; Dahl, S.; Matthiesen, J.; Christensen, C. H.; Sehested, J., *J. Catal.* **2004**, 224 (1), 206–217.

[119] Gao, J.; Wang, Y.; Ping, Y.; Hu, D.; Xu, G.; Gu, F.; Su, F., *RSC Adv.* **2012**, 2 (6), 2358–2368.

[120] Wentrcek, P. R.; Wood, B. J.; Wise, H., *J. Catal.* **1976**, 43 (1-3), 363–366.

[121] Nguyen, T.; Wissing, L.; Skjøth-Rasmussen, M., *Catal. Today* **2013**, 215, 233–238.

[122] Rostrup-Nielsen, J.; Pedersen, K.; Sehested, J., *Appl. Catal. A Gen.* **2007**, 330, 134–138.

[123] Vannice, M. A., *J. Catal.* **1975**, 37 (3), 462–473.

[124] Vannice, M., *J. Catal.* **1975**, 37 (3), 449–461.

[125] Andersson, M. P.; Bligaard, T.; Kustov, A. L.; Larsen, K.; Greeley, J.; Johannessen, T.; Christensen, C. H.; Nørskov, J. K., *J. Catal.* **2006**, 239 (2), 501–506.

[126] Chen, X.; Jin, J.; Sha, G.; Li, C.; Zhang, B.; Su, D.; Williams, C. T.; Liang, C., *Catal. Sci. Technol.* **2014**, 4 (1), 53–61.

[127] Tian, D.; Liu, Z.; Li, D.; Shi, H.; Pan, W.; Cheng, Y., *Fuel* **2013**, 104, 224–229.

[128] Bartholomew, C. H.; Pannell, R. B.; Butler, J., *J. Catal.* **1980**, 65, 335–347.

[129] McCarty, J. G.; Wise, H., *J. Catal.* **1979**, 57 (3), 406–416.

[130] Kelley, R.; Goodman, D. W., *Surf. Sci.* **1982**, 123, L743–L749.

[131] Nikolla, E.; Holewinski, A.; Schwank, J.; Linic, S., *J. Am. Chem. Soc.* **2006**, 128 (35), 11354–11355.

[132] Wang, H.; Fang, Y.; Liu, Y.; Bai, X., *J. Nat. Gas Chem.* **2012**, 21 (6), 745–752.

Appendix

H_2/D_2 exchange

Table A.1: Experimental values for XPS data acquisition. Reprinted from [49].

scan type	scan range [eV]	pass energy [eV]	step size [eV]	scans [#]	dwell time [s]
survey	1050 to -5	50	0.5	2	0.5
detailed	100 to 50	25	0.2	10	0.2

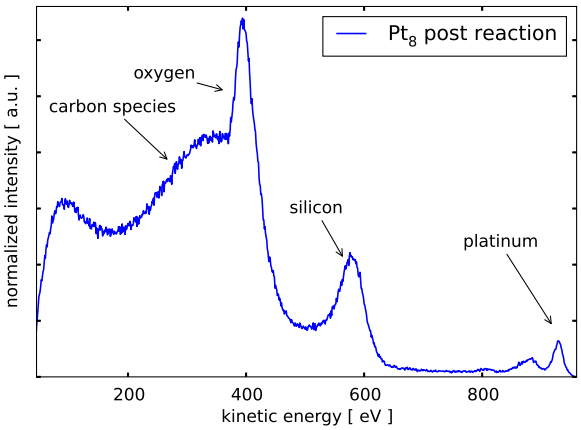

Figure A.1. ISS spectrum of the Pt_8 sample after chemical testing. Reprinted from [49].

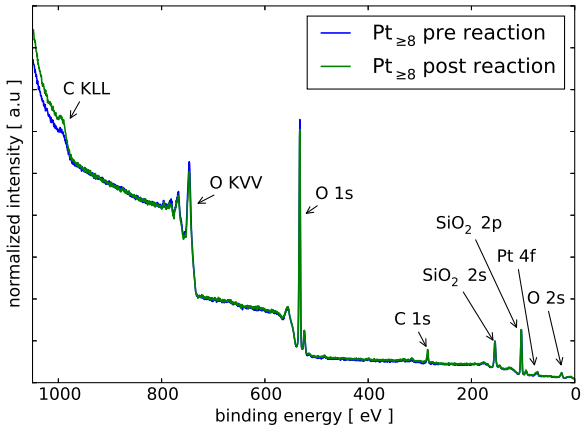

Figure A.2. XPS overview spectra of the $Pt_{\geq 8}$ sample before and after chemical testing. Reprinted from [49].

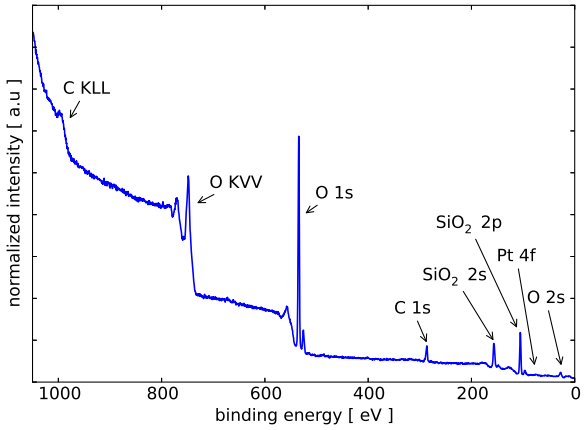

Figure A.3. XPS overview spectrum of the Pt_8 sample after chemical reaction. Reprinted from [49].

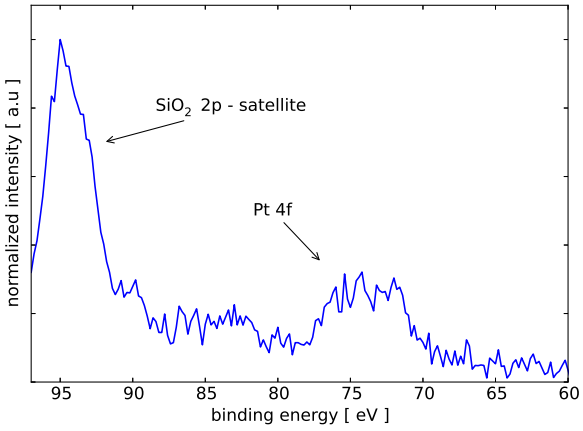

Figure A.4. XPS spectrum of the Pt_8 sample after chemical reaction. The graph is zoomed in on the SiO_2 2p satellite and the Pt 4f doublet. The smaller clusters, compared to the unselected $Pt_{\geq 8}$ sample, result in a very small Pt peak where the doublet is hardly distinguishable. Reprinted from [49].

Appendix

B

Methanation

Table B.1: Overview of $Ni_{75}Fe_{25}$ samples used for methanation.

sample name	particle size [nm]	coverage [%]
MR59	9	10
MR61	7	10
MR52	7	10
MR46	7	10
MR60	5	10
MR34	5	10
MR24	5	10
MR56	3.5	10

Table B.2: Parameters used for XPS measurements of $Ni_{75}Fe_{25}$ samples.

spectrum name	scan range [eV]	pass energy [eV]	step size [eV]	scans [#]	dwell time [s]
survey	1050.0 to -5.0	50.0	0.5	2	0.200
Ni $2p_{3/2}$	872.0 to 846.0	50.0	0.100	15	0.200
Fe $2p_{3/2}$	727.0 to 700.0	50.0	0.100	20	0.200
O 1s	540.0 to 525.0	50.0	0.100	5	0.200
C 1s	294.0 to 280.0	50.0	0.100	10	0.200
Si 2s	165.0 to 145.0	50.0	0.100	5	0.200
Si 2p	111.0 to 98.0	50.0	0.100	5	0.200

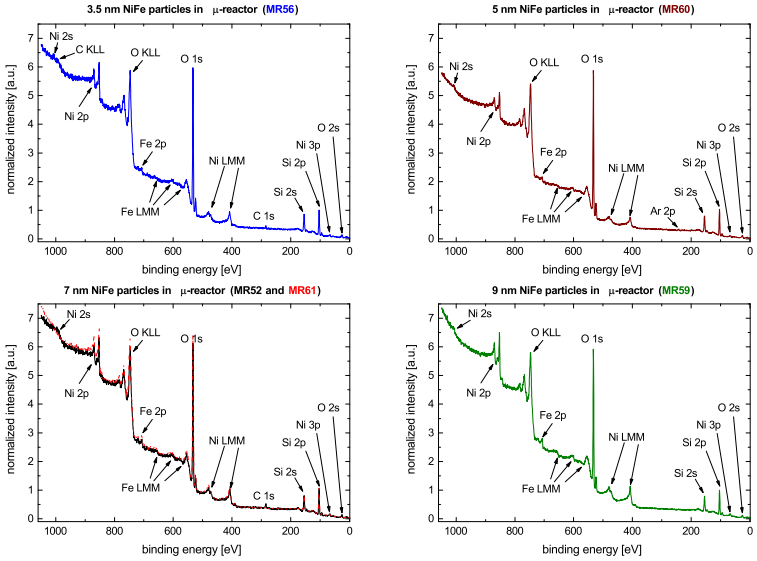

Figure B.1. XPS overview spectra of $Ni_{75}Fe_{25}$ samples. All spectra are normalized to the SiO_2 2p peak area and shifted to fit the SiO_2 2p peak at 103.5 eV. Figure by Béla Sebök.

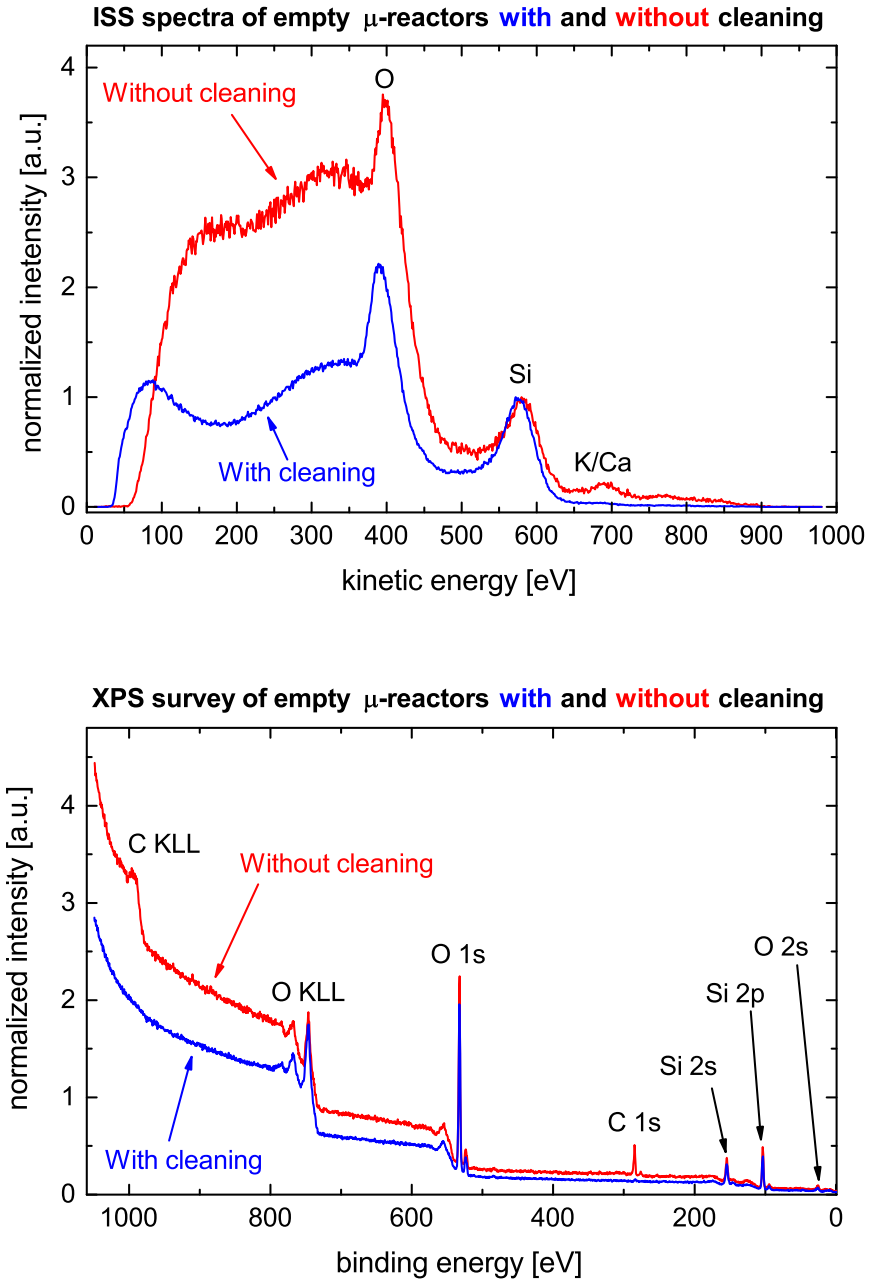

Figure B.2. XPS and ISS spectra of a cleaned and un-cleaned reactor. Figure by Béla Sebök.

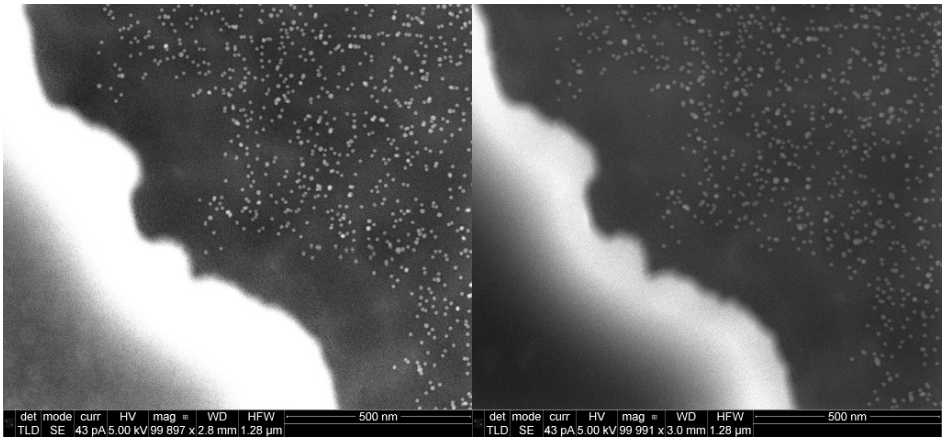

Figure B.3. Identical location SEM of pillar edge of a 9 nm $Ni_{75}Fe_{25}$ sample before (left) and after (right) chemical testing. The rough edge of pillar is seen in the bottom left corner of each image. Image by Elisabetta Maria Fiordaliso.

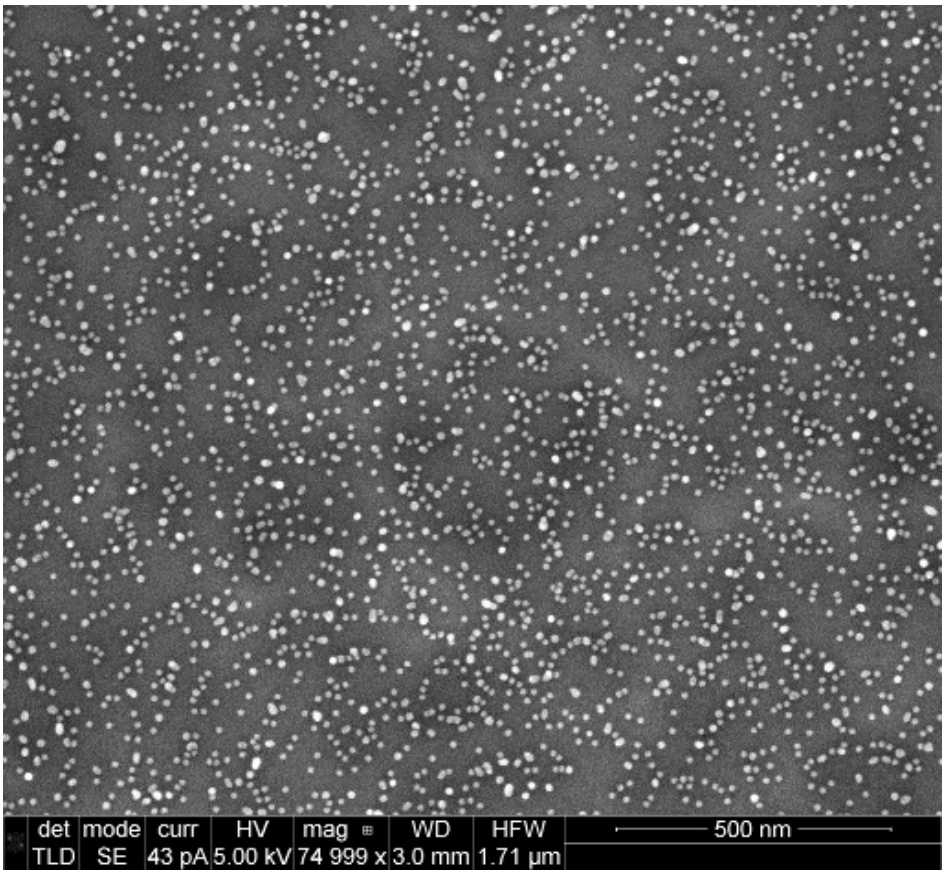

Figure B.4. SEM image of an area of a 9 nm $Ni_{75}Fe_{25}$ sample, not imaged prior to chemical activity testing. Image by Elisabetta Maria Fiordaliso.

Journal Name

ARTICLE TYPE

Cite this: DOI: 10.1039/xxxxxxxxxx

H_2/D_2 exchange reaction on mono-disperse Pt clusters: Enhanced activity from minute O_2 concentrations†

Jakob Nordheim Riedel,[a] Marian David Rötzer,[b] Mikkel Jørgensen,[cd] Ulrik Grønbjerg Vej-Hansen,[ac] Thomas Pedersen,[e] Béla Sebök,[a] Florian Frank Schweinberger,[b] Peter Christian Kjærgaard Vesborg,[a] Ole Hansen,[e] Jakob Schiøtz,[ac] Ulrich Heiz,[b] and Ib Chorkendorff*[a]

Received Date
Accepted Date

DOI: 10.1039/xxxxxxxxxx

www.rsc.org/journalname

The H_2/D_2 exchange reaction was studied on mono-dispersed Pt_8 clusters in a μ-reactor. The chemical activity was studied at temperatures varying from room temperature to 180 °C, using mass spectrometry. It was found that minute amounts of O_2 in the gas stream increased the chemical activity significantly. XPS and ISS before and after reaction suggests little or no sintering during reaction. A reaction pathway is suggested based on DFT. H_2 desorption is identified as the rate limiting step and O_2 is confirmed as the source of the increased activity. The binding energy of platinum atoms in a SiO_2 supported Pt_8 cluster is found to be comparable to inter atomic binding energies of bulk platinum, underlining the stability of the model system.

Introduction

Experiments aiming to enhance the fundamental understanding of chemical reactions on surfaces require well defined model catalyst systems and simple reactions. Size selected sub-nanometer metal clusters on a uniform support are well defined model systems that have attracted significant attention for their unique chemical properties.[1–4] For example; bulk gold is noble and does not dissociate H_2[5] while gold nanoparticles are active for H_2 dissociation[4] and photo-dissociation.[6]

The dissociation of H_2 is an important elementary step in many industrial reactions[7] including hydrogen oxidation in fuel cells,[8,9] and has been studied for hydrogen storage,[10–14] but is not well understood on metal clusters at ambient pressures. Single crystal studies prove that hydrogen dissociates on high Miller index platinum surfaces[15–17] and that adsorption-dissociation is rate controlling for the H_2/D_2 exchange reaction.[18,19] Strong coverage dependent adsorption suggests that repulsive adsorbate interaction decreases adsorption energy and desorption activation energy of hydrogen on Pt(111).[20] On a nanoparticle scale H_2/D_2 exchange reaction is only weakly dependent on size[21] and OH groups form on, or around, the SiO_2 supported platinum particles.[22] The OH group is believed to be directly involved in the H_2/D_2 exchange reaction.[23] At an even smaller size regime Pt_{13} clusters can accommodate 32 hydrogen atoms at 200 mbar[24] proving large enough to facilitate enough reactants for random recombination of surface species. This study aims to clarify the reaction mechanism on Pt clusters supported on SiO_2 and how it can be influenced by adding minute amounts of O_2 to a well defined model system. Cluster stability is also addressed using ISS, XPS, and DFT. Platinum nanoparticles sinter primarily by Ostwald ripening.[25–29] The process can be suppressed by a narrow particle size distribution. DFT simulations on the mono-disperse Pt_8 sample was also used to support stability. The model system is studied using μ-reactors as graphically shown in figure 1.

Methods

μ-reactor

The μ-reactor constitutes an etched silicon chip sealed with a pyrex lid using anodic bonding.[30,31] While small (16×20 mm) and having a cylindrical reactor volume with a diameter of 1 cm and depth of 3 μm the design allows heterogeneous gas-phase catalysis on minute amounts of catalyst at pressures from

[a] DNRF Center for Individual Nanoparticle Functionality (CINF), Department of Physics, Technical University of Denmark, DK-2800 Kgs. Lyngby, Denmark; E-mail: ibchork@fysik.dtu.dk.
[b] Chair of Physical Chemistry, Catalysis Research Center and Chemistry Department, Technische Universität München, Lichtenbergstr. 4, 85748 Garching, Germany.
[c] Center for Atomic-scale Materials Design (CAMD), Department of Physics, Technical University of Denmark, DK-2800 Kgs. Lyngby, Denmark.
[d] Department of Applied Physics and Competence Centre for Catalysis, Chalmers University of Technology, Göteborg, Sweden
[e] Department of Micro- and Nanotechnology, Technical University of Denmark, DK-2800 Kgs. Lyngby, Denmark.
† Electronic Supplementary Information (ESI) available: [details of any supplementary information available should be included here]. See DOI: 10.1039/b000000x/

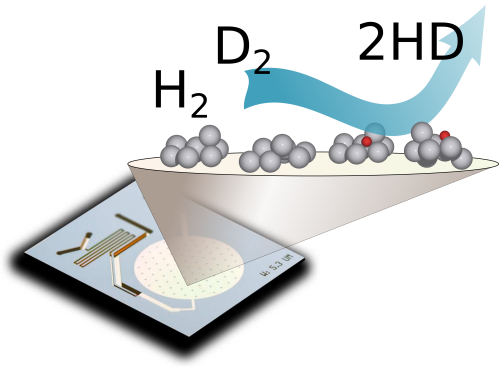

Fig. 1 Graphical representation of H_2/D_2 exchange reaction being facilitated on clusters with an added oxygen atom (red). The experiments are carried out in a μ-reactor.

$0.1 - 2.5$ bar. Two inlet channels allow mixing of reactant gases. One outlet bypasses the reactor volume and is used to control the pressure in the reactor while a second outlet leads the products and unconverted reactants from the reactor volume to an ultra high vacuum (UHV) chamber where the gases can be continuously analysed with a quadrupole mass spectrometer (QMS) (Balzers QMS 125) and logged together with a time resolved temperature measurement.

For catalyst characterization after chemical testing it was necessary to remove the reactor lid. A diamond saw was used for cutting pyrex and silicon, but to prevent contaminating the surface with cooling water a simple method was used. Grooves were cut in a square pattern above the reactor volume leaving $\sim 35\,\mu$m thick pyrex. A piece of copper was glued to the square cut-out and the reactor lid was broken off. This left small Pyrex shards on the catalyst surface, but prevented contaminations from cooling water from the diamond saw.

Cluster synthesis

The clusters were deposited on the μ-reactors described above using a high frequency laser ablation cluster source and a transfer chamber, described in detail elsewhere.[32–34] In short, the beam of a diode pumped Nd:YAG laser (InnoLas, Germany; DPSS Spitlite, 100 Hz, 70 mJ at 532 nm) was focused onto a rotating (1 Hz) metal target (99.99 % Pt, Goodfellow, USA). The resulting plasma was cooled via a delayed helium (He 6.0, Westfalen, Germany) gas pulse and afterwards an adiabatic expansion of the helium platinum vapour through a nozzle into the vacuum. An octupole and ion lenses then guided the cluster beam along the axis of the differentially pumped vacuum. In a quadrupole bender unit the clusters cations were separated from the neutral ones; the deflector unit was operated in such way, that positively charged clusters were focused into a QMS (ABB Extrel Merlin, U.S.A.) with a mass limit of 16,000 u where mass selection down to a single cluster size is achieved. The QMS was operated and optimized for highest transmission while ensuring size selection down to a single mass. A mass scan of the cluster current is show in figure S1 of the ESI. Beside the selection of only Pt_8 clusters (1560 u) the QMS was operated as a high-pass mass filter by means of only using the radio frequency (RF only mode) of the QMS. As a consequence, unselected clusters with a tunable minimum size (in the presented study 8 atoms, short $Pt_{\geq 8}$) were generated. After size selection the cluster beam passed through an aperture and was focused onto the substrate (deposition diameter of 10 mm, corresponding to the reaction zone of the μ-reactor) while assuring soft-landing conditions, i.e. deposition energies lower than 1 eV per cluster atom.[35,36] Recording the discharge current on the support (coverage reported in the unit charges per area: e nm^{-2} - assuming single charged clusters) over the course of the deposition period, the coverage was measured and kept at a value of 0.023 e nm^{-2} for all prepared samples. The sample was then transferred to ambient conditions for subsequent anodic bonding and experiments.

Spectroscopic characterisation

Ion scattering spectroscopy (ISS) and X-ray photo-electron spectroscopy (XPS) were performed in a UHV chamber (Omicron, Multiscan Lab) with a base pressure of 1×10^{-11} mbar. ISS was measured at a constant He pressure of 1×10^{-7} mbar and a primary He^+ energy of 1000 eV. A magnesium anode was used to generate X-rays for XPS. Further details are given in the ESI.

Chemical activity procedure

H_2/D_2 exchange reaction was performed by dosing a continuous flow of H_2 (H2 6.0, AGA, Denmark), D_2 (D2 N30, Alpha Gas, France), and Ar (Ar 6.0, AGA, Denmark) through the μ-reactor in a 4:4:1.5 ratio, respectively. Gas products were detected by a QMS and plots show HD turn over frequency (TOF) as function of temperature. Since the $m/z = 3$ background signal was dominated by the H_2/D_2 gas stream, a background proportional to the $m/z = 4$ signal was subtracted from the $m/z = 3$ signal. The TOF was calculated by assuming that 4:9.5 of the total flow is HD at full conversion at a pure H_2/D_2/Ar gas mixture and relating that to a gas flow.[37] This flow was divided by the number of platinum surface atoms in the reactor containing Pt_8 clusters. Assuming one surface atom equals one surface site this resulted in a TOF.

The reactor was pumped down to $\sim 2 \times 10^{-3}$ mbar before the catalyst was oxidized in 1 bar of O_2 for 0.5 h and cooled to room temperature (RT) in oxygen before pumping out. The reactor and gas lines were then flooded with Ar at 0.5 bar and pumped out twice. A gas flow composed of 4:4:1.5 of H_2, D_2, and Ar, respectively, was started. The reactor was kept at 100 °C for 4 h while the gas flows stabilized and residual oxygen in the reactor was reacted off. To determine the activity of reduced clusters the reactor was cooled to RT and heated using three subsequent heating ramps to 180 °C and back to RT at 2 °C min^{-1}. The transition to an oxygen containing gas stream was done at 100 °C where the Ar flow was changed from 1.5 to 1.45 ml min^{-1} while a 5000 ppm O_2 in Ar (5000 ppm O_2 in Ar, AGA, Denmark) was set to 0.05 ml min^{-1} corresponding to 26 ppm O_2 of the total H_2/D_2/Ar/O_2 gas stream. When flows and catalyst activity was stabilized the sample was

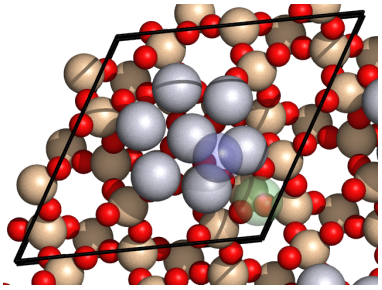

Fig. 2 Initial configurations of the Pt_8 cluster before relaxation. Seven atoms form a basal plane; the eighth atom can either be on top of the basal plane (shown in transparent blue) or as an extension of the basal plane (shown in transparent green). In either case there are six different sites. The black box denotes the computational unit cell. Platinum atoms are grey, silicon atoms are golden and oxygen atoms are red.

cooled to RT. Testing the activity in the new gas flow was done by heating to 120 °C and back to RT at 2 °C min^{-1} with three subsequent heating ramps.

DFT calculations

In order to investigate the activity and stability of the Pt_8 clusters, density functional theory (DFT)[38,39] calculations were used to find their adhesion energy and the dissociative adsorption energies of hydrogen with and without co-adsorbed oxygen, in the form of OH. The adsorption energies were corrected for the change in zero-point energies, by calculation of the vibrational spectra. The silica substrate was modelled as a (0001) surface of α-quartz without oxygen vacancies.[40]

The DFT calculations were made with the GPAW software[41] using the ASE framework[42] and the BEEF-vdW exchange-correlation functional.[43] BEEF is short for Bayesian Error Estimation Functional, and includes capabilities for estimating the error on calculated energies.[43] Atomic positions were optimized until the forces were less than 0.05 eV/Å in any cartesian coordinate. The clusters were set up using a 7-atom basal plane,[44,45] and then investigated 6 reasonable sites for the 8th atom, with examples shown in figure 2. Note that the clusters change their shape rather dramatically upon relaxation, and the 6 initial configurations should therefore be viewed as a distribution of initial conditions and not as a guess of the final structure. The relaxed configurations are shown in figure S8 in the ESI. Due to the size of these unit cells it was sufficient to sample the Brillouin Zone with a 3x3x1 k-point-grid.[46] The slab was separated from the edge of the computational box by 6 Å of vacuum on each side in the non-periodic direction. For calculations involving hydrogen, oxygen atoms in SiO_2 not covered by Pt were passivated with hydrogen.

In order to determine the effect of oxygen on the cluster morphology, the stability of adsorbed oxygen on the most stable cluster morphology found in vacuum was investigated. Oxygen was adsorbed in the different available sites on the lowest-energy cluster found previously, and all atomic positions in the cluster were allowed to relax again.

Results and discussion

Analysis of the chemical activity of the catalysts is conducted in the μ-reactor while characterization before and after reaction is performed using ISS and XPS. Samples are characterized to determine the stability of the catalyst. Ripening processes of clusters have been found to vary with both metal and support.[28] However, mono-disperse clusters have a unique ability to suppress Ostwald ripening.[26,27,29,34,47] To assure the stability of the Pt_8 sample during reaction, an unselected $Pt_{\geq 8}$ sample was given the same chemical and thermal treatment and examined for signs of sintering using ISS and XPS.

Ion scattering spectroscopy

ISS is strictly surface sensitive and only probes the outermost atomic layer. If a catalyst sinters, the total catalyst surface area would decrease while the bulk increases and cause the cluster related ISS signal to decrease.[48–50]

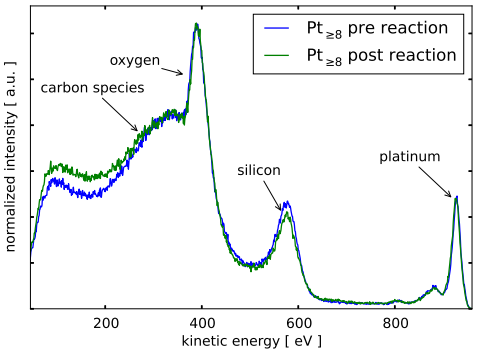

Fig. 3 ISS of $Pt_{\geq 8}$ prior to anodic bonding of lid and testing chemical activity (blue) and after chemical reaction (green) normalized to the oxygen peak. Both graphs show clear peaks from platinum at ∼927 eV. The two small peaks on the low energy side of platinum are identified as minute contaminants. The platinum peaks show no traceable change in intensity indicating insignificant sintering.

To determine stability of the catalyst, the $Pt_{\geq 8}$ sample is characterised with ISS before and after testing. This sample is selected for its inhomogeneous size distribution that makes it more prone to sintering.[26,27,29,34,47] Figure 3 shows the ISS signal normalized to the oxygen peak as function of kinetic energy before (blue) and after (green) reaction. Most noticeably the two curves show comparable features. The platinum and silicon peaks at ∼ 927 eV and ∼ 590 eV respectively are almost identical in the two measurements, indicating little or no sintering during reaction. Since the $Pt_{\geq 8}$ sample is more prone to sintering, the mono-disperse Pt_8 sample is therefore expected to be stable under reaction conditions. The peak at ∼ 391 eV is identified as oxygen originating from the SiO_2 substrate and contamination from exposure to air. Below this energy is a large broad feature coming from various carbon species, also from exposure to air. At 800 to 900 eV are two small features that could not be identified. These contami-

nants are in very small quantities and are therefore negligible.

X-ray photoelectron spectroscopy

XPS spectra of the $Pt_{\geq 8}$ sample taken before and after testing of chemical activity are shown in figure 4 with a zoom in on the Pt 4f doublet and SiO_2 2p satellite peaks. The SiO_2 2p peaks are omitted in favour of the satellite peaks because the signal intensity match better that of the Pt 4f doublet. Red and grey bars indicate position and relative height of $4f_{5/2}$ and $4f_{7/2}$ peaks of metallic platinum and SiO_2 2p satellite peaks from $K\alpha_3$ and $K\alpha_4$ lines of the magnesium anode, respectively. Both curves were normalised to the SiO_2 satellite peaks and shifted in energy so the carbon 1s peak is at 284.6 eV. The overall intensity of the spectrum after reaction is higher than the spectrum prior to reaction, giving rise to a better signal to noise ratio in the spectrum after reaction. Prior to each spectrum the sample is transported under atmospheric conditions. The shift of the $4f_{5/2}$ and $4f_{7/2}$ peaks to higher binding energies can be explained by a final state effect or a partial oxidation of the cluster. The two spectra do not differ significantly and the integrated peak area ratio between platinum and the silicon satellite is 1.17 before reaction and 1.58 after. Finding the exact same spot on the reactor after chemical testing is impractical and small changes in signal intensity is to be expected. Given the experimental uncertainties this change is insignificant since the spot in the reactor being measured is likely slightly different in the two measurements. The relatively stable $Pt_{\geq 8}$ sample suggests that the mono-disperse Pt_8 sample will be stable during reaction conditions.

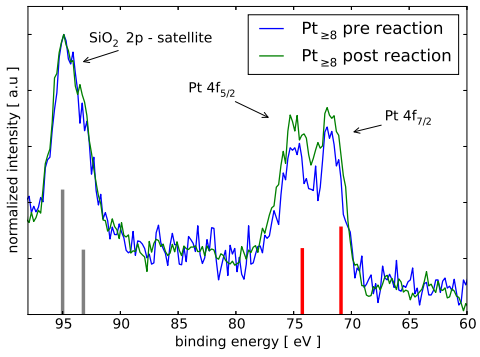

Fig. 4 XPS spectra of $Pt_{\geq 8}$ before (blue) and after (green) chemical activity testing. Red bars show position and relative height of metallic platinum $4f_{5/2}$ and $4f_{7/2}$. The grey bars indicate position and relative height of the SiO_2 2p satellite peaks from $K\alpha_3$ and $K\alpha_4$ of the magnesium anode. Similarities between the two curves further emphasize the cluster stability. The binding energies are shifted to fit the carbon 1s peak to 284.6 eV and normalized to the SiO_2 satellite peaks. Fitted parameters to the peaks are shown in table S2 together with overview spectra shown in figure S3 of the ESI.

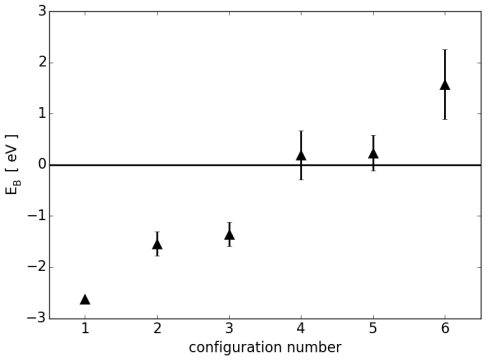

Fig. 5 Binding energy of the Pt_8 clusters on SiO_2, with the Pt referenced to bulk Pt. Negative values indicate that the clusters are more stable than Pt in the bulk form. The atomic configurations are shown in figure S8 in the ESI, using the same numbering. Error bars are from the BEEF-vdW exchange-correlation functional.

DFT structure and stability

Figure 5 shows the binding energy of the investigated atomic configurations with the chemical potential of bulk platinum as the reference. It shows that the three configurations with the lowest energy are found to be stable with regard to this reference, meaning they have lower energy per atom than pure bulk platinum. This is surprising given the very open structure of these clusters, and demonstrates that there is a very strong interaction between the clusters and the support. This very strong binding to the support is consistent with studies in the literature on Pt_{13} clusters on amorphous silicon.[51] These very strong bindings also indicate that sintering is unfavourable for these clusters, in agreement with the experimental observations.

The adsorption energy of oxygen on the lowest-energy cluster is also calculated, and finds that oxygen binds strongly to the cluster, with at least 1.0 eV in all investigated sites. This indicates some level of oxygen coverage on the clusters if even small amounts of oxygen is available in the system. The adsorption energies are shown in figure S9 in the ESI.

Chemical activity

The isotopic exchange rate on a Pt_8 cluster sample is shown in figure 6a. Three red curves show activity during pure $H_2/D_2/Ar$ dosage with arrows indicating the direction of the temperature ramp. Highly reproducible data shows full conversion (i.e. the equilibrium gas mixture is obtained) at $\sim 120\,^{\circ}C$. A small hysteresis effect causes slightly higher activity during cooling. This is likely due to small temperature gradients in the reactor. The decrease in HD TOF at full conversion is due to the capillary outlet of the reactor: with increasing temperature the flow through the reactor decreases, causing the TOF to decrease.[37] The green curves show increased activity as a result of the 26 ppm O_2 dosage, proving a dramatic change of the catalyst performance. In the presence of oxygen, full conversion is reached already at $\sim 70\,^{\circ}C$

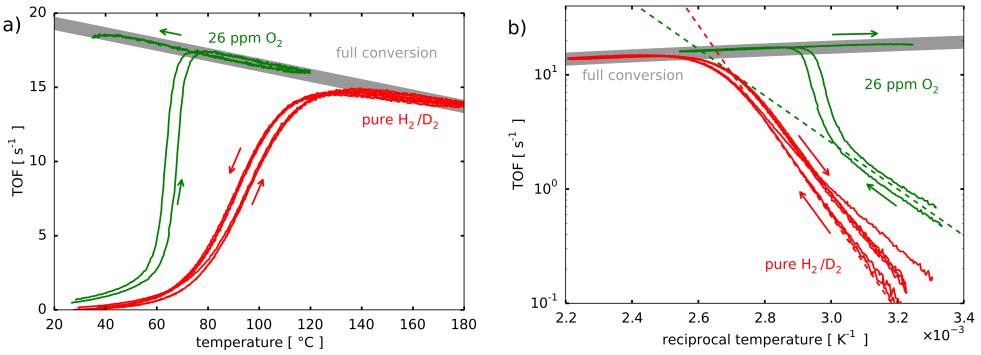

Fig. 6 Isotopic exchange rate for a Pt_8 sample a) as a function of temperature and b) as an Arrhenius plot. The red curves show three subsequent measurements of H_2/D_2 exchange reaction with no O_2 present. Dosage of 26 ppm O_2 resulted in the two green curves with significantly higher activity and a considerable hysteresis that keeps the catalyst at full conversion until ∼45 °C. Arrows indicate the direction of the temperature ramp and the dashed lines in b) show a fit to the linear part of the activity while ramping up the temperature. Apparent activation energy for reduced clusters is 0.83 eV while oxidized clusters have 0.40 eV. The grey areas indicate full conversion.

and a clear hysteresis keeps the catalyst at full conversion during gradual cooling to RT. The pronounced hysteresis and an activity deviating from the initial Arrhenius behaviour shows that the catalyst reaches a state of enhanced activity. Dosage of minute amounts of O_2 causes the HD production to increase with approximately one order of magnitude at 70 °C. Since the reactants have the same free energy as the product, back reaction will be considerable close to full conversion. From this it is clear that oxygen facilitates the reaction. Figure 6b shows an Arrhenius plot of the same data with dashed lines showing a fit to the linear part of the activity while ramping up the temperature. Apparent activation energy for reduced clusters is 0.83 eV while oxidized clusters have an apparent activation energy of 0.40 eV. The corresponding chemical activity and Arrhenius plots for the $Pt_{\geq 8}$ sample are shown in figure S5 in ESI. Adding oxygen to the gas stream also increases the activity of the $Pt_{\geq 8}$ sample, indicating a trend that applies to platinum clusters larger than eight atoms. Signals from other m/z ratios during reaction of the Pt_8 sample are shown in figure S6 and S7 of the ESI. Forming of H_2O, HDO and D_2O during O_2 dosage is to be expected.[52] However, both O_2 ($m/z = 32$) and HDO ($m/z = 19$) signals are below the detection limit. The $m/z = 20$ signal is dominated by doubly ionized Ar and does not provide information on D_2O formation. The H_2O signal ($m/z = 18$) is dominated by water desorbing from the gas handling system and can not be interpreted as relating to the catalytic activity. If H_2O, HDO and D_2O formation is involved in the HD formation it was not detectable in the QMS. ISS and XPS spectra of the Pt_8 sample after reaction are shown in figure S2 and S4 of the ESI, respectively.

Figure 7 shows the HD TOF of the Pt_8 sample at a constant temperature of 100 °C throughout the measurement. A pure $H_2/D_2/Ar$ mixture is dosed during the first four hours. At this point in time 26 ppm O_2 is dosed and the activity rapidly increases to full conversion. This corroborates the profound effects of oxygen on the catalyst performance.

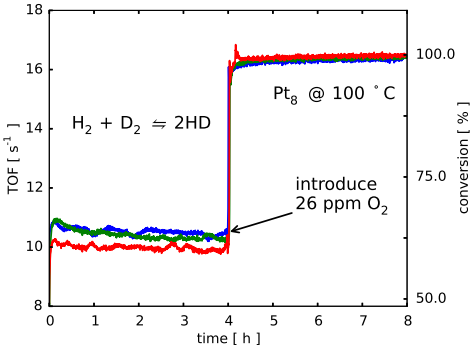

Fig. 7 Three examples of HD TOF during reaction of equal flows of H_2 and D_2 at 100 °C on the Pt_8 sample. At 4 h 26 ppm of O_2 is added to the gas flow. This increases the catalysts activity to a stable plateau at full conversion.

Activation energies reported in literature vary significantly. Table 1 shows activation and adsorption energies on varying model systems measured in experiments or calculated using DFT. The present study demonstrates the profound effect of small oxygen contaminations as a plausible explanation to the large variation of experimental activation energies reported in literature, since O_2 below the detection limit of most experimental set-ups clearly affects the catalyst dramatically.

Activity estimate by DFT

The influence of oxygen on H_2 dissociation activity was investigated through the use of hydrogen adsorption as a descriptor. The dissociation of hydrogen was found to be barrierless on some sites on these clusters, in agreement with literature,[58] thus it is

Table 1 Activation and adsorption energies reported in literature on selected model systems. The method of investigation, i.e. experimental or DFT, is stated together with the reference.

system	E_{act}/eV	E_{ads}/eV	method	ref.
Pt(111)	$0.23-0.026^a$		exp.	16
Pt film	0.22		exp.	12
	$0.22-0.28^b$		exp.	21
Pt wire	0.11		exp.	18
2 nm Pt/SiO_2		0.93	exp.	53
Pt_8/SiO_2	0.83		exp.	present
Pt_8O_x/SiO_2	0.40		exp.	present
Pt(111)	$0.0-0.42^c$		DFT	54
	0.5		DFT	55
Pt(100)	0.8		DFT	55
	0.0		DFT	56
Pt_{22}/Al_2O_3		$0.42-0.62^d$	DFT	44
Pt_{44}/Al_2O_3		$0.47-0.61^d$	DFT	44
Pt_4/TiC(001)	1.16	0.87	DFT	57
Pt_8/SiO_2		$0.13-1.35$	DFT	present
Pt_8O/SiO_2		$0.066-0.89$	DFT	present

[a] Temperature dependent activation energy
[b] Varying with film thickness
[c] Dependent on adsorption site
[d] Energies vary with coverage

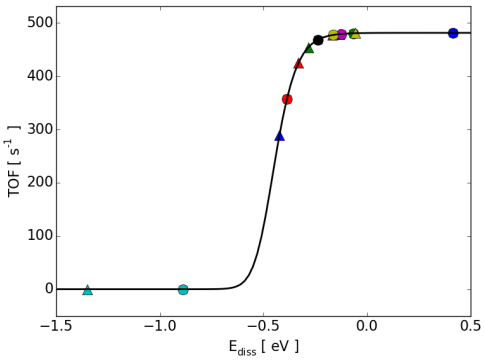

Fig. 8 Calculated activity for hydrogen dissociation for different site combinations on both a bare and oxidized Pt_8 cluster at 1 ML H coverage. Markers with the same colour correspond to the same site combination, with triangles denoting the bare cluster and the circles the oxidized cluster. Figure S8 shows the hydrogen dissociation sites and numerical values for the data points can be found in table S3 in the ESI. The solid line is the theoretical model of activity as a function of hydrogen desorption energy.

assumed that hydrogen dissociation is barrierless on all cluster sites for the purpose of estimating the rate. This means that desorption is the rate-limiting step for the H_2/D_2 exchange reaction. Assuming that diffusion is faster than desorption, the desorption energy equals the adsorption energy and the adsorption is without a barrier. Based on this, the activity is calculated with Transition State Theory, using the expression in equation (1), where the dependence on the dissociative adsorption energy of H_2 is shown explicitly.

$$r = \left(\frac{\sqrt{K}}{1+\sqrt{K}}\right)^2 \frac{k_B T}{\sqrt{2\pi M_{H_2} k_B T}} \exp\left(\frac{S_{gas}}{k_B}\right) \exp\left(\frac{-E_{diss}}{k_B T}\right) \quad (1)$$

$$K = \exp\left(\frac{S_{surf-vib} - S_{gas}}{k_B}\right) \exp\left(\frac{E_{diss}}{k_B T}\right)$$

Here r is the calculated rate, K is the calculated equilibrium constant for the $H_2(gas) \rightleftharpoons 2H(ads)$ reaction, k_B is the Boltzmann constant, T is the temperature, M_{H_2} is the mass of H_2, S_{gas} is the entropy of H_2 in the gas phase, E_{diss} is the dissociative chemisorption energy of H_2 and $S_{surf-vib}$ is the entropy of the vibrations of adsorbed H.[59]

Focus was put on the cluster with the lowest energy, as it is computationally not practical to investigate these effects for a full ensemble of structures. Figure 8 shows the dissociative hydrogen adsorption energy on a cluster with 1 monolayer (ML) of hydrogen, and corresponding calculated activity, for the lowest energy cluster with and without adsorbed oxygen. Note that one data point has a positive desorption energy and is therefore not physical.

The activity for hydrogen dissociation is very sensitive to the adsorption energy in this interval, with the TOF changing from 0 to 500 s^{-1} over a range of 0.5 eV. Furthermore, the expression for the activity is only an approximation, meaning that there is some uncertainty in the horizontal placement of the black curve in figure 8. In many cases, it was found that oxygen lowers the adsorption strength of hydrogen at nearby sites, lowering the barrier for desorption and thereby increasing the rate of H_2 dissociation and recombination. Due to the sensitivity discussed above, even small changes in the desorption energy can lead to substantial increases in activity, and this could be the reason for the observed increase in H_2/D_2 exchange rate under the influence of minute amounts of oxygen.

A Bader charge analysis was used to further analyse the change in activity of this system.[60] This is a method to assign the spatial distribution of charge in the system to specific atoms, indicating whether individual atoms are approximately neutral or charged. The results of this are shown in figure 9 for the lowest energy cluster with and without adsorbed OH. It shows a significant amount of charge transfer between oxygen in SiO_2 and Pt, which could help explain the large adhesion energy. An increase of 0.3 e was also observed in the overall charge of the cluster upon adsorption of OH, which is probably part of the reason for the change in the adsorption energy of hydrogen upon adsorption of OH, consistent with literature.[51]

As the dissociation of hydrogen is barrierless on Pt, the rate is determined by the desorption energy, i.e., the rate-limiting step is desorption of H_2. It is therefore reasonable to assume that adsorption of oxygen on the clusters weakens the adsorption of hydrogen, giving a large increase in the rate due to the exponential dependence of the rate on the desorption energy.

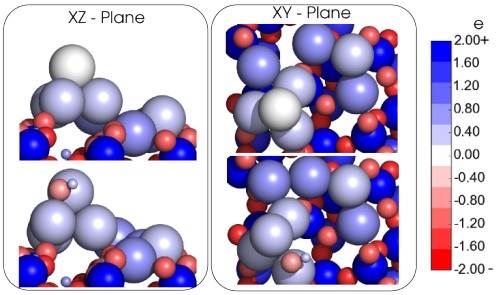

Fig. 9 Bader charge analysis of the lowest energy cluster without (upper panels) and with (lower panels) adsorbed OH. Blue indicates positive and red indicates negative charge. The colour scale is saturated at ±2e in order to better show the variation among the Pt atoms.

Conclusion

Hydrogen dissociation on mono-dispersed platinum clusters was studied using the H_2/D_2 exchange reaction. μ-reactors were used to test reaction rates at 1 bar of pressure and varying temperature. The effects of minute amounts of oxygen in the gas stream under ambient pressures show a significant improvement in reaction rate, at some temperatures up to one order of magnitude. A substantial decrease in apparent activation energy from 0.83 eV to 0.40 eV arose from the oxidation of the clusters. The reaction mechanism was examined by DFT analysis and reaction rate theory. A single oxygen atom on a Pt_8 cluster shows a remarkable influence on morphology and chemical properties of the cluster. This emphasizes the impact oxygen has on performance of the model catalyst. The unselected platinum catalyst also showed a remarkable increase in HD formation when oxygen was added to the gas stream. This suggests that the phenomenon is present also on platinum clusters larger than eight atoms.

The stability of the system was examined by both ISS and XPS on a platinum cluster sample with a significant size distribution before and after chemical reaction. No significant changes in spectra show that little or no sintering of the unselected clusters occurred under reaction conditions, proving that the mass selected samples are stable. This was further supported by DFT calculations that reveal a strong binding of the platinum atoms to the substrate.

Activation energies reported in literature vary significantly. In this paper, it is proven that minute amounts of oxygen present in the system can dramatically change the results of experiments. The presented results provide further insights to more complex reactions that rely on atomic hydrogen as a co-reactant.

Acknowledgements

For funding of this work we gratefully acknowledge The Danish National Research Foundation's Center for Individual Nanoparticle Functionality (DNRF54), the Danish Council for Independent Research's project DynCat (DFF), the European Union's Seventh Framework Programme (FP7/2007-2013) under grant agreement n° 607417 (Catsense), and the DFG Project (He3454/23-1).

References

1 U. Heiz, A. Sanchez, S. Abbet and W.-D. Schneider, *J. Am. Chem. Soc.*, 1999, **121**, 3214–3217.
2 A. Sanchez, S. Abbet, U. Heiz, W.-D. Schneider, H. Häkkinen, R. N. Barnett and U. Landman, *J. Phys. Chem.*, 1999, **103**, 9573–9578.
3 S. Abbet, A. Sanchez, U. Heiz, W.-D. Schneider, A. M. Ferrari, G. Pacchioni and N. Rösch, *J. Am. Chem. Soc.*, 2000, **122**, 3453–3457.
4 T. Fujitani, I. Nakamura, T. Akita, M. Okumura and M. Haruta, *Angew. Chemie - Int. Ed.*, 2009, **48**, 9515–9518.
5 B. Hammer and J. K. Nørskov, *Nature*, 1995, **376**, 238–240.
6 S. Mukherjee, L. Zhou, A. M. Goodman, N. Large, C. Ayala-Orozco, Y. Zhang, P. Nordlander and N. J. Halas, *J. Am. Chem. Soc.*, 2014, **136**, 64–7.
7 K. Honkala, A. Hellman, I. Remediakis, A. Logadottir, A. Carlsson, S. Dahl, C. Christensen and J. K. Nørskov, *Science (80-.).*, 2005, **307**, 555–558.
8 H. A. Gasteiger and J. Garche, *Handb. Heterog. Catal.*, 2008, 3031–3121.
9 K. C. Neyerlin, W. Gu, J. Jorne and H. A. Gasteiger, *J. Electrochem. Soc.*, 2007, **154**, B631.
10 L. Schlapbach and A. Züttel, *Nature*, 2001, **414**, 353–358.
11 M. Johansson, T. Johannessen, J. H. Jørgensen and I. Chorkendorff, *Appl. Surf. Sci.*, 2006, **252**, 3673–3685.
12 M. Johansson, O. Lytken and I. Chorkendorff, *J. Chem. Phys.*, 2008, **128**, 034706.
13 L. Wang and R. T. Yang, *J. Phys. Chem. C*, 2008, **112**, 12486–12494.
14 M. Yamauchi, H. Kobayashi and H. Kitagawa, *ChemPhysChem*, 2009, **10**, 2566–76.
15 S. L. Bernasek, W. J. Siekhaus and G. A. Somorjai, *Phys. Rev. Lett.*, 1973, **30**, 1202–1204.
16 S. L. Bernasek and G. A. Somorjai, *J. Chem. Phys.*, 1975, **62**, 3149.
17 M. Salmeron, R. J. Gale and G. A. Somorjai, *J. Chem. Phys.*, 1977, **67**, 5324.
18 P. N. Ross and P. Stonehart, *J. Res. Inst. Catal. Hokkaido Univ.*, 1974, **22**, 22–41.
19 C. P. O'Brien, J. B. Miller, B. D. Morreale and A. J. Gellman, *J. Phys. Chem. C*, 2011, 24221–24230.
20 L. Xu, Y. Ma, Y. Zhang, B. Teng, Z. Jiang and W. Huang, *Sci. China Chem.*, 2011, **54**, 745–755.
21 E. Fiordaliso, S. Murphy, R. Nielsen, S. Dahl and I. Chorkendorff, *Surf. Sci.*, 2012, **606**, 263–272.
22 M. Wallin, H. Grönbeck, A. L. Spetz, M. Eriksson and M. Skoglundh, *J. Phys. Chem. B*, 2005, **109**, 9581–9588.
23 H. Sajiki, T. Kurita, H. Esaki, F. Aoki, T. Maegawa and K. Hirota, *Org. Lett.*, 2004, **6**, 3521–3523.
24 M. Keppeler and E. Roduner, *Phys. Chem. Chem. Phys.*, 2014, 11–14.
25 S. B. Simonsen, I. Chorkendorff, S. Dahl, M. Skoglundh, J. Sehested and S. Helveg, *J. Am. Chem. Soc.*, 2010, **132**, 7968–

7975.
26 S. B. Simonsen, I. Chorkendorff, S. Dahl, M. Skoglundh, J. Sehested and S. Helveg, *J. Catal.*, 2011, **281**, 147–155.
27 V. P. Zhdanov, F. F. Schweinberger, U. Heiz and C. Langhammer, *Chem. Phys. Lett.*, 2015, **631-632**, 21–25.
28 Y. Fukamori, M. König, B. Yoon, B. Wang, F. Esch, U. Heiz and U. Landman, *ChemCatChem*, 2013, **5**, 3330–3341.
29 K. Wettergren, F. F. Schweinberger, D. Deiana, C. J. Ridge, A. S. Crampton, M. D. Rötzer, T. W. Hansen, V. P. Zhdanov, U. Heiz and C. Langhammer, *Nano Lett.*, 2014, **14**, 5803–5809.
30 T. R. Henriksen, J. L. Olsen, P. C. K. Vesborg, I. Chorkendorff and O. Hansen, *Rev. Sci. Instrum.*, 2009, **80**, 124101.
31 P. C. K. Vesborg, J. L. Olsen, T. R. Henriksen, I. Chorkendorff and O. Hansen, *Rev. Sci. Instrum.*, 2010, **81**, 016111.
32 U. Heiz, F. Vanolli, L. Trento and W.-D. Schneider, *Rev. Sci. Instrum.*, 1997, **68**, 1986.
33 S. Kunz, K. Hartl, M. Nesselberger, F. F. Schweinberger, G. Kwon, M. Hanzlik, K. J. J. Mayrhofer, U. Heiz and M. Arenz, *Phys. Chem. Chem. Phys.*, 2010, **12**, 10288–91.
34 F. F. Schweinberger, *Dissertation*, Technische Universität München, 2013.
35 H.-P. Cheng and U. Landman, *J. Phys. Chem.*, 1994, **98**, 3527–3537.
36 K. Bromann, H. Brune, C. Félix, W. Harbich, R. Monot, J. Buttet and K. Kern, *Surf. Sci.*, 1997, **377**, 1051–1055.
37 U. J. Quaade, S. Jensen and O. Hansen, *J. Appl. Phys.*, 2005, **97**, 1–5.
38 P. Hohenberg and W. Kohn, *Phys. Rev.*, 1964, **136**, B864–B871.
39 W. Kohn and L. Sham, *Phys. Rev.*, 1965, **140**, 1133–1138.
40 Q. Fu and T. Wagner, *Surf. Sci. Rep.*, 2007, **62**, 431–498.
41 J. J. Mortensen, L. Hansen and K. W. Jacobsen, *Phys. Rev. B*, 2005, **71**, 035109.
42 S. Bahn and K. W. Jacobsen, *Comput. Sci. Eng.*, 2002, 56–66.
43 J. Wellendorff, K. Lundgaard, A. Møgelhøj, V. Petzold, D. Landis, J. K. Nørskov, T. Bligaard and K. W. Jacobsen, *Phys. Rev. B*, 2012, **85**, 235149.
44 F. Behafarid, L. K. Ono, S. Mostafa, J. R. Croy, G. Shafai, S. Hong, T. S. Rahman, S. R. Bare and B. Roldan Cuenya, *Phys. Chem. Chem. Phys.*, 2012, **14**, 11766.
45 B. Wang, B. Yoon, M. König, Y. Fukamori, F. Esch, U. Heiz and U. Landman, *Nano Lett.*, 2012, **12**, 5907–5912.
46 H. Monkhorst and J. Pack, *Phys. Rev. B*, 1976, **13**, 5188–5192.
47 N. Fukui and H. Yasumatsu, *Eur. Phys. J. D*, 2013, **67**, 81.
48 G. H. Vurens, D. R. Strongin, M. Salmeron and G. A. Somorjai, *Surf. Sci.*, 1988, **199**, L387–L393.
49 G. C. van Leerdam, H. Brongersma, I. I. M. Tijburg and J. W. Geus, *Appl. Surf. Sci.*, 1992, **55**, 11–18.
50 H. H. Brongersma, P. Groenen and J.-P. Jacobs, *Mater. Sci. Monogr.*, 1995, **81**, 113–182.
51 C. S. Ewing, M. J. Hartmann, K. R. Martin, A. M. Musto, S. J. Padinjarekutt, E. M. Weiss, G. Veser, J. J. McCarthy, J. K. Johnson and D. S. Lambrecht, *J. Phys. Chem. C*, 2015, **119**, 2503–2512.
52 S. Yook, H. Shin, H. Kim and M. Choi, *ChemCatChem*, 2014, **6**, 2836–2842.
53 E. Bus and J. A. van Bokhoven, *Phys. Chem. Chem. Phys.*, 2007, **9**, 2894–2902.
54 R. A. Olsen, G. J. Kroes and E. J. Baerends, *J. Chem. Phys.*, 1999, **111**, 11155.
55 E. Skúlason, A. A. Faraj, L. Kristinsdóttir, J. Hussain, A. L. Garden and H. Jónsson, *Top. Catal.*, 2013, **57**, 273–281.
56 A. Pasteur, S. Dixon-Warren, Q. Ge and D. King, *J. Chem. Phys.*, 1997, **106**, 8896.
57 T. Gomez, E. Florez, J. A. Rodriguez and F. Illas, *J. Phys. Chem. C*, 2011, **115**, 11666–11672.
58 C. Zhou, J. Wu, A. Nie, R. C. Forrey, A. Tachibana and H. Cheng, *J. Phys. Chem. C*, 2007, **111**, 12773–12778.
59 I. Chorkendorff and J. W. Niemantsverdriet, *Concepts of Modern Catalysis and Kinetics*, Wiley-VCH Verlag GmbH, 2nd edn, 2007.
60 W. Tang, E. Sanville and G. Henkelman, *J. Phys. Condens. Matter*, 2009, **21**, 084204.

Methanation on size-selected $Ni_{75}Fe_{25}$ nano-particles

Jakob Nordheim Riedel, Béla Sebök, Elisabetta Maria Fiordaliso, Alexander Krabbe, Anders Bodin, Thomas Pedersen, Christian Danvad Damsgaard, Jakob Birkedal Wagner, Peter Christian Kjærgaard Vesborg, Ole Hansen, and Ib Chorkendorff

Catalytic methanation reaction from CO and H_2 was studied on mass selected $Ni_{75}Fe_{25}$ nano-particles with sizes 3.5 nm, 5 nm, 7 nm and 9 nm. Results show that 7 nm particles are consistently more active than the other sizes. Characterization before and after chemical activity measurements using ISS, XPS, and SEM demonstrates a highly stable catalyst up to 225 °C.

In preparation